SPATIAL DISTRIBUTION OF ACTIVE SITES AND BUBBLE FLUX DENSITY

SPATIAL DISTRIBUTION OF ACTIVE SITES
AND BUBBLE FLUX DENSITY

by

MOHAMED A. E. SULTAN, B.Sc. (Eng.)

A Thesis

Submitted to the School of Graduate Studies
in Partial Fulfilment of the Requirements
for the Degree
Master of Engineering

McMaster University

April 1977

TO BOSHRA

MASTER OF ENGINEERING
(Mechanical Engineering)

McMaster University
Hamilton, Ontario

TITLE: Spatial Distribution of Active Sites and Bubble Flux Density

AUTHOR: MOHAMED ABD EL-MOHTY SULTAN,
B.Sc. (Mech. Eng.),
(Alexandria University, Alexandria, Egypt)

SUPERVISOR: Dr. Ross L. Judd

NUMBER OF PAGES: xii, 131

ABSTRACT

An experimental investigation is presented for boiling of water at atmospheric pressure on a single copper surface. The distribution of active sites was investigated at different levels of heat flux and subcooling. The results obtained indicated that the active sites were distributed randomly on the heating surface, since the distribution of active sites followed the Poisson distribution.

Changes in heat flux and subcooling did not affect the distribution of active sites, although additional active sites formed among the sites which had been already activated when heat flux was increased.

The frequency of vapour bubble emission and the bubble flux density have been studied as well. The results obtained showed that the surface superheat had a great effect on the vapour bubble emission frequency, although the influence of subcooling was of lesser significance. The bubble flux density showed a marked tendency to cluster and was not uniformly distributed over the heating surface.

ACKNOWLEDGEMENTS

It is my pleasure to express my sincere gratitude to Dr. Ross L. Judd for his guidance, valuable advice and continuous encouragement throughout the duration of the present investigation.

I would like to express my thanks to Professor J. N. Siddall and Professor C. W. Dunnett for their helpful comments.

The author also expresses his appreciation to Ms. Lorraine A. Oneschuk for typing the manuscript.

The financial support provided by the National Research Council through grant A 4362 is also acknowledged.

TABLE OF CONTENTS

LIST OF FIGURES

LIST OF TABLES

CHAPTER I

INTRODUCTION

In the last few years, a sudden interest in boiling heat transfer was initiated to provide empirical information and to clarify the mechanism of boiling heat transfer to meet the development of devices such as nuclear power plant reactors.

Boiling heat transfer is defined as the mode of heat transfer that occurs with change of phase from liquid to vapour. Pool boiling is the type of boiling which occurs on a heating surface submerged in pool of quiescent liquid. When the surface temperature exceeds the saturation temperature of the liquid sufficiently, vapour bubbles form at specific locations on the heating surface such as pits, scratches, and grooves which have an ability for trapping vapour. These locations of bubble origin are called active sites. The heating surface contains many potentially active sites which have trapped small amounts of vapour or gas but are not necessarily active sites. According to the amount of heat flux applied, some of the potentially active sites become active and the number of active sites increases as the heat flux increases until the entire surface becomes "vapour blanketed" at high rates of heat flux. Figure (1) shows the different boiling regimes. The present investigation is concerned with the "bubble" regimes and involves the study of the distribution of active sites on the heating surface with different levels of heat flux and subcooling. In addition, the vapour bubble emission frequency and the distribution of bubble flux density on the heating area, have been studied as well.

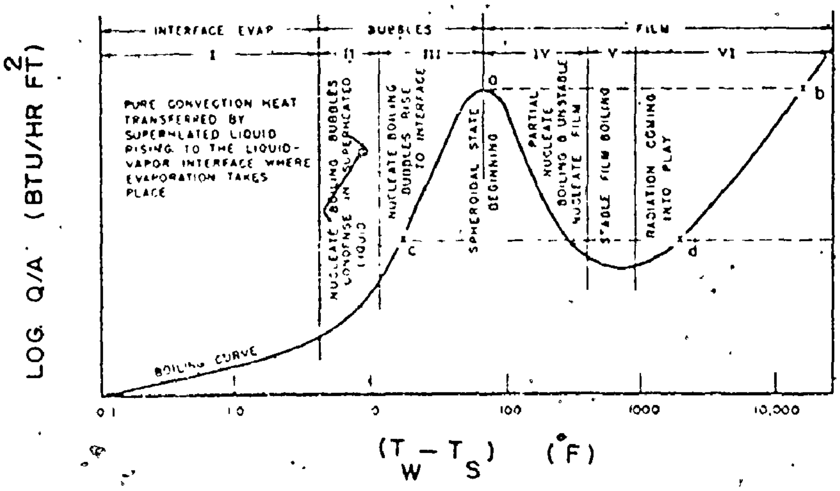

Figure (1) Representative Characteristic Boiling Curve

CHAPTER 2

LITERATURE SURVEY

2.1 Effect of Surface Condition on Nucleate Boiling

Jakob [1] demonstrated that the rate of heat transfer increased as macroscopic roughness increased and shifted the boiling curve markedly as shown in Figure (2). Corty and Foust [2] used a profilometer, which measured the surface roughness by interpretting the motion of a 0.001 inch diameter diamond tip as it travelled over the surface. The results obtained showed that both the slopes and position of the boiling curve changed with the change in surface roughness. Corty and Foust plotted the superheat as a function of roughness for constant heat transfer coefficient as shown in Figure (3). Hsu and Schmidt [3] also showed that heat transfer increased with increasing surface roughness for a polished 304 stainless steel surface. In a subsequent investigation, Kurihara and Myers [4] studied boiling with different surface finishes (emery paper 410, 310, 210, 0, 1, 2 and also on a surface roughened by polishing with 140 mesh carborandum) and found that the number of active boiling centers increased with increased surface roughness. Berenson [5] investigated the effect of two surface roughnesses using different surface materials prepared by lapping and by emery paper. The results indicated that heat transfer was greater in case of the lapped surface than in the case of the emery paper finished surface. Thus, heat transfer decreased with an apparent

Curve No.	State of Heating Surface
1	Recently roughened by a sand blast
2	Same, oxidized by longer use
3	Same, roughened once more by sand blast
4	Same, after long use
5	Recently fitted with a roughness screen and cleaned
6	Same, after 4 hours of boiling, followed by 24 hours of lying in water
7	Same, after 8 more hours of boiling, followed by another 24 hours of lying in water

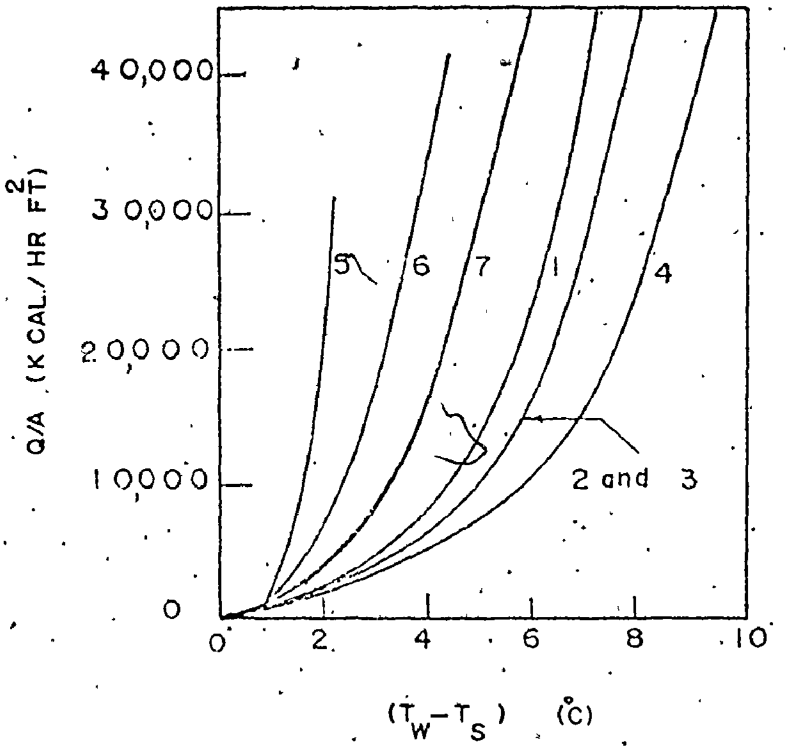

Figure (2) Effect of Surface Roughness on the Boiling of Water

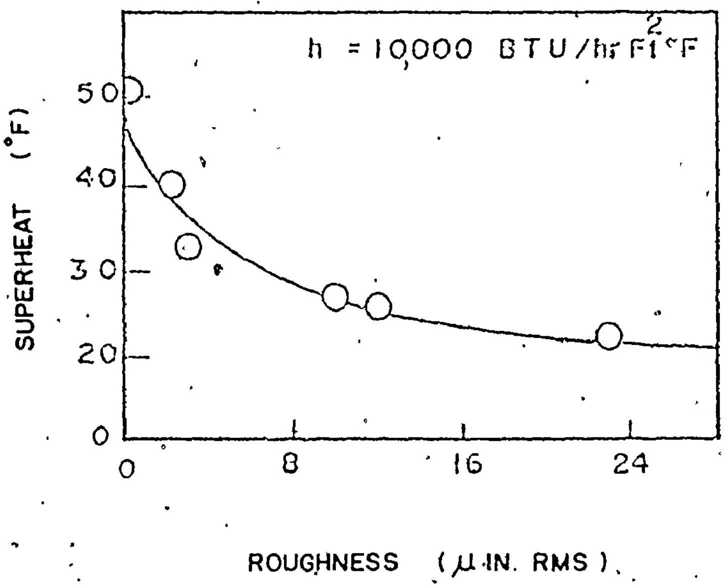

Figure (3) Surface Roughness Versus Surface Superheat at Constant Heat Transfer Coefficient increase in surface roughness, contrary to the findings of the previous investigators.

Vachon, Tanger, Davis and Nix [6] studied pool boiling on polished and chemically etched stainless steel surfaces with surface roughnesses ranging from 2 to 61 μ inches at atmospheric pressure using distilled water, and came to the same conclusion as Berenson [5], in that an increase in roughness does not necessarily mean an increase in heat transfer. Their results are shown in Figure (4). Shoukri and Judd [7], who studied pool boiling of distilled, degassed water at atmospheric pressure on a single copper surface with different surface finishes, showed that decreasing surface macroroughness shifts the boiling curve to higher superheat for the same heat flux as shown in Figure (5). Nishikawa [8] observed the formation of bubbles from a horizontal surface and observed a greater number of bubble columns on a rough surface than on a smooth one. Nishikawa found the boiling coefficients to be higher on the rough surface.

The material of the boiling surface appears to have an effect on the boiling characteristic curve. Marto, Moulson and Maynard [9] studied two surfaces with different materials having the same surface finish (mirror finish). Figure (6) shows that the copper surface produced higher heat transfer coefficients than the nickel surface. This observation was presented as being due to the difference in thermal properties. It seems that difference may be due to the differences in the material hardness and this agrees with the findings of Berenson [5] for copper surfaces. However, Berenson explained that the differences in material hardness would tend to change the cavity size and density

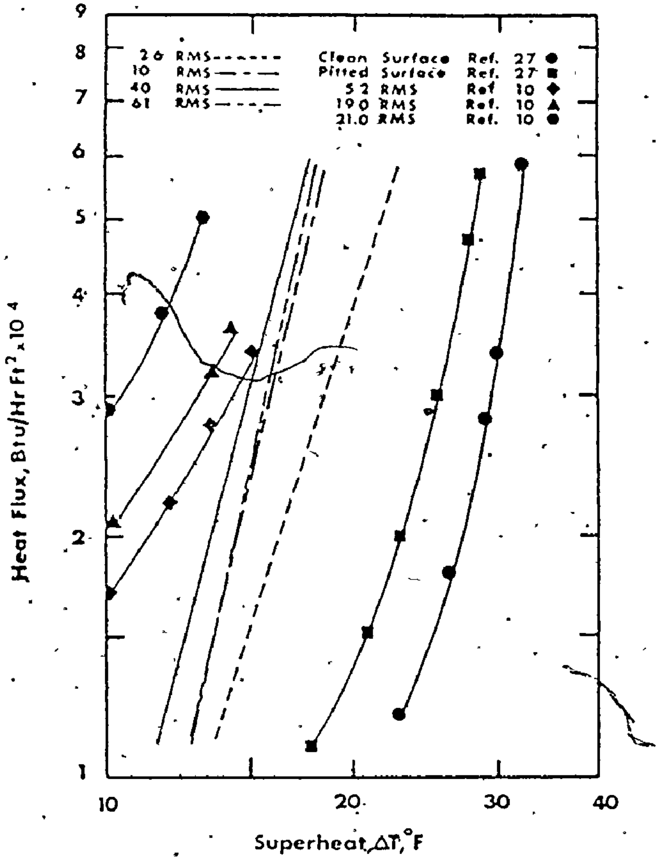

Figure (4) Heat Flux Versus Superheat

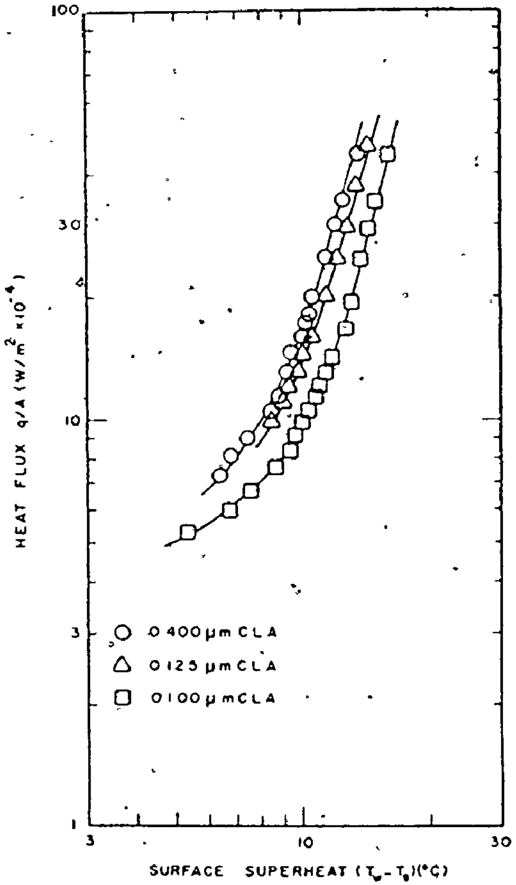

Figure (5) Boiling Characteristic Curves According to Shoukri and Judd

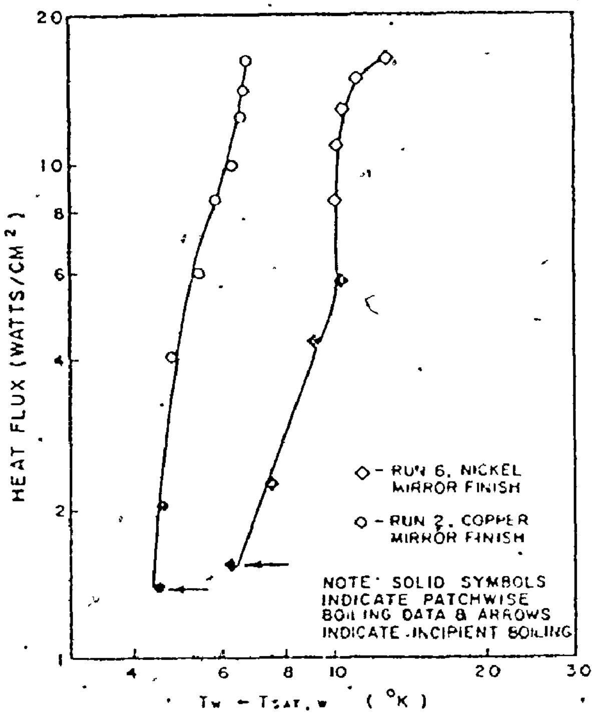

Figure (6) Effect of Material on Nucleate Boiling Curve

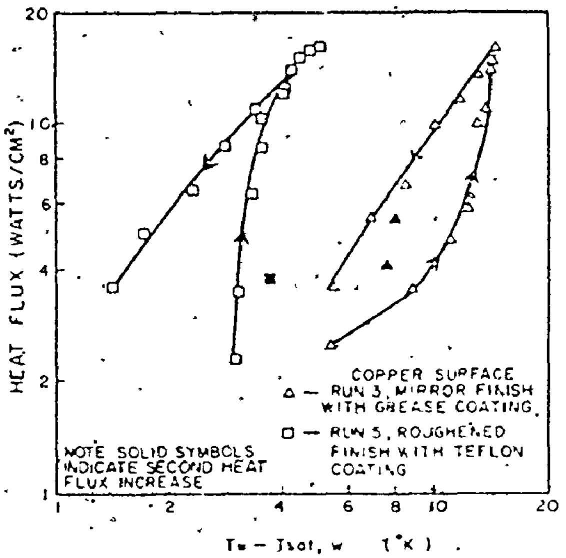

Figure (7) Effect of Coating Material on the Boiling Curve distribution on the surface. Marto, Moulson Maynard [9] also showed that the increase of surface roughness improved heat transfer coefficients and demonstrated that any coating material like grease or Teflon would shift the boiling curve. This observation implies that more superheat would be needed to get the same value of heat transfer coefficient, as shown in Figure (7).

From this survey of the effect of surface condition on nucleate boiling, it may be concluded that surface roughness cannot be used in the characterization of boiling surfaces, because surface roughness represents the macroroughness of the surface; however, surface roughness may be useful for comparison purposes when using the same technique for the preparation of boiling surfaces from the same material.

2.2 The Role of Cavities

Since it is apparent that cavities are important in determining the rate of nucleate boiling heat transfer, then it is essential to understand the role of the cavity in the process of bubble nucleation. One important aspect in nucleation theory is the action of the cavities in trapping residues of vapour or gas.

Bankoff [10] presented the conditions for entrapment of gas upon the advance of a semi-infinite liquid sheet across a groove. It can be seen in Figure (8) that if the contact angle θ is greater than wedge angle β, the advancing liquid front will strike the opposite wall of the cavity before it has completed its advance down the near wall. Consequently, a residue of gas will be trapped, which can serve as the

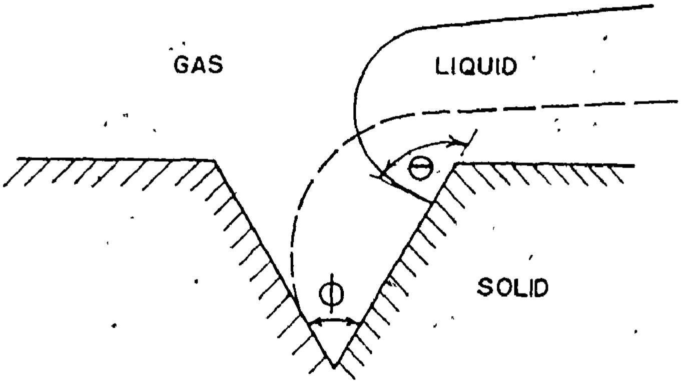

Figure (3) Conditions for the Entrapment of Gas in the Advance of a Liquid Layer Across a Groove nucleus for subsequent bubble emission. If $\theta < \phi$, the gas will be completely displaced by the liquid and the cavity will be deactivated. It can be concluded that cavities are generally more stable vapour traps than the grooves. Steep walled cavities will almost always be filled with vapour whereas, moderately sloped cavities may be filled with vapour, one instant and with liquid the next, depending on the wetting conditions.

Lorenz, Mikic and Rohsenow [11] determined that the radius of the bubble nucleus could be equal to or less than the radius of the cavity. If r is the effective radius of the nucleus and R is the cavity radius, then the ratio r/R will determine whether or not the residue of gas/vapour will fill the cavity completely. In the case of $r < R$, (e.g. organic fluids), the cavity will not be filled completely with the gas/vapour residue, whereas in the case of $r > R$ (e.g. water) the cavity will be filled completely and the bubble nucleus will stand at the mouth. For cylindrical cavities, Singh, Mikic and Rohsenow [12] determined that the volume of trapped vapour depends upon the cavity radius R, depth D and advancing contact angle θ. From the available data, values of θ in the range of 40^0 - 50^0 (copper surface) have been considered for water, and 8^0 - 15^0 for ethanol and methanol. It is apparent that due to smaller θ, organics will penetrate deeper into a cylindrical cavity and that less volume of vapour will be trapped as compared with water.

Rohsenow [13] postulated that the bubbles form at a heated surface from cavities which have already trapped some gas or vapour.

These so called active cavities grow by evaporation at the liquid-vapour interface near the heated wall as shown in Figure (9.a). When the bubble detaches, some vapour is trapped inside the cavity to form the nucleus for the next bubble as depicted in Figure (9.b). In the case of very high subcooling, two different cases must be considered for contact angle Θ giving opposite curvature of the interface. In case of $p_v > p_\ell$ as depicted in Figure (9.c), it is seen that a convex meniscus forms when the surface cools and the bubble wall temperature will never become great enough to produce equilibrium. Consequently, the nucleus collapses and the cavity completely fills with liquid and becomes inactive. In case of $p_v < p_\ell$ as depicted in Figure (9.d), it is seen that a concave meniscus forms because when the surface cools, the radius of the interface decreases, reducing p_v . Then the saturation temperature of the vapour decreases and the cavity does not collapse but becomes a potentially active nucleus for subsequent bubble formation.

2.3 Identification of Active Sites

In 1960 Gaertner and Westwater [14] investigated a method to determine the number of active sites up to 1130 sites/in^2. This method was based on the electroplating phenomena by which an impressed current at low heat flux resulted in a nickel film being plated on the surface. This technique indicated the location of the active sites, since during the electroplating, vapour bubbles originating at the active sites, would push the plating solution away from the surface so that very little metal could be plated at the location. High contrast photographs

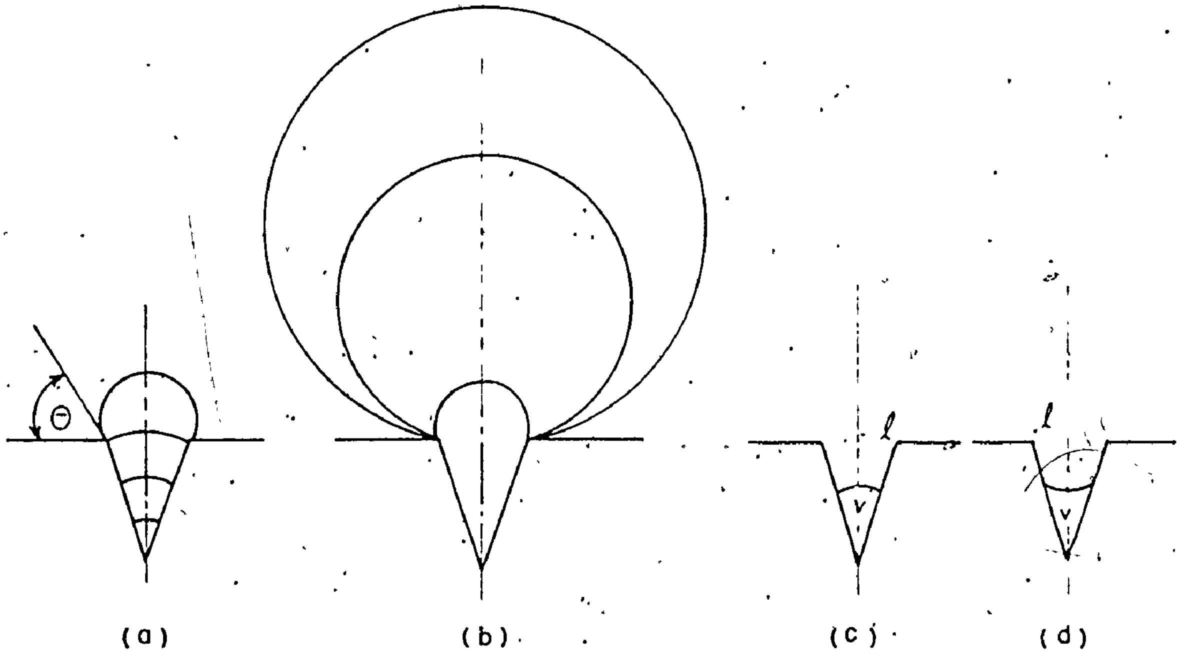

Figure (9) The Formation of Vapour Bubbles Over Cavities in a Heated Surface were taken of the plated surface to permit counting of the pinholes representing the active sites. However, this technique is restricted to electroplating solutions only.

In 1967, Heled and Orell [15] proposed another technique which greatly facilitates the identification and location of active sites. Their technique was based on the observation of thin scale deposits (5 to 30 μin.) which formed on highly polished surface (first polished to a high degree and then electroplated with either chrome or nickel). The tap water or distilled water which was boiled contained soluable salts which formed ring shaped deposits during nucleate boiling. At first, Orell tried this technique using an artificial cylindrical pit. The results indicated that the size of pits range from 590 to 2000 μin. at a temperature difference of 18^{o}F in the presence of a thermal boundary layer of 3000 μin. thickness which are in good agreement with the theoretical size range predicted by Hsu. With this technique, active site density could be obtained up to 15,700 sites/ft^{2}. Furthermore, this technique can be used for different fluids in the presence of a highly polished surface so long as sufficient salts can be dissolved.

In 1974 Nail, Vachon and Morehouse [16] studied pool boiling over a cold rolled, 304 stainless steel test specimens. A-C power was controlled so that the first twelve to twenty bubbles formed on the surface remained on the surface sufficiently long to allow the bubble locator to be positioned over the center of selected bubbles. The positions of all the centers were recorded and the surface was removed for study in the scanning electron microscope. This method is restricted for low heat flux only.

These are the only different site identifying techniques which are known at the present time.

2.4 Effect of Active Site Distributions on the Rate of Heat Transfer

Jakob and Fritz [17] advanced the theory that each active site contributes a quantized amount to the overall rate of heat transfer. If the number of active sites were doubled, the rate of heat transfer would increase proportionately. References [4] and [14] have indicated that the average rate of heat transfer attributed to an individual active site is not a fixed value but depends on the active site density. Zuber [18] found the relationship

$$\left(\frac{Q/A}{\bar{N}/A}\right) \alpha \left(\frac{\Delta T_{sup}}{(\bar{N}/A)^{0.5}}\right)^{3/2} \qquad ----1$$

Combining this equation with Gaertner's [19] equation

$$\bar{S} = \frac{1}{2}\,\frac{\bar{N}}{A}^{-\frac{1}{2}} \qquad ----2$$

gives the relationship

$$\frac{Q/A}{\bar{N}/A} \alpha (\bar{S}\,\Delta T_{sup})^{3/2} \qquad ----3$$

It is seen that at constant ΔT_{sup}, the average rate of heat transfer associated with one active site decrease as the active site density becomes larger or as the mean nearest-neighbor distance between sites decreases. Zuber [18], concluded that the heat transfer characteristics of nucleate boiling are determined by hydrodynamic processes. As the distance between the sites changes the hydrodynamic processes change. Zuber divided nucleate boiling into two regions. The first region (active site isolation) is the region where the distance between the bubbles is relatively large. The predominant mechanism of heat transfer is natural convection and the turbulence and microconvection caused by the growth of the bubbles affect heat transfer only slightly. The second region (active site congestion) is the region where the temperature at the surface has increased such that the smaller nuclei on the surface have started becoming activated and more active sites have been created. As the active sites come closer together, they start competing for a supply of liquid from the superheated boundary layer and hydrodynamic instabilities begin to take place. In reference [14], Westwater and Gaertner studied the effect of heat flux on the average diameter of the vapour aureole, the circular area of bubble contact on the surface before departure. From Figure (10), at low rates of heat transfer the aureole diameters are seen to be independent of heat flux. However, at high rates of heat transfer the diameters of the aureole decrease with an increase of heat flux or active site density. Zuber [18] interpreted the knee in the curve in Figure (10) as a transition from the active site isolation region to active site congestion region which occurs when the average distance between active sites is approximately twice the average diameter of the aureole.

Gaertner [19] investigated the distribution of active sites on a heating surface with three levels of heat flux and showed a good

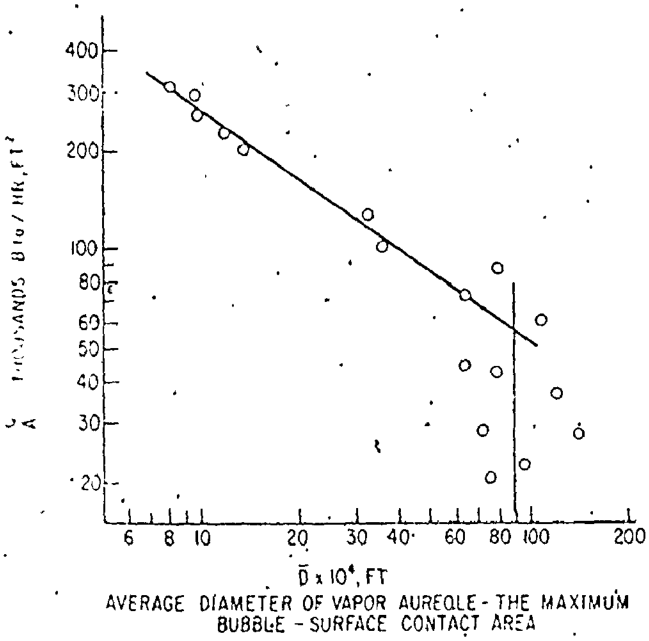

Figure (10) Average Diameter of Vapour Aureole the Maximum Bubble Surface Contact Area agreement with results predicted by the Poisson distribution as shown in Figure (11). The Poisson equation:

$$P_{\overline{Na}}(Na) = \frac{e^{-\overline{Na}}(\overline{Na})^{Na}}{Na!} \qquad \text{----4}$$

where $P_{\overline{Na}}(Na)$ is the probability that event Na will occur when the mean or expected value of Na is $\overline{Na}$. Therefore, $P_{\overline{Na}}(Na) = \frac{a}{A} Z_{Na}$ ----5

Gaertner [19] postulated that as the surface temperature rose the active site density would increase according to $\frac{Q}{A} = C\left(\frac{N}{A}\right)^m$ ----6 and obtained values of m and C. The value of m was equal to 0.66. Shoukri and Judd [7] obtained a value of m equal to 0.5, Gaertner and Westwater [14] obtained a value of m equal to 0.49 and Staniszewski [20] found m = 1, decreasing to m = 0.5 as Q/A increased. It is clear that the value of m lies in the range from 0.5 to 1. Gaertner [19] also proposed a site activation theory in which the active site density was related to the fluid properties, system pressure and surface temperature by the relationship

$$\frac{N}{A} = N_0 \exp\left\{-\left[\frac{16\pi\sigma^3 M^2 N^*}{3\rho_\ell^2 \bar{R}^3 \left[\ln\left(\frac{P_\infty}{P_v}\right)\right]^2}\right] \Phi \left(\frac{1}{T_w}\right)^3\right\} \qquad \text{----7}$$

in which N_0 and Φ are two arbitrary constants which will vary with each fluid/surface combination. The exponential term describes the fraction of the potentially active sites activated by a particular combination of system pressure, fluid characteristics and surface temperature, whereas the coefficient represents the number of potentially active sites per unit area. Figure (12) shows that the straight lines

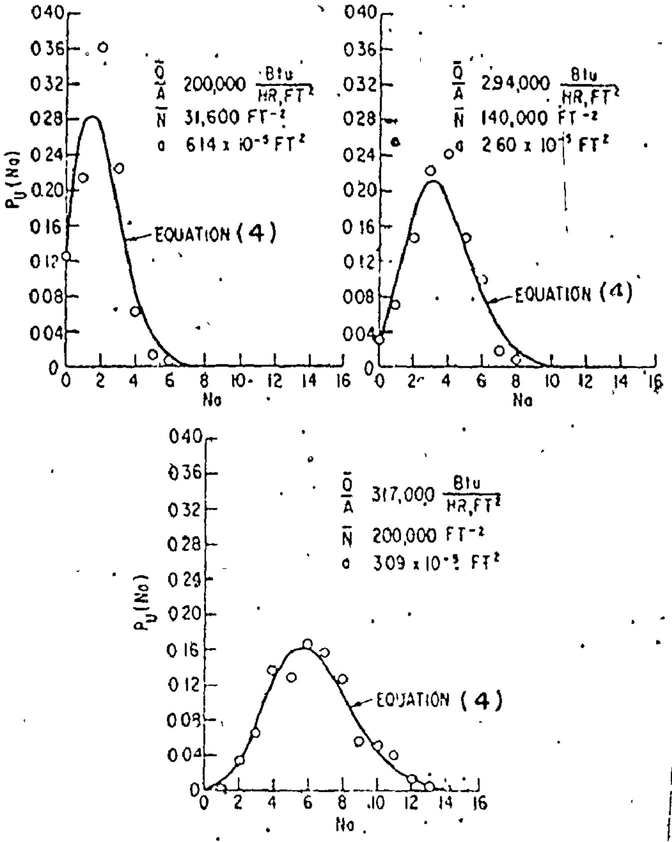

Figure (11) Distribution of the Local Active Site Populations

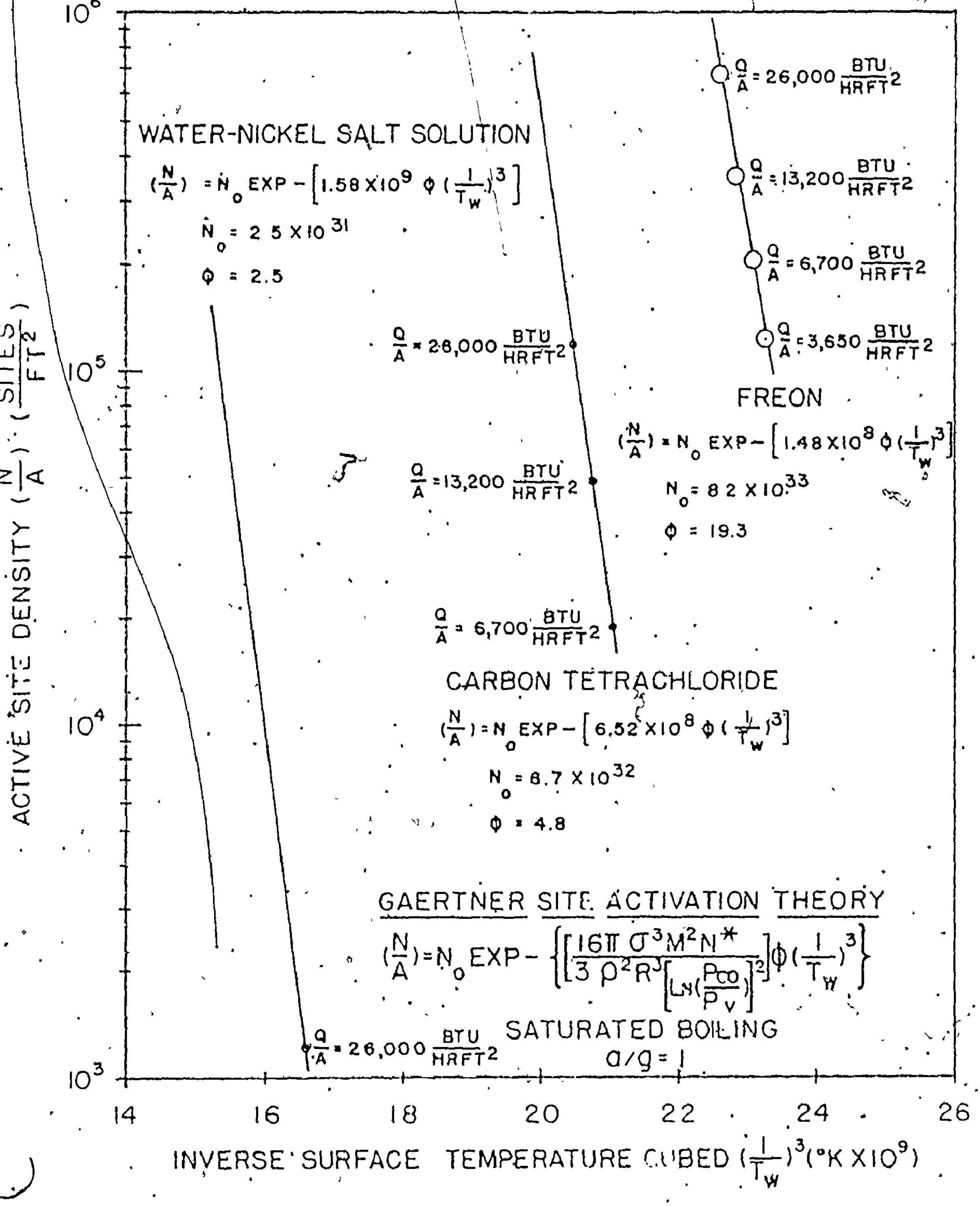

Figure (12) Active Site Density Versus Inverse Surface Temperature Cubed correlating active site density with inverse surface temperature cubed for different authors, are observed to be nearly parallel and that therefore, the value of $\left\{\dfrac{16\pi\sigma^{3}M^{2}N^{*}}{3\rho_{\ell}^{2}\bar{R}^{3}\left[\ln\left(\dfrac{P_{\infty}}{P_{v}}\right)\right]^{2}}\right\}\phi$ is almost invariant for different fluids.

Brown [21] suggested that the site density (N/A) of nucleation cavities of radius greater than or equal to R could be correlated according to $(N/A) \alpha (1/R)^{m}$ which will yield the total active site density (N/A) when the minimum cavity radius R_{min} is substituted. Shoukri and Judd [7] found that the relationship advanced by Brown correlated their active site density data with cavity radius, and recommended the parameter group $2\sigma T_{s}/\rho_{v}h_{fg}(T_{w} - T_{s})$ to predict the minimum nucleation cavity radius. Therefore, the usage of this parameter group with Brown's correlation is recommended as a sufficient method describing the boiling nucleation characteristics.

2.5 Distribution of Nearest-Neighbor Distance Between Active Sites

The distribution of nearest-neighbor distances between points in a randomly scattered spatial array is of great interest in many areas of the biological and physical sciences. Gaertner [19] applied the analysis of Clark and Evans and considered a random array of sites as shown in Figure (13a). If an arbitrarily selected active site A_1 is chosen as the center of a circle having a radius s which is the approximate distance to its nearest-neighbor A_2, the probability of finding N active sites in area πs^2 where the active site

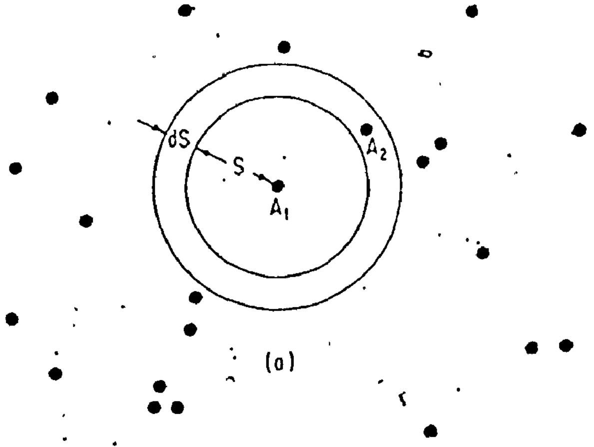

Figure (13) Random Array of Active Sites Model of Nearest-Neighbor Distance Between Sites density over the heating surface is $\frac{\bar{N}}{A}$ is given by

$$P(N) = \frac{e^{-\frac{\bar{N}}{A}\pi s^2}\left(\frac{\bar{N}}{A}\pi s^2\right)^N}{(N)!} \qquad ----8$$

Therefore the probability that no active site (N = 0) will be found in the area πs^2 other than A_1 which is specified to be in the center (probability equals one) is given by a Poisson equation

$$P(o) = e^{-\frac{\bar{N}}{A}\pi s^2} \qquad ----9$$

where the active sites are assumed to be uniformly distributed over the surface. Similarly, the probability of finding N active sites in an area $2\pi sds$ surrounding the area πs^2 is given by

$$P(N) = \frac{e^{-\frac{\bar{N}}{A}2\pi sds}\left(\frac{\bar{N}}{A}2\pi sds\right)^N}{(N)!} \qquad ----10$$

Consequently, the probability that one active site (N = 1) will be found in a shell of area $2\pi sds$ is

$$P(1) = \frac{\bar{N}}{A}2\pi sds \qquad ----11$$

because $e^{-\frac{\bar{N}}{A}2\pi sds}$ approaches unity.

The probability that A_2 is the nearest-neighbor of A_1 where the distance between them lies between s and s + ds is given by the product of equations (9) and (11)

$$P(s<s<s+ds) = 2\pi s\frac{\bar{N}}{A}e^{-\frac{\bar{N}}{A}\pi s^2}.ds \qquad ----12$$

Gaertner [19] then differentiated the probability density function as presented in equation (12) and set the result equal zero to obtain the most probable nearest-neighbor distance

$$2\pi\frac{\bar{N}}{A}e^{-\frac{\bar{N}}{A}\pi s^2} + 2\pi s\frac{\bar{N}}{A}\left(-2\pi s\frac{\bar{N}}{A}\right)e^{-\frac{\bar{N}}{A}\pi s^2} = 0 \qquad ----13$$

Therefore the expression obtained for the most probable nearest-neighbor distance is given by:

$$S_{mp} = \frac{1}{\sqrt{2\pi}} \left(\frac{\overline{N}}{A}\right)^{-\frac{1}{2}} \qquad \text{----14}$$

The mean and root mean square nearest-neighbor distances were obtained by an averaging technique

$$\overline{S} = \frac{1}{2} \left(\frac{\overline{N}}{A}\right)^{-\frac{1}{2}} \qquad \text{----15}$$

$$\sqrt{\overline{S}^2} = \frac{1}{\sqrt{\pi}} \left(\frac{\overline{N}}{A}\right)^{-\frac{1}{2}} \qquad \text{----16}$$

Figure (14) shows the plot of equations (14), (15) and (16). None of the nearest-neighbor distances defined by these equations agree with the data of Gaertner and Westwater [14] presumably because the data represented is not the average nearest-neighbor distance as will be discussed later.

2.6 Distribution of Bubble Emission Frequency

The prediction of bubble frequency for bubbles growing on a heating surface is not well established, although work still continues in this direction. The information which is available has been primarily generated at McMaster University. An understanding of bubble emission frequency is essential in the development of nucleate boiling models.

Although heat flux may be considered to be uniformly distributed over the heating surface, the distribution of active sites is not necessarily uniform. Consequently, the bubble emission fre-

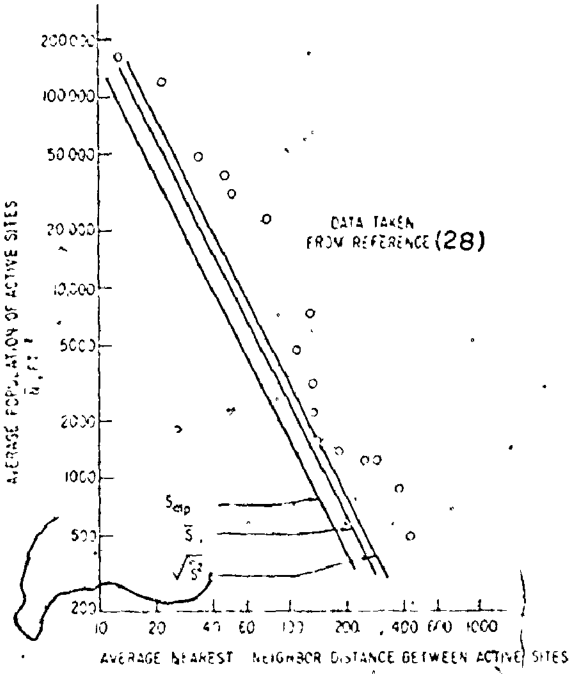

Figure (14) Average Population of Active Site Versus Average Nearest-Neighbor Distance quency may not be the same for all of the active sites and accordingly the frequency may vary from one site to another over the heating surface. The distribution of bubble emission frequency is one aspect of nucleate boiling which has received little attention.

Judd [22] studied pool boiling of Freon 113 on a glass plate coated with an electrically conducting oxide film by using results obtained from two high speed motion picture film strips. The first film strip was exposed at 2,000 frames/second and the second film strip was exposed at 1,000 frames/second. The framing rates chosen enabled a complete cycle of vapour bubble emission including active and inactive periods to be photographed on one or both of the film strips for bubbles forming at a number of active nucleation sites. Each of the film strips obtained was analysed to determine the frequency of vapour bubble emission for a particular combination of heat flux and subcooling. The average frequency of vapour bubble emission was determined at ten different nucleation sites chosen at random on the heating surface, by taking the average value of frequency of vapour bubble emission for each active site and then summing up these averages and dividing by the number of active sites. Judd showed that the value of the average frequency of vapour bubble emission varied directly with heat flux and indirectly with subcooling. These results may be a good representation provided that the sites chosen to compute the frequency are representative and a large number of active sites are examined.

Voutsinos [23] studied the influence of heat flux and subcooling upon the frequency of vapour bubble emission for dichloromethane boiled on a glass surface coated with an electrically conducting oxide film. Using the results obtained from high speed motion picture film strips, Voutsinos obtained a "time interval" average frequency of vapour bubble emission by counting the total number of bubbles observed during the length of motion picture film and dividing by the film duration. Voutsinos showed that the average frequency of vapour bubble emission decreases slightly with increasing subcooling. This phenomena was explained by arguing that a bubble takes longer periods of time to reach departure size. This explanation is not quite adequate because it is contrary to the results obtained on a similar surface with the same fluid by Judd and Hwang [24] who showed that at the same heat flux, the bubble departure size decreases with increasing subcooling.

In 1976, Judd and Hwang [24] studied pool boiling of dichloromethane on a glass plate coated with electrically conducting oxide film by means of high speed motion pictures. The average frequency was computed at each site which emitted two or more bubbles. A "surface weighted" average frequency was obtained by summing up the average frequency for all of the active sites selected and then dividing by the number of active sites to obtain the average frequency per site. This result was multiplied by the average activity ratio for the various sites on the heating surface. The average activity ratio is defined as the average ratio of the times for which each site is active divided by the total duration time. Judd and Hwang showed that within the small range of subcooling which was investigated, the frequency of vapour bubble emission increased by up to 233% when heat flux increased by 120% and also showed that for constant heat flux, the average frequency of bubble emission increased by 120% when subcooling increased by 11.3°C from the saturation condition. However, these authors argued that the frequency of vapour bubble emission must decrease as subcooling increases further since cessation of bubble formation is expected under high levels of subcooling. These results are contrary to the results obtained by Judd [22] and Voutsinos [23]. Judd [22] studied the average frequency for only a small number of active sites and with a wide range of subcooling and these effects at the lower subcooling may have been missed. The film duration in Voutsinos study was quite short, so that the results may not be representative.

From this survey of the frequency of vapour bubble emission, it may be seen that as heat flux is increased, the frequency of vapour bubble emission increases and that with increasing subcooling, the frequency of bubble emission first increases to a certain value and then decreases again. These findings are however, extremely tenuous at the present time.

A private communication with Dr. Judd concerning some unpublished experimental results obtained on June 29, 1976 for dichloromethane boiling on an oxide coated glass surface by using high speed pictures is discussed below. The pictures obtained were examined by using a projector, not only to determine the locations of active sites over the heating surface but also the number of the frame at which each bubble started to grow.

The average frequency of vapour bubble emission for each active site in bubbles/1000 frames was computed by summing up the inverse of differences in frame numbers for each cycle during 1000 frames and then dividing by the number of bubbles observed at the particular active site. Figure (15) shows in qualitative sense that bubble emission frequency is not distributed uniformly over the heating surface.

2.7 Distribution of Bubble Flux Density

It is important to know how the bubble flux density varies over a heating surface in order to understand the mechanism of nucleate boiling heat transfer. The fact that very little bubble flux density data exists may be due to the fact that frequency of vapour bubble emission is not well established. Voutsinos [15] studied the influence of heat flux and subcooling upon the bubble flux density. For dichloromethane boiling on a glass surface the bubble flux density was determined as the product of the "time interval" average bubble frequency multiplied by the active site density. Voutsinos showed that the bubble flux density increases with increasing heat flux and decreases with increasing subcooling.

More recently, Judd and Hwang [24] studied the influence of heat flux and subcooling upon the bubble flux density as well. For dichloromethane boiling on a glass surface the bubble flux density was determined as the product of the "surface weighted" average bubble

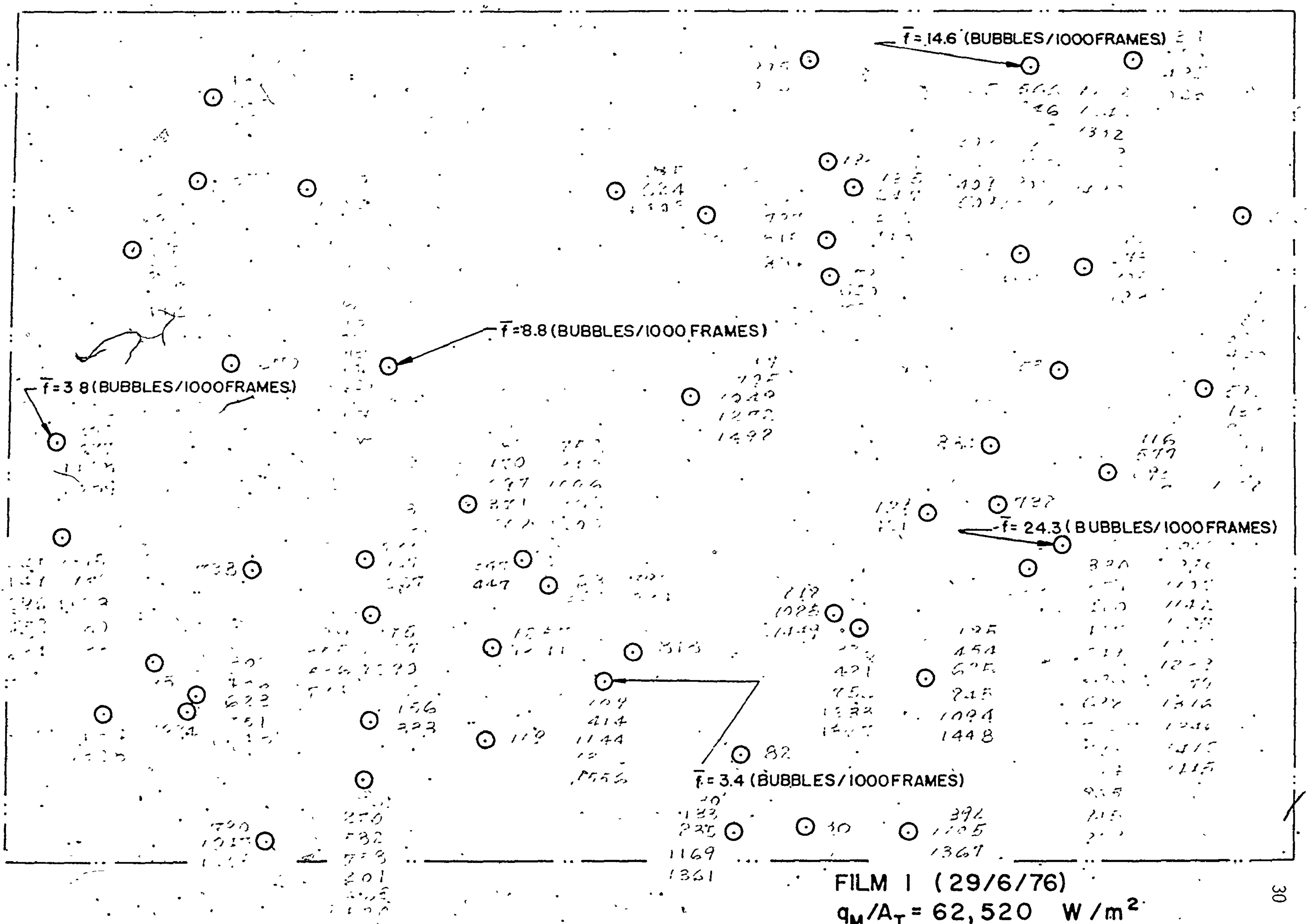

Figure (15) Bubble Frequency at Different Active Sites According to Judd

FILM I (29/6/76)
q_M/A_T = 62,520 W/m^2
P_S = 29.52 INCHES Hg.
T_S = 105°F (40.6°C)

frequency by the active site density. The results obtained are in good agreement with the effect of heat flux but contrary to the effect of subcooling when compared with the results obtained by Voutsinos [23]. The different subcooling effects may be due to the different methods of obtaining the average frequency of vapour bubble emission as discussed in the previous section.

CHAPTER 3

EXPERIMENTAL APPARATUS

At the commencement of the research, an experimental apparatus constructed by Wiebe [25] in 1970 to measure temperature profiles near to the heating surface already existed. However, the operating criteria for the present investigation were considerably changed from the previous requirements and consequently, the apparatus described below is essentially a modified design.

3.1 Design Criteria

The apparatus was modified to be capable of:

1. Boiling water up to a maximum heat flux of 150,000 BTU/hr. ft.^{2}
2. Subcooling the bulk liquid by at least 70^0 F at the maximum heat flux condition.
3. Determining the different locations of the active nucleation sites on the heating surface.

3.2 Boiler Assembly

A sectional view of the complete boiler assembly is presented in Figure (16). The vessel was made from schedule 40 stainless steel pipe, 18 inches in length by 8 inches inside diameter. Two stainless steel flanges 3/4 inches in thickness were welded on the

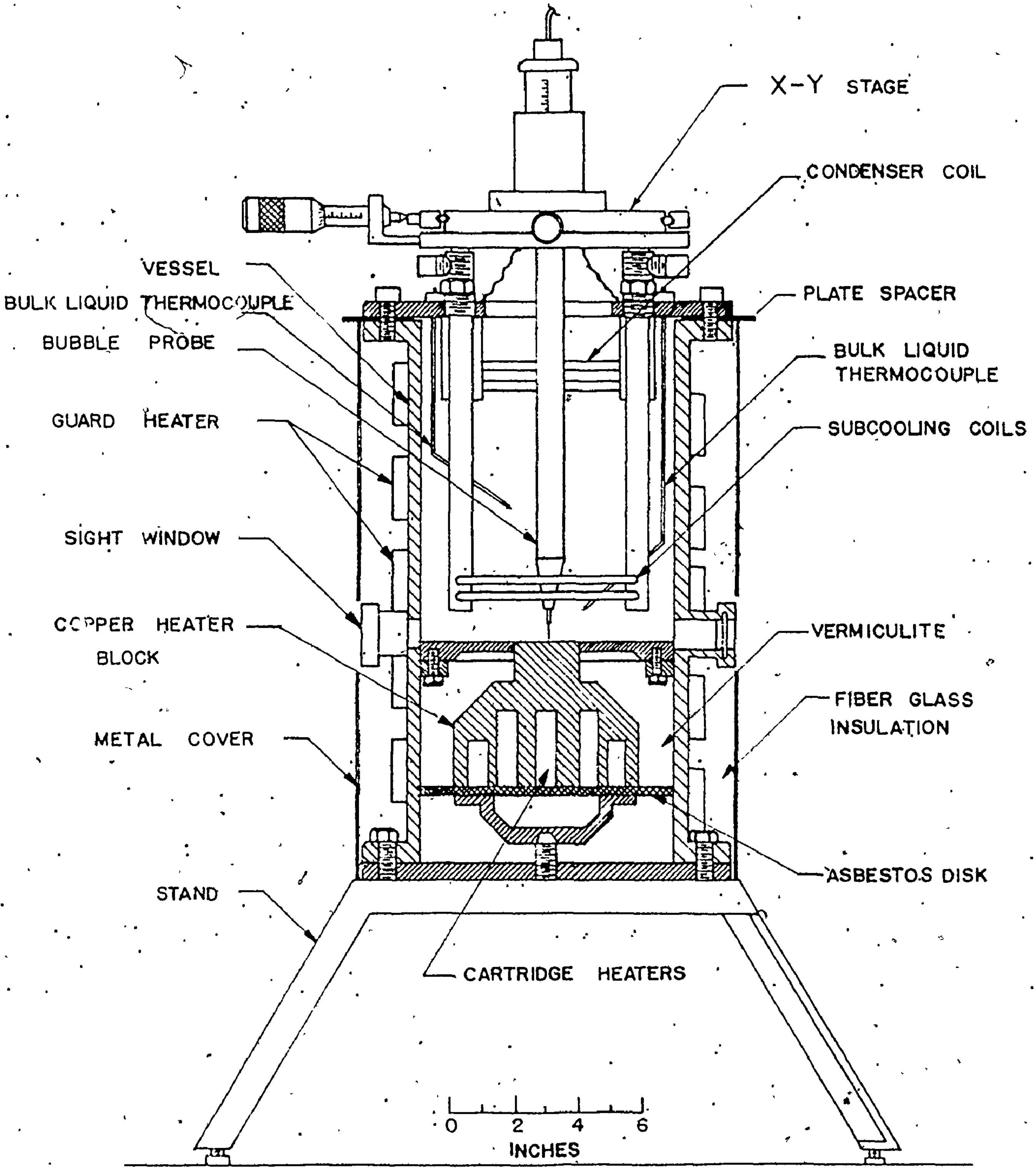

Figure (16) Section of Boiler Vessel

outside diameter at both ends of the pipe. A stainless steel cover plate 1/2 inches in thickness by 11 1/2 inches in diameter was attached to the flange at the top end of the vessel with eight 3/8 inch diameter cap screws which compressed a rubber gasket between the flange and the cover plate. Two circular sight glass windows 1 inch in diameter were located diametrically opposite at a level which permitted observation of the bubbles and the probe location over the heating surface.

The heater block was made from a copper cylinder 6 inches in diameter reduced to 2 inches at the boiling surface. Thirteen "Firerod" cartridge heaters (Watlow Electric Manufacturing Company) with a total power rating of 4000 watts were installed in symmetrically located holes in the base of the copper heater. A stainless steel skirt 1/8 inches in thickness was brazed flush with the top of the copper block to provide a continuous extension of the boiling surface. A stainless steel flange welded inside the vessel supported the skirt and positioned the heater block within the vessel. Eight cap screws served to compress an "O" ring seal which provided a water tight joint at the flange. The boiling surface was finished after the skirt was brazed before the heater block assembly was installed in the vessel.

The heating surface was initially prepared with a fine slow speed lathe cut, taken across the surface. In final finishing, the heater block assembly was rotated in a lathe chuck and the heating surface was polished using a group of "Diamond Grit" papers with numbers (200, 400 and 600) respectively. The root mean square surface roughness was measured in ten different directions by using a Talysurf profilometer. The average value of root mean square roughness for the heating surface was 10 μin.

The present investigation required that the subcooling in the bulk liquid be varied. This condition was satisfied by using a single pass heat exchanger comprised of eight 3/16 inch diameter stainless steel tubes, semi-circular in shape, brazed between two stainless steel pipes and located one inch from the skirt to provide the bulk subcooling. To condense the vapour which formed at the free surface of water, a single pass condenser comprised of two 3/16 inch diameter of stainless steel tubes arranged in a semi-circular form between two stainless steel pipes was positioned one inch below the cover plate. The cooling water flow rate through each of the coils was controlled by using needle valves.

The vessel was fitted with a vent located ~~on the cover~~ plate to allow any non-condensed vapour to escape to the atmosphere and also to keep the applied pressure at the atmospheric level.

To minimize the heat flow in the radial direction through the heater block, vermiculite was located between the heater block and the vessel. Furthermore, to minimize the heat loss from the outer wall of the vessel, twelve feet of 3 inch wide heating tape (Electrothermal Engineering Limited, Model HT 362) with the capacity of 500 watts was helically wrapped arround the vessel to serve as a guard heater. Fiberglass insulation 1 1/2 inch in thickness covered the guard heater and the vessel, which was then covered with light gauge galvanized steel sheet. An asbestos disc was attached to the bottom of the heater block to minimize the heat loss in the downward direction.

Two 36 gauge nylon insulated chromel constantan thermocouples inserted in stainless steel tubes were used to measure the bulk liquid temperature. Both thermocouples were introduced into the vessel through "Swagelok" fittings in the cover plate at 2 inch radius from the vessel centerline and were located at levels of 2 inches and 4 inches above the heating surface.

Eleven additional thermocouples were used to measure the temperature at different locations. The construction of the thermocouple assemblies is discussed in Section 3.3.

An "X - Y stage" provided with two micrometers capable of reading ± 0.0001 inch was fixed to the cover plate on four supports. The stage provided a controlled and accurate travel of the bubble probe in two normal directions.

The bubble probe described in Appendix C was mounted on a vertical travelling mechanism, to control the vertical distance between probe tip and the heating surface.

Photographs showing three different views of the test assembly and the associated equipment are presented in Figures (17), (18) and (19).

3.3 Thermocouples

Chromel constantan thermocouples were selected because the EMF characteristic for this combination of materials is approximately 36 μ Volts/ ^{0}F. To determine the axial temperature gradient in the copper block near the heating surface, three thermocouples A, B and C

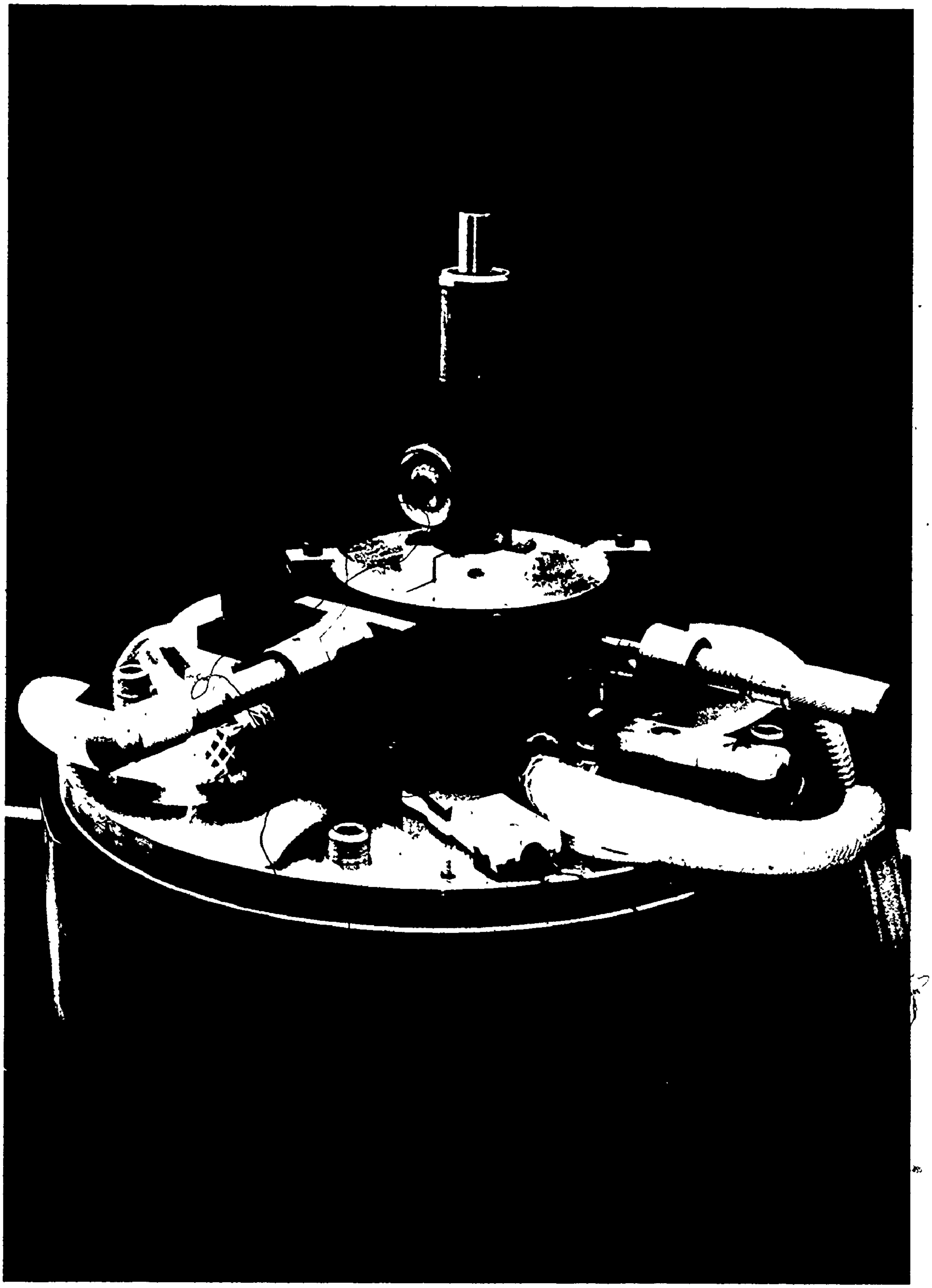

Figure (17) Nucleation Site Location System

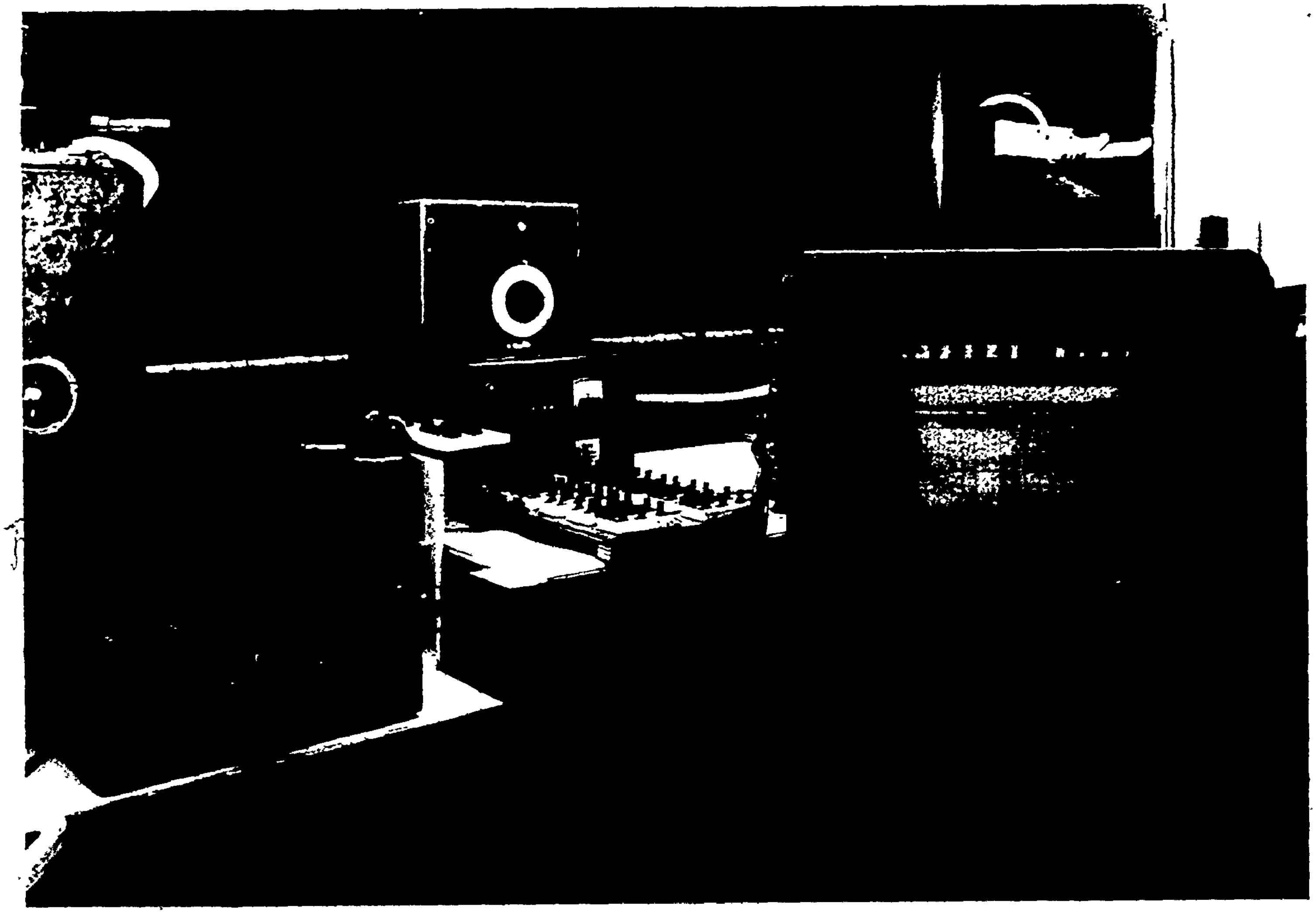

Figure (18) Experimental Arrangement

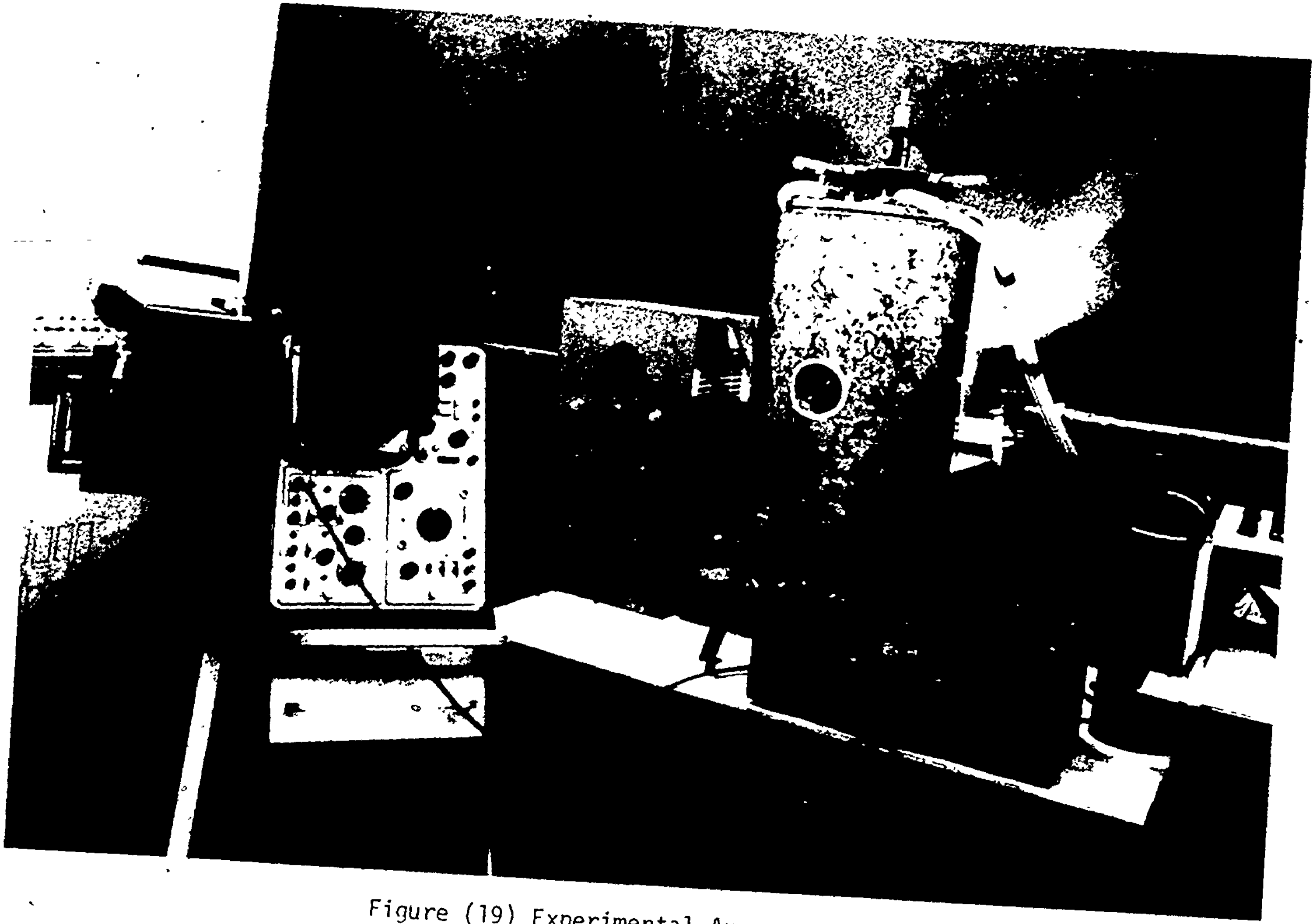

Figure (19) Experimental Arrangement

as shown in Figure (20) were inserted in the block centerline at approximately 1/4 inch intervals from the heating surface. The radial temperature distribution in the neck of the copper block was measured by three thermocouples D, E and F as shown in Figure (20) located at 1/4 inch, 1/2 inch and 3/4 inch radii from the axis in the plane perpendicular to the axis 1/2 inch below the heating surface which included thermocouple B as well.

These six thermocouples were constructed of 30 gauge thermocouple material as shown in Figure (21). Bare 30 gauge thermocouple wire was threaded through lengths of 1/16 inch diameter two-hole ceramic insulators. A drop of Epoxy cement was used to hold the wires in place in the insulator. A small lipped collar of brass was cemented to the ceramic insulator in such a position that when the thermocouple was fully inserted into the positioning hole, the sensing junction was pressed firmly against the bottom of the hole. Three spring loaded wires were used to hold the six thermocouple assemblies snugly in place. Another thermocouple was located in the center of the cartridge heater cluster to provide a check on the maximum block temperature. Two more thermocouples were placed at different radii one on the copper block and the other on the vessel wall in the vermiculite insulation in order to check on radial heat loss from the copper block and two thermocouples were soldered to the underside of the skirt in 1/8 deep holes at 1 3/4 inch and 2 1/4 inch radii respectively.

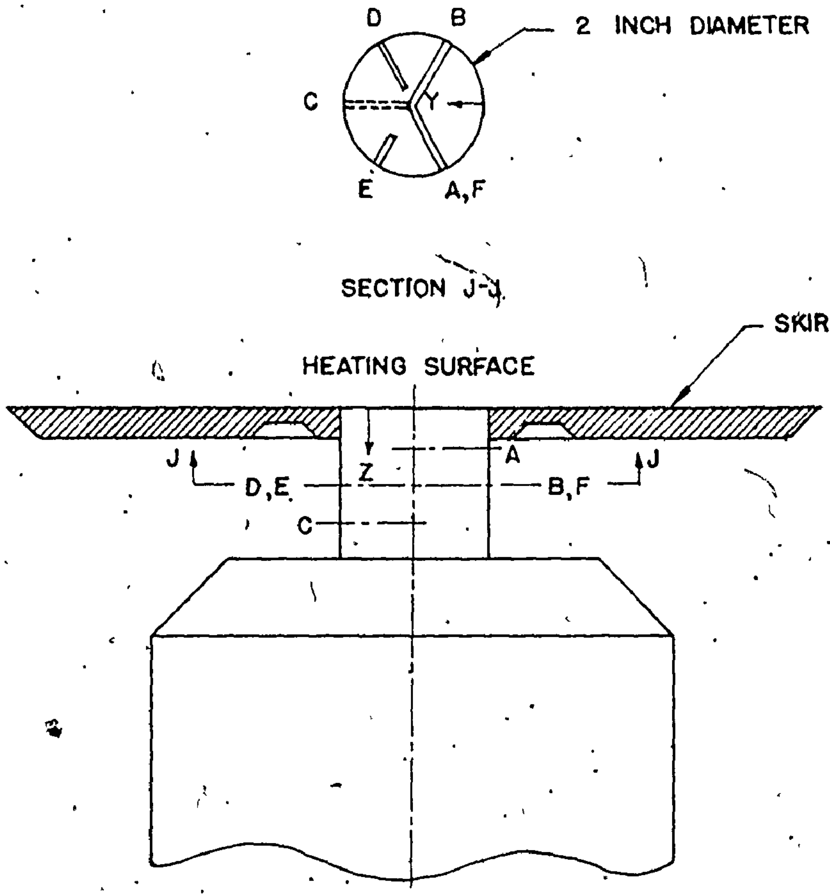

Figure (20) Thermocouple Locations

HOLE	HOLE DEPTH Y (INCH)	VERTICAL DISTANCE Z (INCH)
A	1	1/4
B	1	1/2
C	1	3/4
D	3/4	1/2
E	1/2	1/2
F	1/4	1/2

TABLE (1) LOCATION OF THERMOCOUPLES IN THE NECK OF THE COPPER HEATING BLOCK

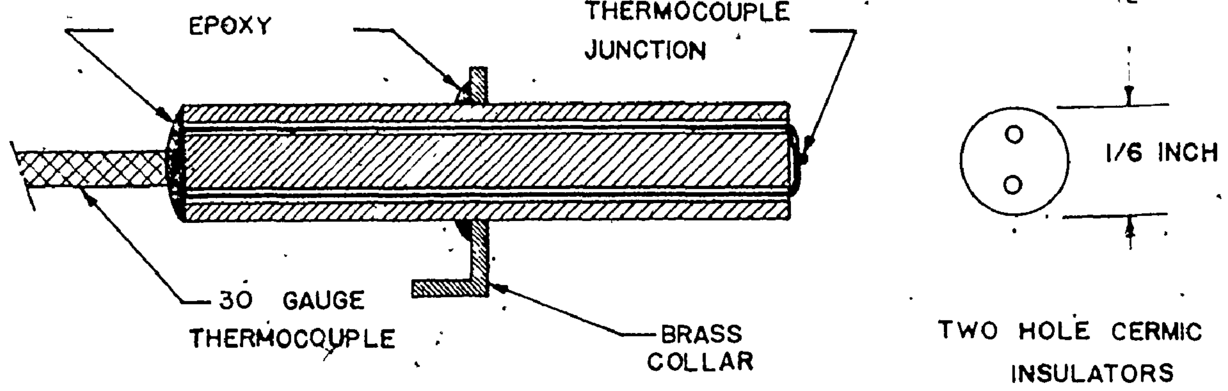

THERMOCOUPLE ASSEMBLY

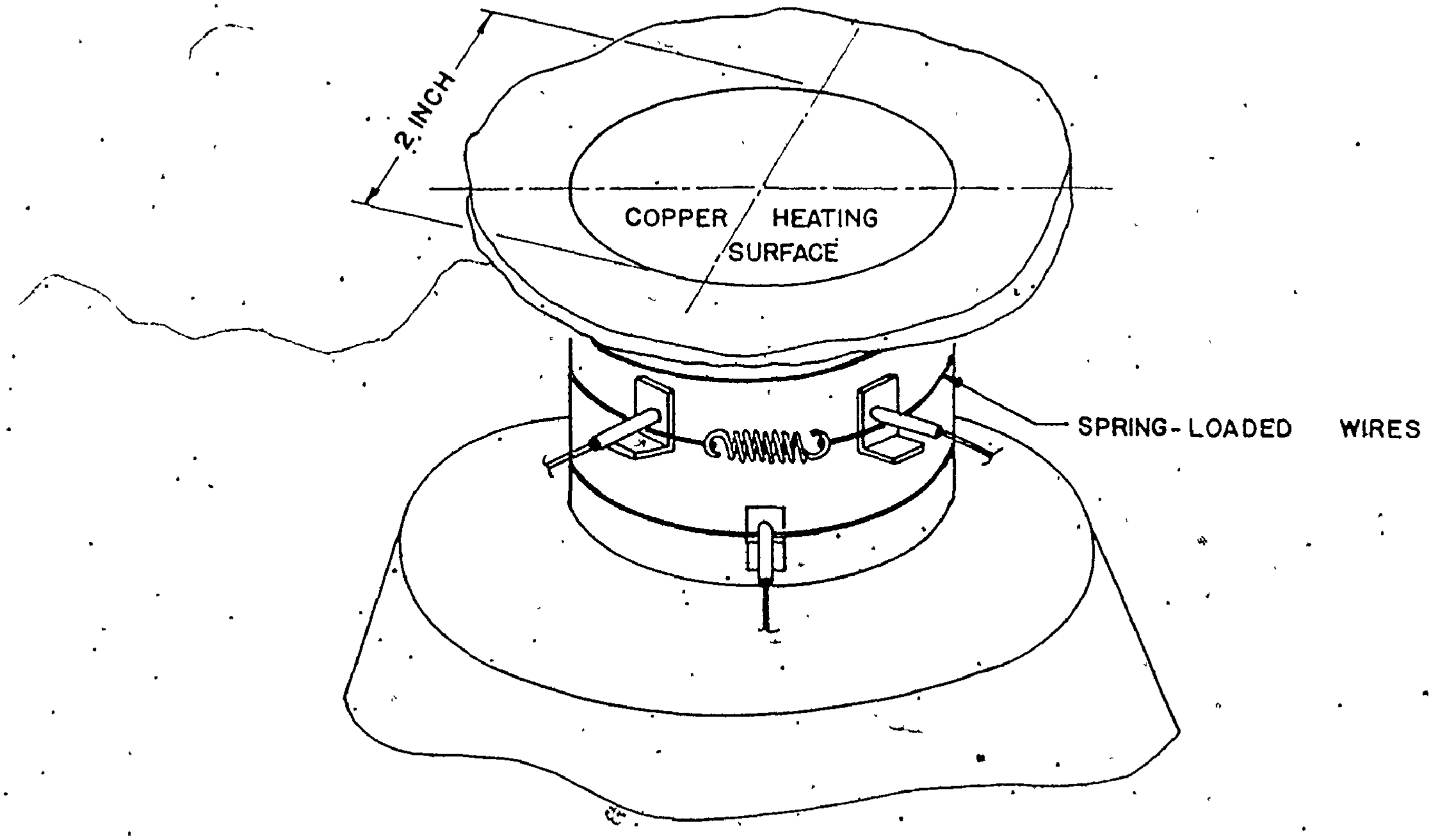

THERMOCOUPLE ASSEMBLY IN POSITION

Figure (21) Thermocouple Assembly

3.4 Power Circuitry and Measurement

Two separate circuits have been used to power the apparatus. The first circuit controlled the block heaters as shown in Figure (22a). The line voltage was applied directly to a 110 volt, 2.1 maximum KVA (Superior Electric Company, type 226T) "Powerstat" variable output autotransformer, which controlled the power input to the thirteen "Firerod" block heaters. A wattmeter was used to measure the power dissipated in the heaters which were connected in parallel. A 10 ampere fuse was used as indicated for protection and an indication lamp was installed in the circuit to show that the line voltage was applied to the primary windings of the "Powerstat".

The second circuit controlled guard heaters as shown in Figure (22b). The line voltage was applied directly to a 110 volt, 1.4 KVA "Powerstat" variable output autotransformer, which controlled the power input to the guard heaters. A 3 ampere fuse was used as indicated also for protection and an indication lamp was installed in the circuit to show that the line voltage was applied to the guard heaters. A wattmeter was connected before the commencement of testing and a graph representing the relationship between the output from the autotransformer and dial indicator was obtained. Afterward, during the test program, the wattmeter was disconnected from electric circuit of the guard heaters, and the graph was used while adjusting the power setting of the guard heaters.

3.5 High Intensity Lamp

A high intensity lamp was used to permit visual observation

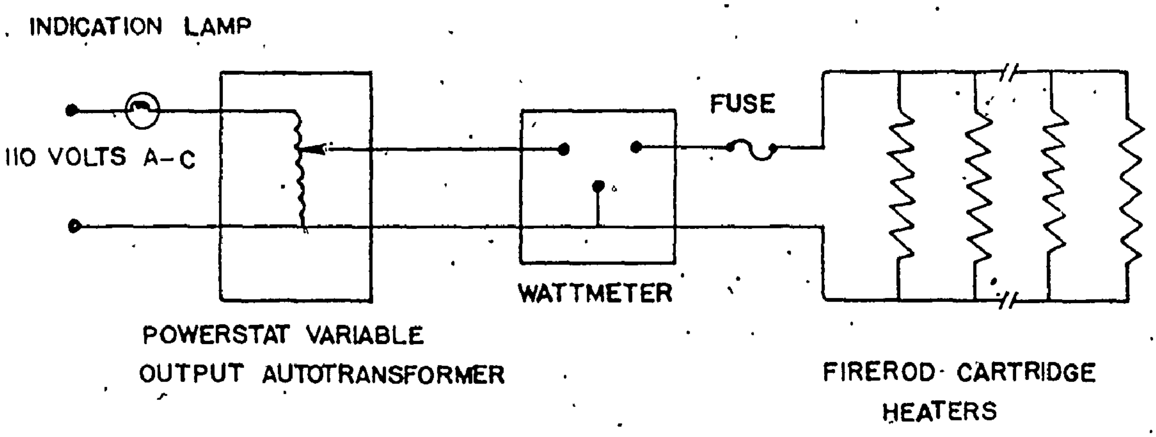

BLOCK HEATER ELECTRIC CIRCUIT

(a)

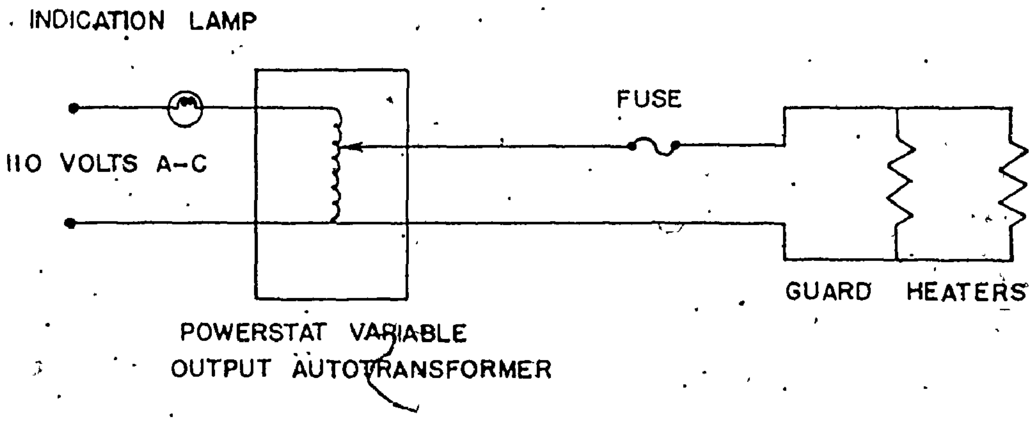

GUARD HEATER ELECTRIC CIRCUIT

(b)

Figure (22) Power Circuit Diagram

of the region above the heating surface. The lamp system is shown in Figure (23) which is comprised of a high voltage power supply and a high intensity mercury vapour lamp protected by an aluminum casing which emits a concentrated beam of white light on to a double convex lens. The focussing lens was located such that a parallel beam of light was projected across the heating surface when the axis of the viewing ports was carefully aligned with the axis of the lens.

3.6 Temperature Measurement System

A typical thermocouple circuit is shown in Figure (24). To conserve chromel constantan wire, a transition was made to single strand nylon insulated thermocouple grade copper wire at ice baths in all thermocouple circuits. The leads were connected to the center copper knife switches which directed the output in two directions. The first direction connected to the twelve channel Honeywell recording potentiometer (Model #15303836) capable of reading with an accuracy of ± 0.1 millivolt. The second direction connected to single channel manual balanced Honeywell potentiometer (Model #2745) capable of reading with an accuracy of ± 0.01 millivolt.

Figure (25) shows the thermocouple switching arrangement in both directions. In one direction, ten thermocouples were connected to ten channels of the twelve channel recording potentionmeter. In the other direction, fourteen terminals were connected in parallel to allow connection to the manually balanced potentionmeter, to obtain the reading of each thermocouple individually.

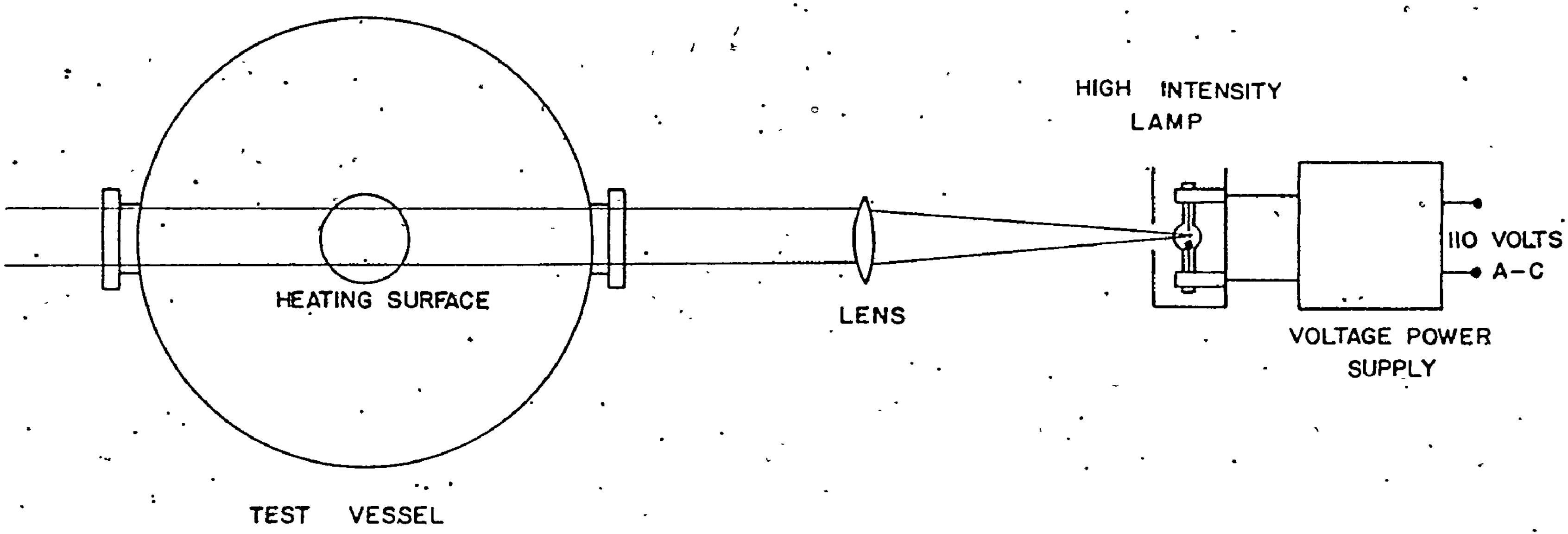

Figure (23) High Intensity Lamp System

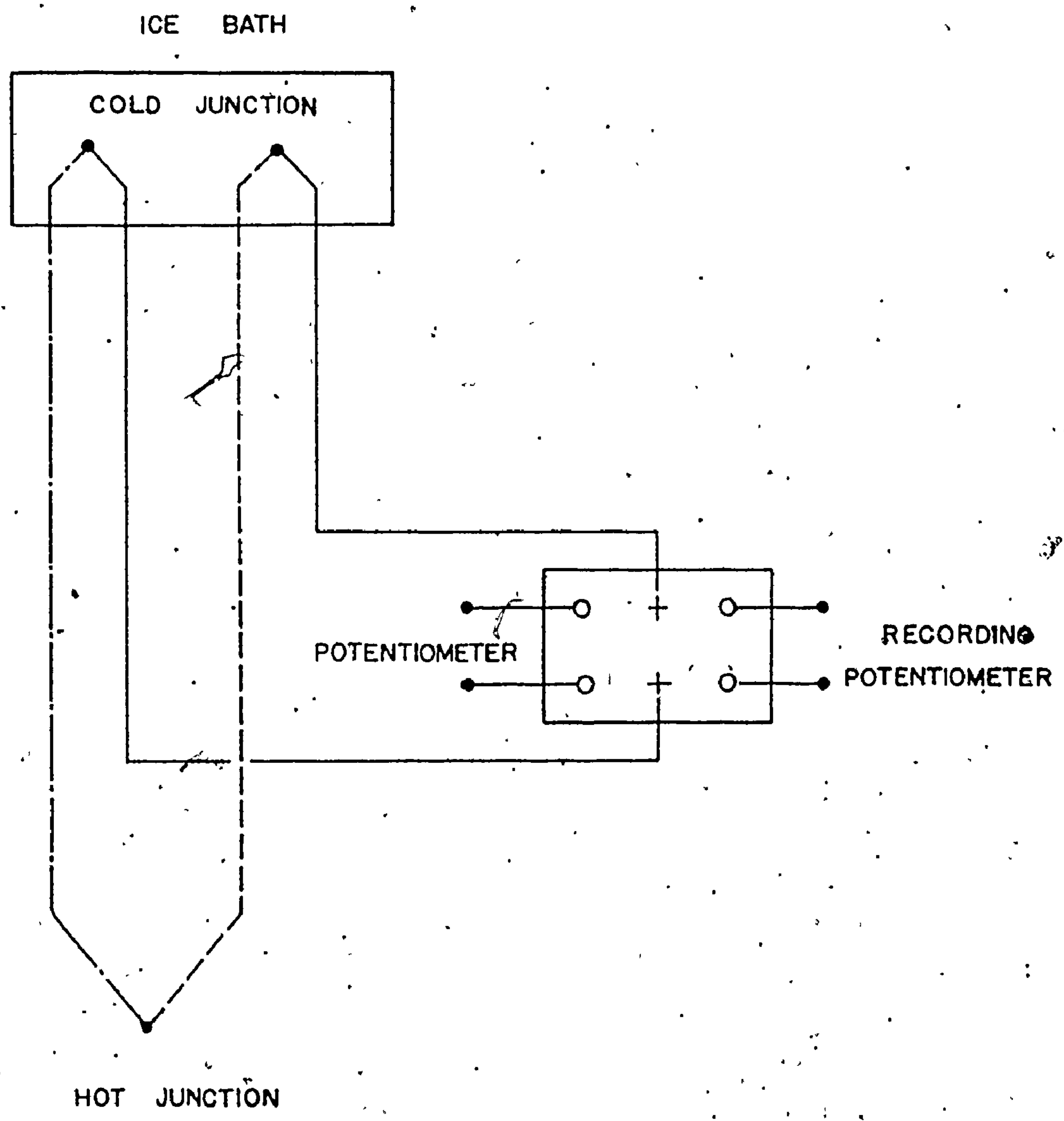

Figure (24) · Thermocouple Circuit

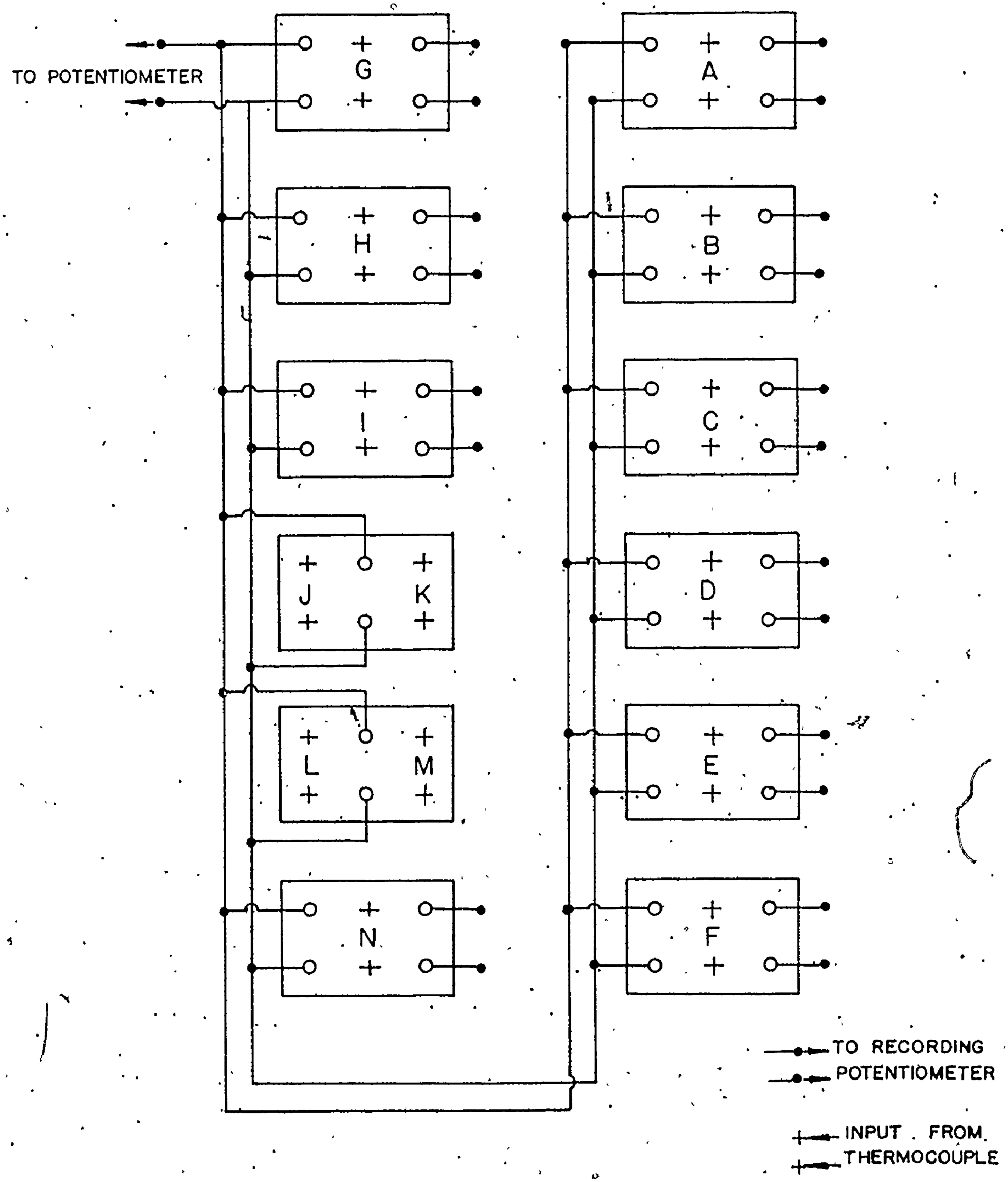

Figure (25) Thermocouples Switching Arrangement.

3.7 Bubble Detection System

Reference [26] reported that electrical probes are widely used for obtaining information on the flow structure in two-phase gas-liquid flows. The conductance probes, which depend for their operation on the fact that the electrical conductivity of a two phase mixture is strongly dependent on the phase distribution, can be used for flow regime detection, void fraction measurement, bubble and drop size determination and film thickness measurement. The same concept was used in the present investigation to determine the locations of the active sites on the heating surface and also the frequency of vapour bubble emission. Appendix C presents design details of the bubble detection probe. The probe circuit as shown in Figure (26) was designed by Shoukri [27].

The probe circuit utilized a signal generator operating at 11,000 Hz and 10 volts to generate the carrier signal. Figure (27) shows the influence of changing carrier frequency on the bubble detection probe response. The resistance R_1 which was connected in parallel with the resistance of the probe which detected the vapour formation between the probe and the heating surface, was used to lower the value of the probe resistance, the capacitor C_1 was used to eliminate any D - C signal in the circuit and the resistance R_2 was used to reduce the signal profile to the zero vertical datum. The resistance R_2 and the capacitor C_2 were introduced in the circuit as part of the filter system.

The output voltage gave an indication of the conductance of

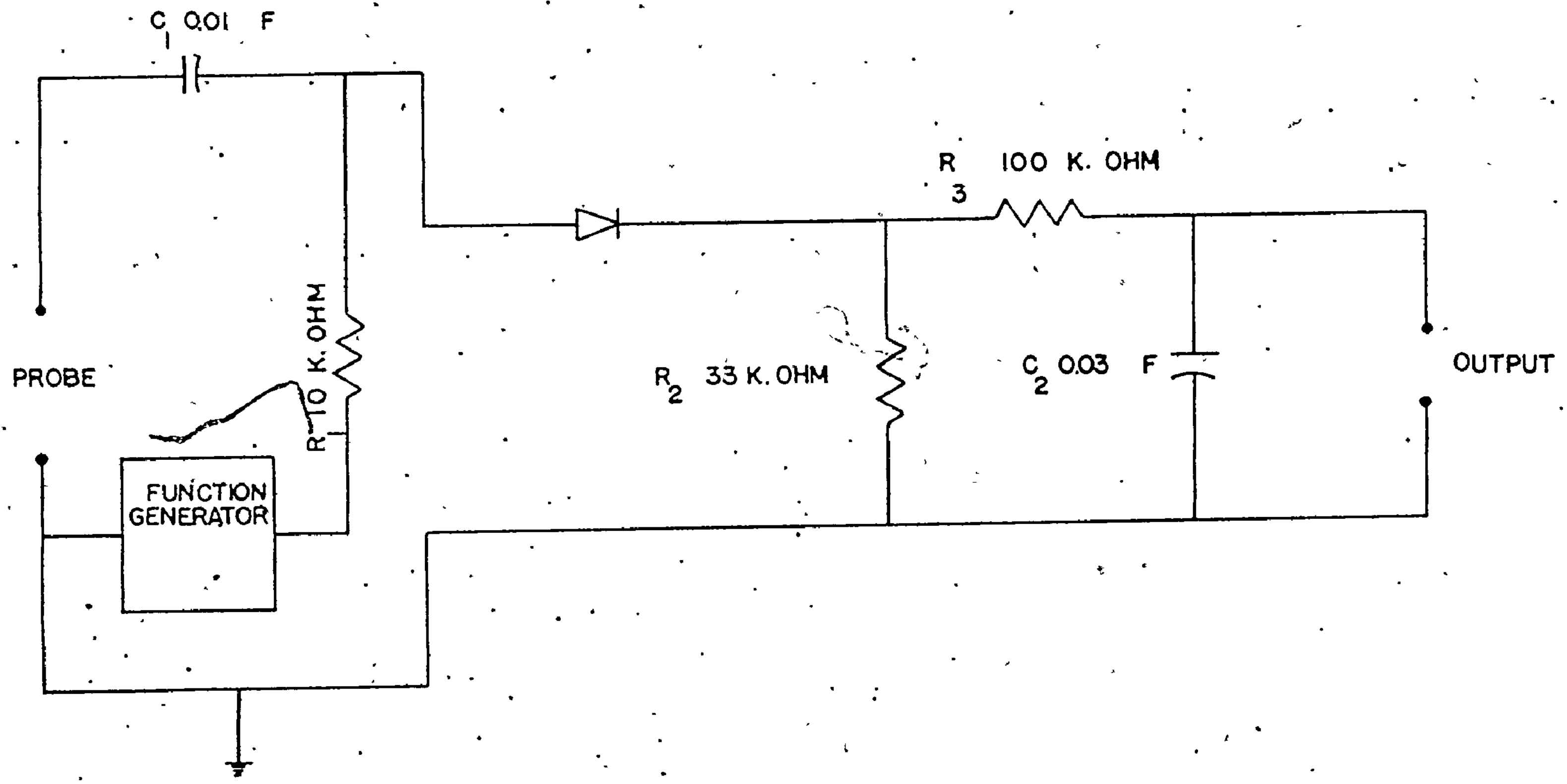

Figure (26) Electrical Probe Circuit

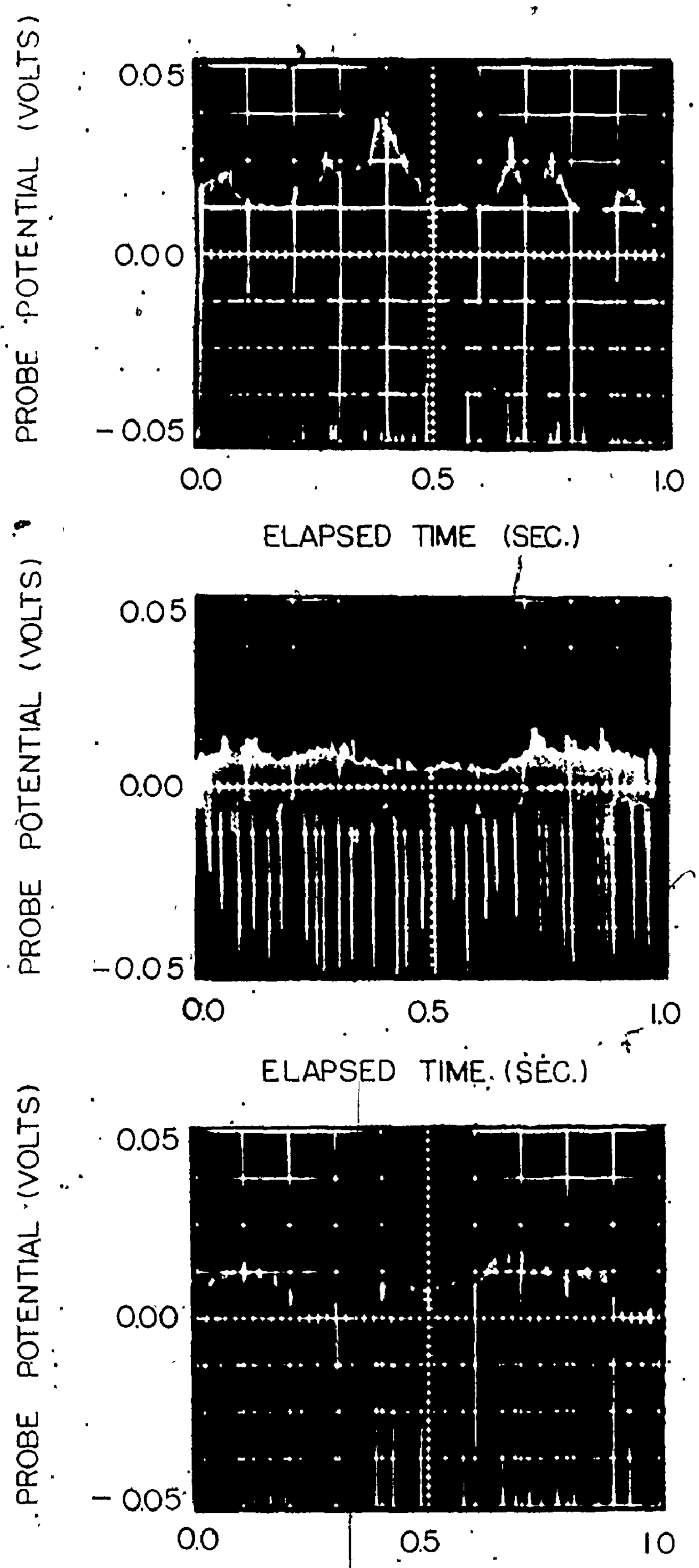

PROBE RESPONSE AT 7,000 Hz CARRIER FREQUENCY

PROBE RESPONSE AT 9,000 Hz CARRIER FREQUENCY

PROBE RESPONSE AT 11,000 Hz CARRIER FREQUENCY

Figure (27) The Effect of Carrier Frequency on the Bubble Detection Probe Response the water or the vapour between the bubble detection probe and the heating surface. Figure (28a) which represents the probe response at some considerable distance from the nucleation site, shows that there was a bridge of water between the bubble detection probe and the heating surface since the signal was invariant during the sampling period. The conductance of the medium within the probe-heating surface gap decreases as the vapour is generated and thus, the output voltage signal decreases intermittently. Figure (28b) shows the probe response at a horizontal distance of approximately 0.010 inches from the nucleation site which yielded the signal shown in Figure (28c). The observation of "strong" fluctuations identified the location of the active site. These fluctuations also enabled the computation of frequency of vapour bubble emission.

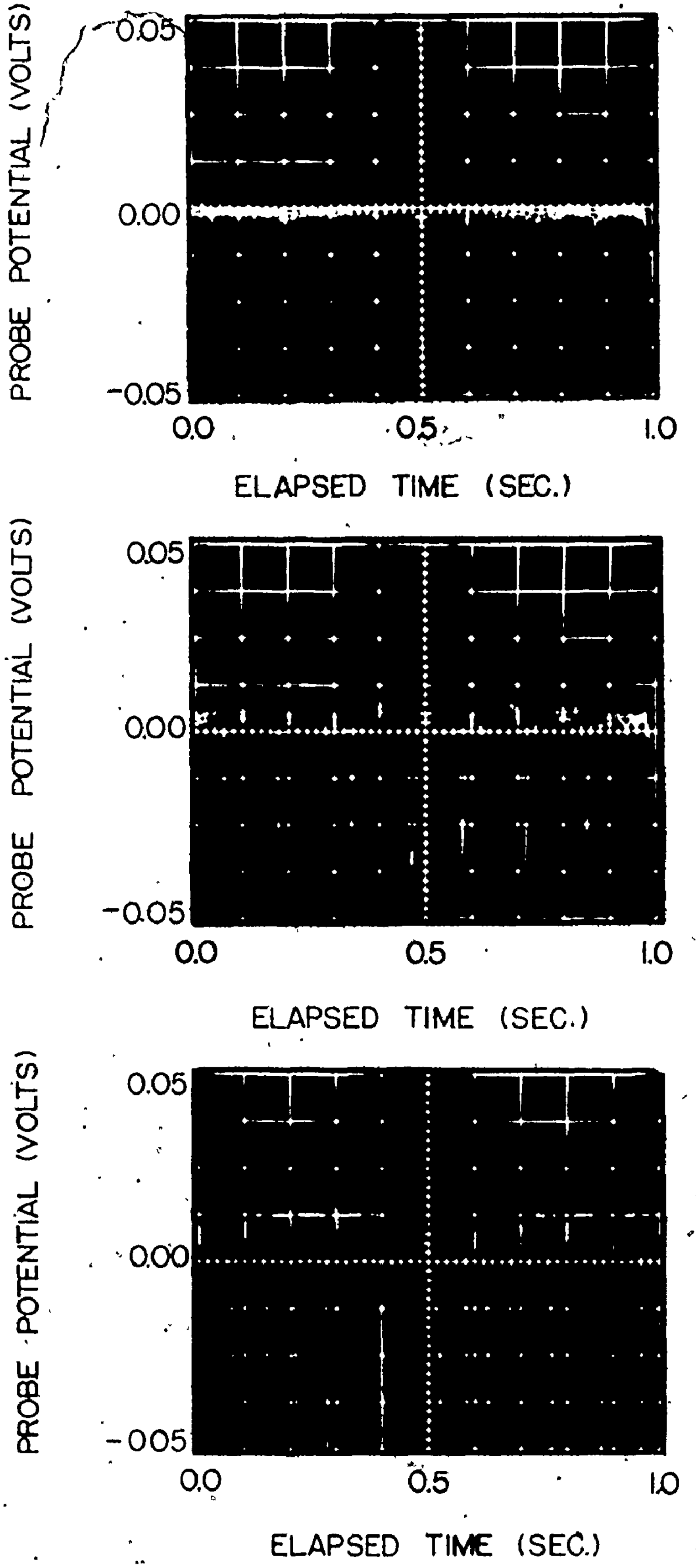

PROBE RESPONSE AT SOME CONSIDERABLE DISTANCE FROM THE NUCLEATION SITE

PROBE RESPONSE AT 0.010 INCHES FROM THE NUCLEATION SITE

PROBE RESPONSE AT THE CENTER OF THE NUCLEATION SITE

Figure (28) The Influence of Probe Displacement From Nucleation Site

CHAPTER 4

TEST CONDITIONS

This experimental investigation was subdivided into two series of tests. In the first series, the subcooling was varied at constant heat flux for three different levels of heat flux setting. The three levels of heat flux were selected to examine the three different boiling regions investigated by Gaertner [28], the discrete bubble region (20,300 BTU/hr. ft.^{2}), the transition region (52,600 BTU/hr. ft.^{2}) and the vapour mushroom region (105,600 BTU/hr. ft.^{2}). The range of subcooling differed from one level of heat flux to another. It was experimentally difficult to distinguish the distribution of active sites over the heating surface due to the large number of active sites on the heating surface corresponding to the intermediate and high heat flux levels. Also it was experimentally difficult to distinguish the distribution of active sites over the heating surface at high levels of subcooling due to the decrease of bubble departure diameter.

The second test series was carried out to examine the active site patterns for two cases in a single experimental run. In the first case, the effect of changing heat flux level was investigated while the subcooling remained the same. In the second case, the effect of changing subcooling was investigated, while the level of heat flux remained the same.

The nominal values of the various parameters investigated in the tests discribed above are listed in Table (2) which follows.

TABLE 7(2.)

NOMINAL VALUES OF TEST CONDITIONS

1. SATURATED AND SUBCOOLED BOILING TESTS

Test No.	Heat Flux Q/A (BTU/hr. ft.^{2})	Subcooling $(T_s - T_\infty)$ (°F)
A 1	20,300	0
2	20,300	15
3	20,300	31
B 1	52,600	3
2	52,600	15
3	52,600	30
4	52,600	51
C 1	105,600	15
2	105,600	31
3	105,600	51
4	105,600	71

2. ACTIVE SITE PATTERN TESTS

Test No.	Heat Flux Q/A (BTU/hr. ft.^{2})	Subcooling $(T_s - T_\infty)$ (°F)
D 1	20,300	20
2	52,600	20
3	105,600	20
E 1	52,600	3
2	52,600	36

CHAPTER 5

TEST PROCEDURES

The vessel was filled approximately to a depth of 6 inches with deionized distilled water containing 0.1 gm. of salt/litre. At the beginning of each test, the level of water inside the vessel was checked to confirm the appropriate water level. The cooling water valves which were used to control the flow to the subcooling and vapour condenser coils were completely closed. The high intensity lamp, the signal generator and the oscilloscope were turned on. The signal generator was adjusted at 11 k Hz and 10 volts. The oscilloscope was adjusted at 0.1 second/division and 0.01 volt/division. The bubble detection probe was lowered down until it came in contact with the heating surface, after which it was raised up a very small distance.

The X-Y stage was employed to move the bubble probe in different directions to check that there was no contact between the probe and the heating surface. The copper block heaters and guard heaters were turned on. A copper block heater setting of approximately 150,000 BTU/hr. ft.^{2} was established to heat up the boiler assembly quickly. In all the tests, the guard heaters were set to yield a heat input of 426 BTU/hr. All the thermocouples were switched in the direction of the recording potentiometer after which the recording potentiometer was turned on. A heat up time of approximately two hours was allowed to elapse in order to achieve steady state conditions, and ensure that the nucleation sites were properly activated at the beginning of each test, after which the heat input was reduced to the desired level. Two hours were required for the system to regain steady state after a change in heat flux or subcooling took place. Then the readings of all the thermocouples were taken from the recording potentiometer. In addition, the thermocouple readings were obtained individually by using the manually balanced potentiometer.

The X-Y stage was adjusted to place the bubble detection probe in the zero reference position. The Y micrometer was fixed at it's zero reference position and the X micrometer was moved very slowly until a significant deflection in the voltage appeared on the oscilloscope screen. X and Y micrometers were moved very small increments in both directions until a strong signal appeared. The reading of X and Y micrometer was recorded on a data sheet and it was deemed to represent the position of the particular active site.

Each deflection of the oscilloscope beam represented a bubble emitted at that time and consequently, the number of the deflections observed on the oscilloscope screen over a fixed time interval could be interpretted as the bubble emission frequency. Ten readings of the signal from each active site were taken. Afterward, the Y micrometer was returned to the original setting and the X micrometer was moved in the X direction once again. The same procedure was continued through a one inch scan. Afterwards the Y micrometer was moved 0.025 inches and the X micrometer made another one inch scan. These steps were repeated through a one inch scan in Y direction. At the conclusion of the scanning procedure the heating area (1X1) inch square had been examined by the bubble detection probe and the locations of all of the active sites detected had been recorded. Some pictures were taken of the oscilloscope screen for the cases of no active sites, active sites with low frequency values and active sites with high frequency values. A sample of the photographs obtained are shown in Figure (29). At the end of the test all the thermocouple readings were recorded once again, using the manually balanced potentiometer. The ambient temperature was measured using a mercury in glass thermometer, and the reading of the barometeric pressure was obtained in order to compute the saturation temperature of the water corresponding to the atmospheric pressure.

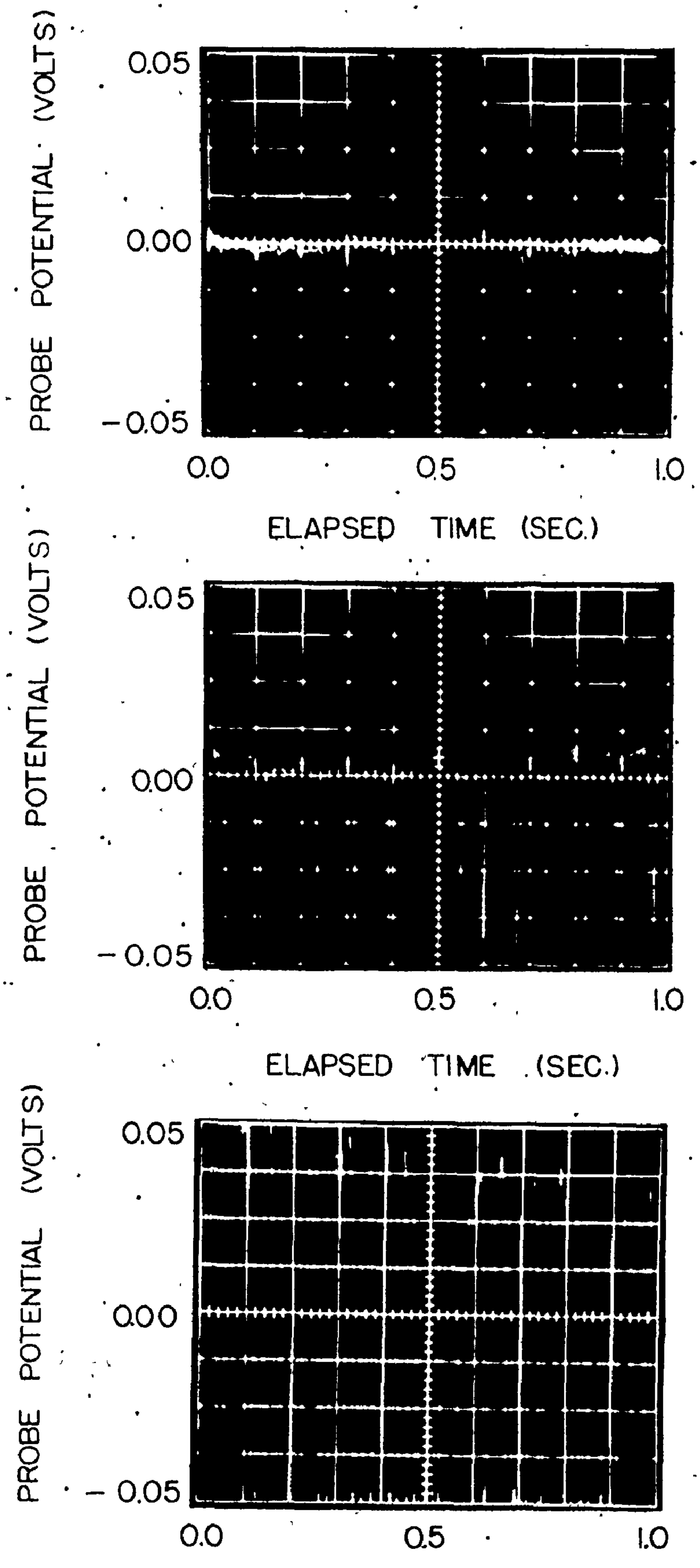

PROBE RESPONSE AWAY FROM THE ACTIVE SITE

PROBE RESPONSE AT ACTIVE SITE WITH LOW BUBBLE FREQUENCY

PROBE RESPONSE AT ACTIVE SITE WITH HIGH BUBBLE FREQUENCY

Figure (29) Bubble Frequency at Different Locations on the Heating Surface

CHAPTER 6

DATA REDUCTION

The following section describes the methods used in calculating the heat flux, surface superheat, liquid subcooling, active site density, bubble frequency and bubble flux density.

6.1 Heat Flux

The heat dissipated at the heating surface was calculated from the total power dissipation by subtracting the total heat losses from the system using the same procedure devised by Wiebe [25]

$$[\frac{Q}{A}]_{Actual} = [\frac{Q}{A}]_{Total} - [\frac{Q}{A}]_{Loss} \qquad \text{----17}$$

The total heat losses to the surroundings were computed as the summation of the heat loss from the stainless steel skirt, the heat loss from the bottom of the heater assembly and the heat loss through the vermiculite. Appendix A presents detailed numerical calculations for the heat loss evaluation procedure.

6.2 Surface Superheat

The surface superheat ΔT_{sup} is given by

$$\Delta T_{sup} = T_w - T_s \qquad \text{----18}$$

where T_w is the temperature of the heat transfer surface calculated by extrapolating the axial temperature gradient in the neck of the heater block assuming the flow of heat to be one dimensional. Wiebe [25] performed his experimental investigation with the same heating surface used in the present work and measured the heating surface temperature by means of a miniature thermocouple positioned on the heating surface. Wiebe found that the difference between the measured and extrapolated surface temperature was less than one degree Fahrenheit. The temperature T_s is the saturation temperature obtained from a plot of saturation temperature versus the pressure evaluated at the barometric pressure reading.

6.3 Liquid Subcooling

The bulk liquid subcooling ΔT_{sub} is given by

$$\Delta T_{sub} = T_s - T_\infty \qquad ----19$$

where T_s is the saturation temperature defined above and T_∞ is the temperature of the bulk liquid measured by two thermocouples which were located at 2 inches and 4 inches above the heating surface. These measurements adequately represented the bulk liquid temperature as demonstrated in Appendix (B).

6.4 Active Site Density

The locations of the active sites on the heating surface (1 X 1) inch square were obtained by using the bubble detection probe. The active site density $\frac{N}{A}$ was determined by counting the active sites located within the (1 X 1) inch square and dividing by the area.

6.5 Bubble Frequency

The average frequency of vapour bubble emission $\overline{f}$ for the entire heating surface was obtained by summing the average frequency of vapour bubble emission for each of the active sites located within the (1X1) inch square and dividing by the total number of active sites. The average frequency of vapour bubble emission for each active site was obtained by averaging ten different measurements of the number of bubbles detected within the arbitrarily chosen one second sampling periods as described before.

6.6 Bubble Flux Density

The heating surface was subdivided into one hundred small (0.1 X 0.1) inch squares. From the average frequency of vapour bubble emission data, the number of vapour bubbles emitted per second from each of the small squares were counted. These counts represented the bubble flux density in each of the small squares and the summation for all the hundred squares represented the bubble flux density on the entire heating surface.

CHAPTER 7

RESULTS

In this section, the experimental data is presented with little comment. Analysis and discussion of the data are presented in Chapter 8. Both the experimental and calculated data are tabulated in Appendix (D).

Figure (30) shows the characteristic boiling curve in the form of a plot of heat flux Q/A as a function of surface superheat $(T_W - T_S)$. As is customarily observed, the heat flux increases as superheat increases.

Figure (31) shows the effect of subcooling $(T_S - T_\infty)$ on the surface superheat $(T_W - T_S)$ for three different levels of heat flux Q/A. At constant heat flux, the surface superheat increases slightly with the increase of subcooling and then decreases again.

Figure (32) presents a sample distribution of the active nucleation site population on the heating surface for test B1. The distribution of active sites among 25 squares and 100 squares can be seen at a glance.

Figure (33) presents the distribution of bubble flux density within the (1 X 1) inch square.

Figure (34) and Figure (35) present the relationship between the total active site density N/A, the heat flux Q/A and the surface superheat $(T_S - T_\infty)$ respectively. The active site density

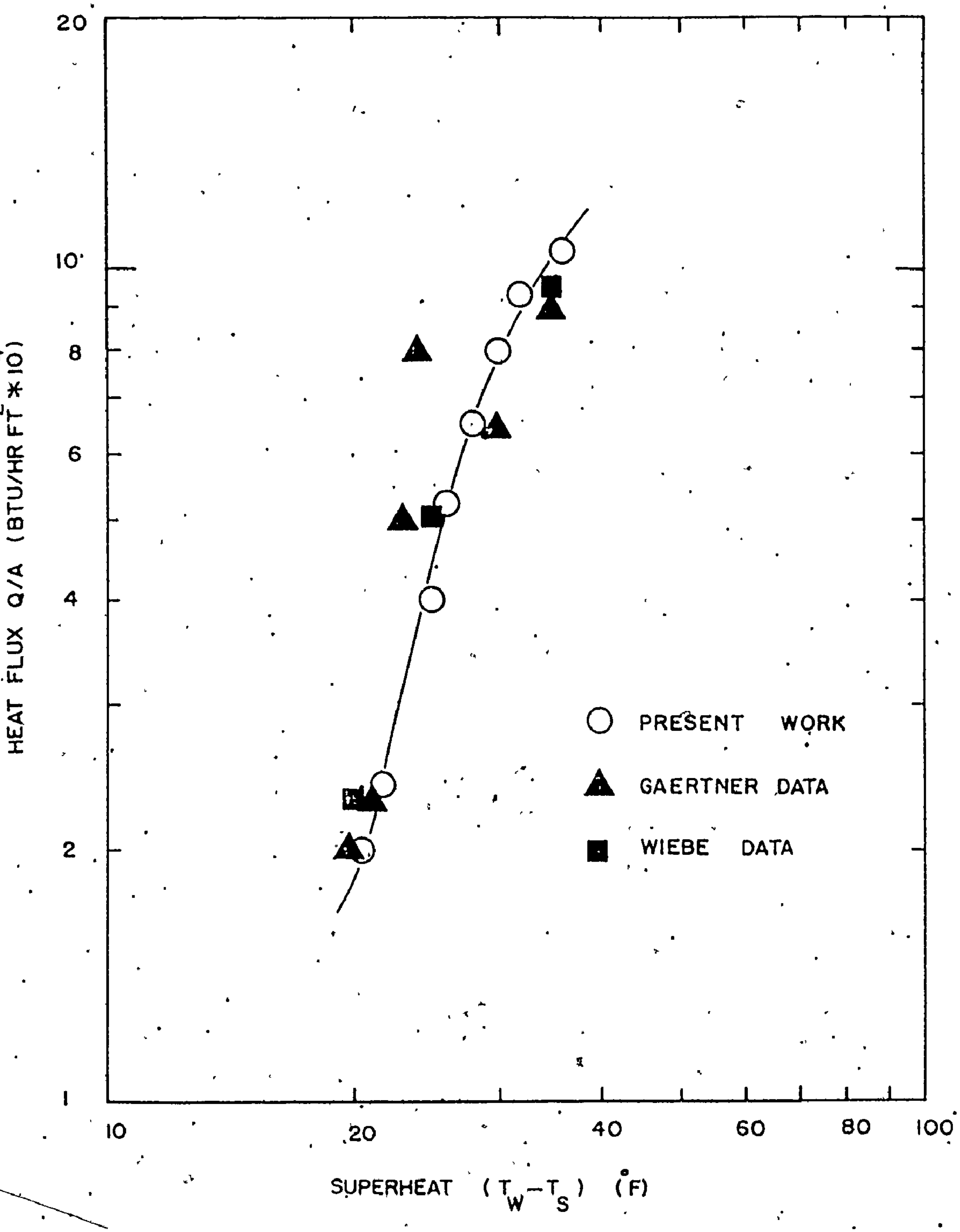

Figure (30) Characteristic Boiling Curve for Present Investigation

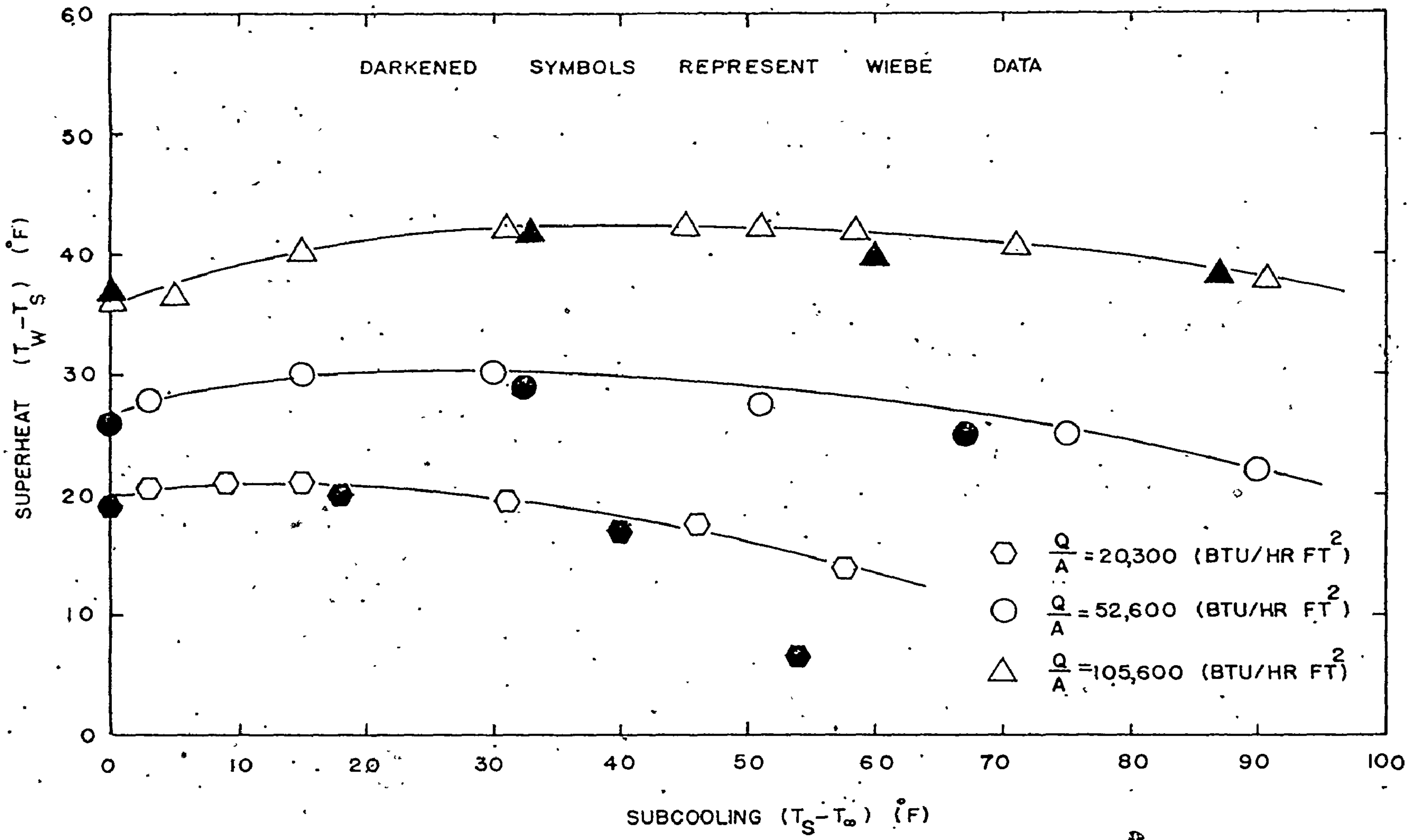

Figure (31) Variation of Surface Superheat With Bulk Subcooling

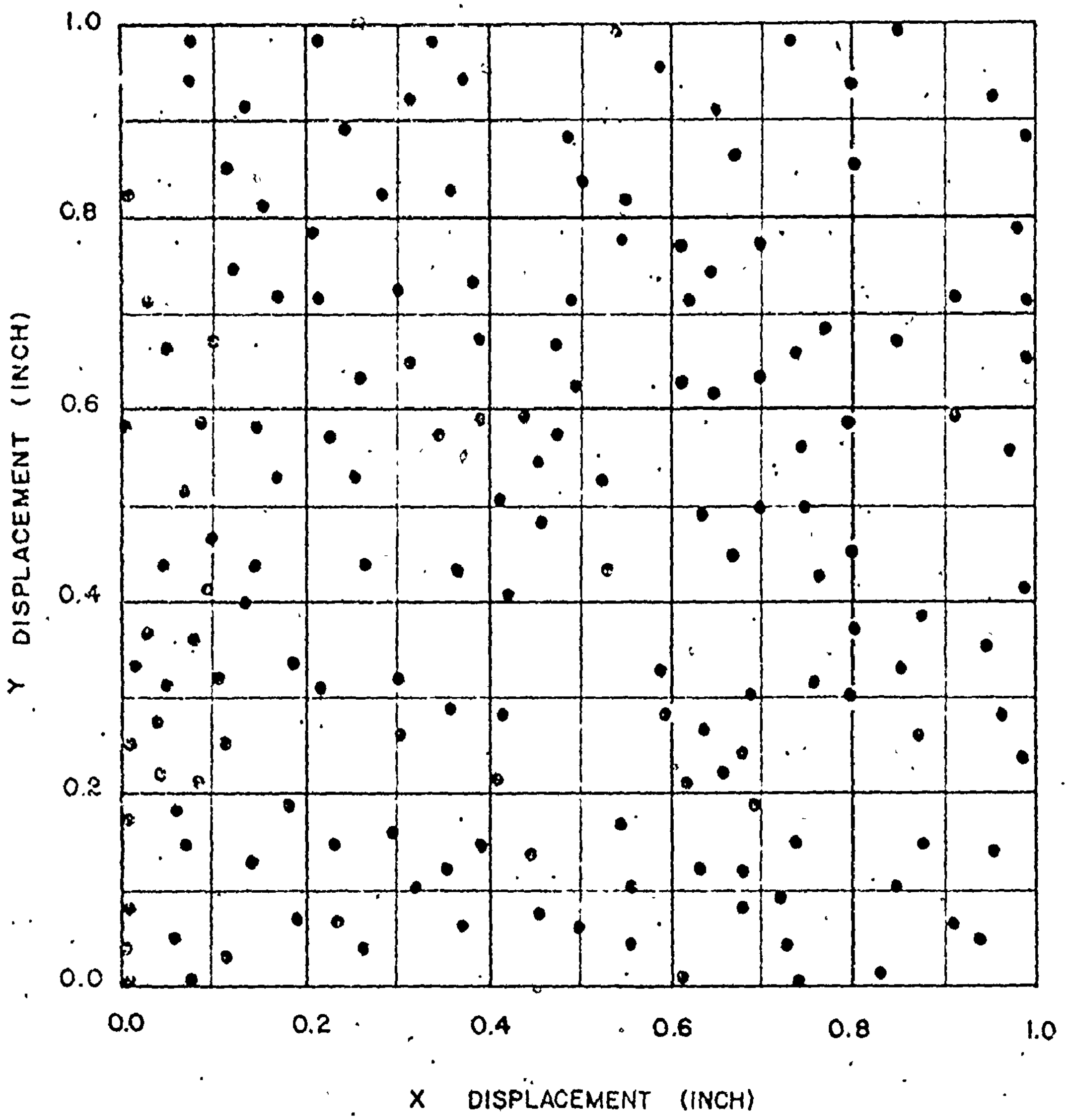

TEST B1

Figure (32) Distribution of Active Nucleation Sites

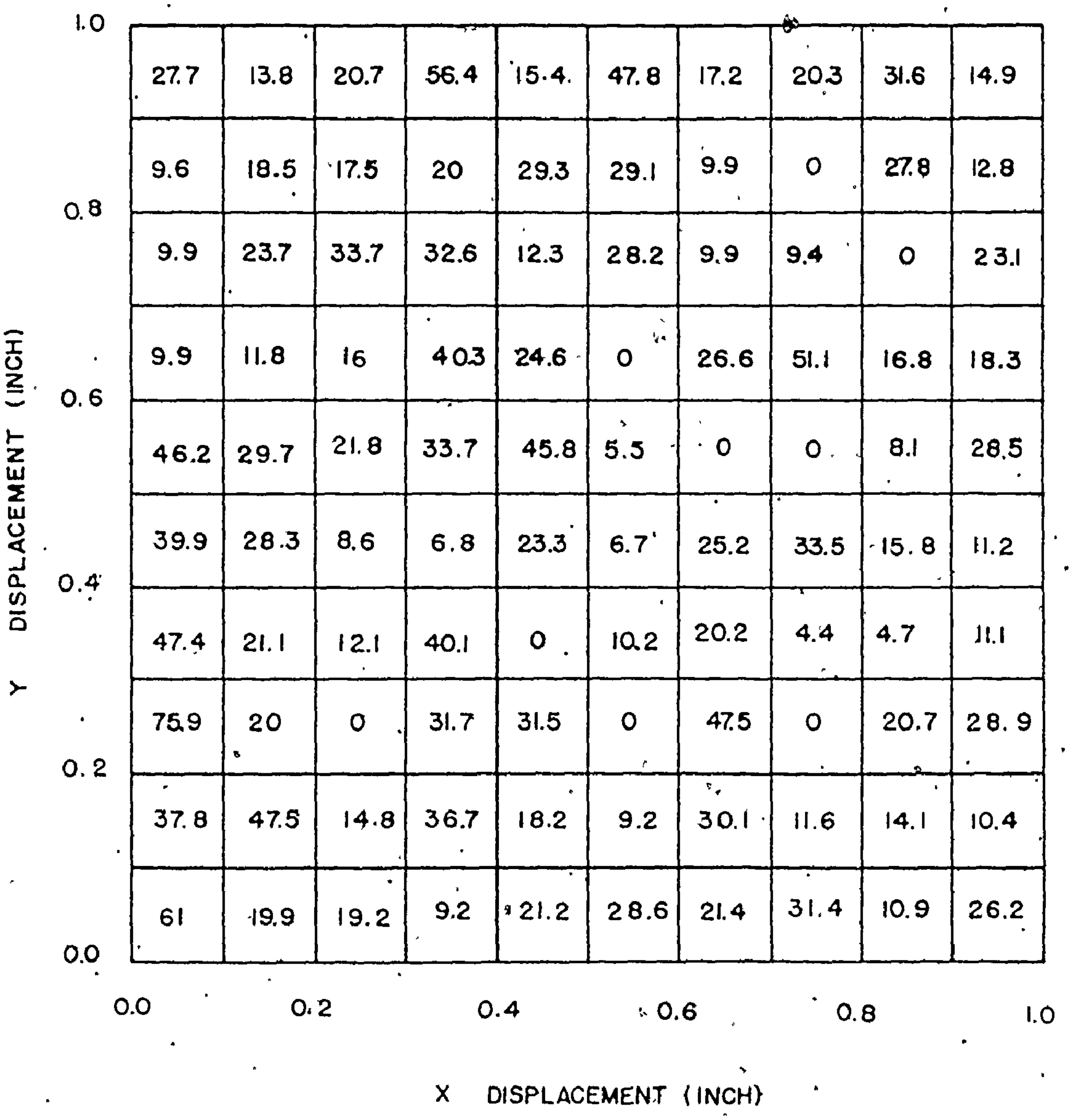

27.7	13.8	20.7	56.4	15.4	47.8	17.2	20.3	31.6	14.9
9.6	18.5	17.5	20	29.3	29.1	9.9	0	27.8	12.8
9.9	23.7	33.7	32.6	12.3	28.2	9.9	9.4	0	23.1
9.9	11.8	16	40.3	24.6	0	26.6	51.1	16.8	18.3
46.2	29.7	21.8	33.7	45.8	5.5	0	0	8.1	28.5
39.9	28.3	8.6	6.8	23.3	6.7	25.2	33.5	15.8	11.2
47.4	21.1	12.1	40.1	0	10.2	20.2	4.4	4.7	11.1
75.9	20	0	31.7	31.5	0	47.5	0	20.7	28.9
37.8	47.5	14.8	36.7	18.2	9.2	30.1	11.6	14.1	10.4
61	19.9	19.2	9.2	21.2	28.6	21.4	31.4	10.9	26.2

TEST B1

Figure (33) Distribution of Bubble Flux Density

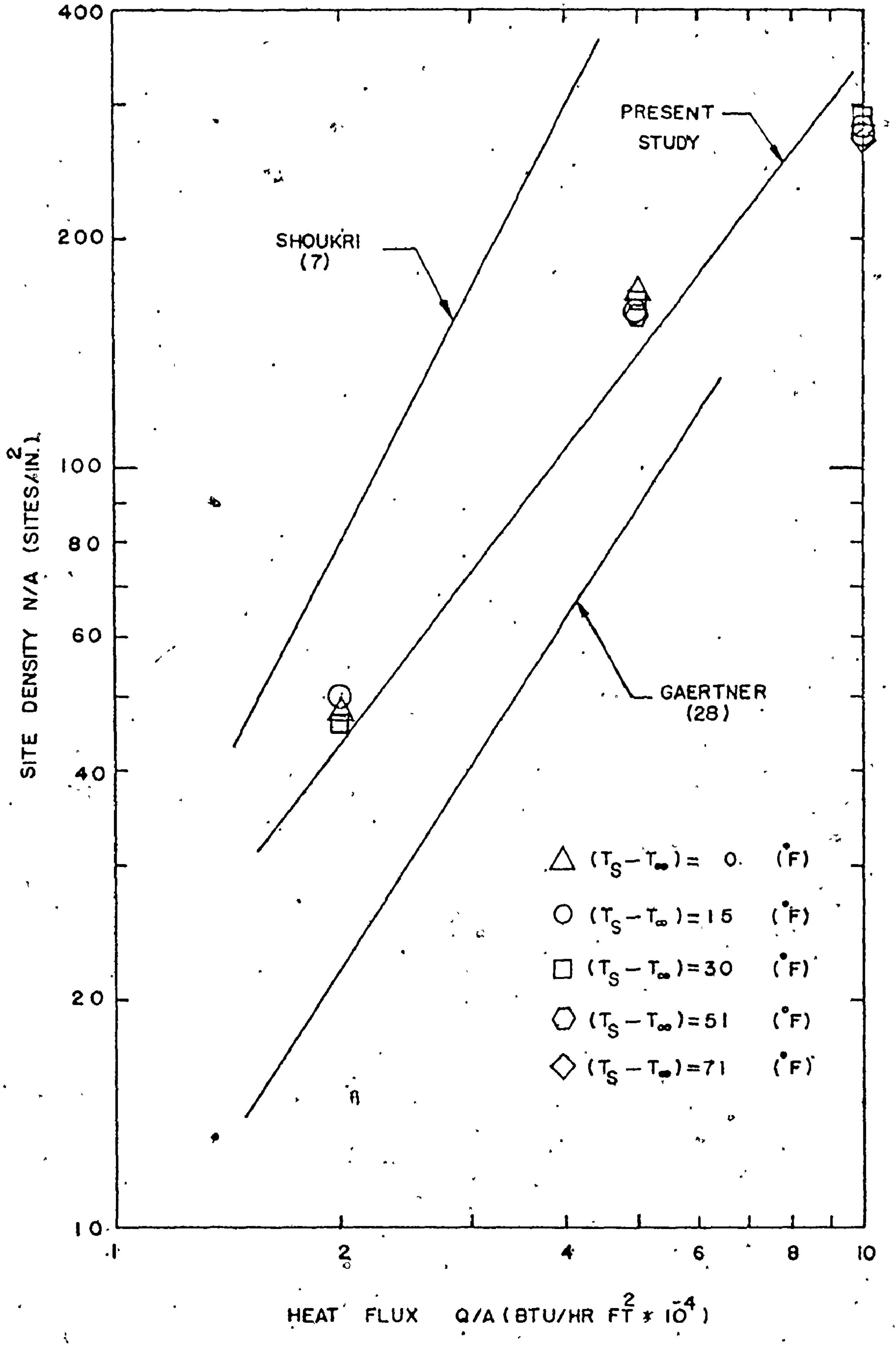

Figure (34) Active Site Density Versus Heat Flux

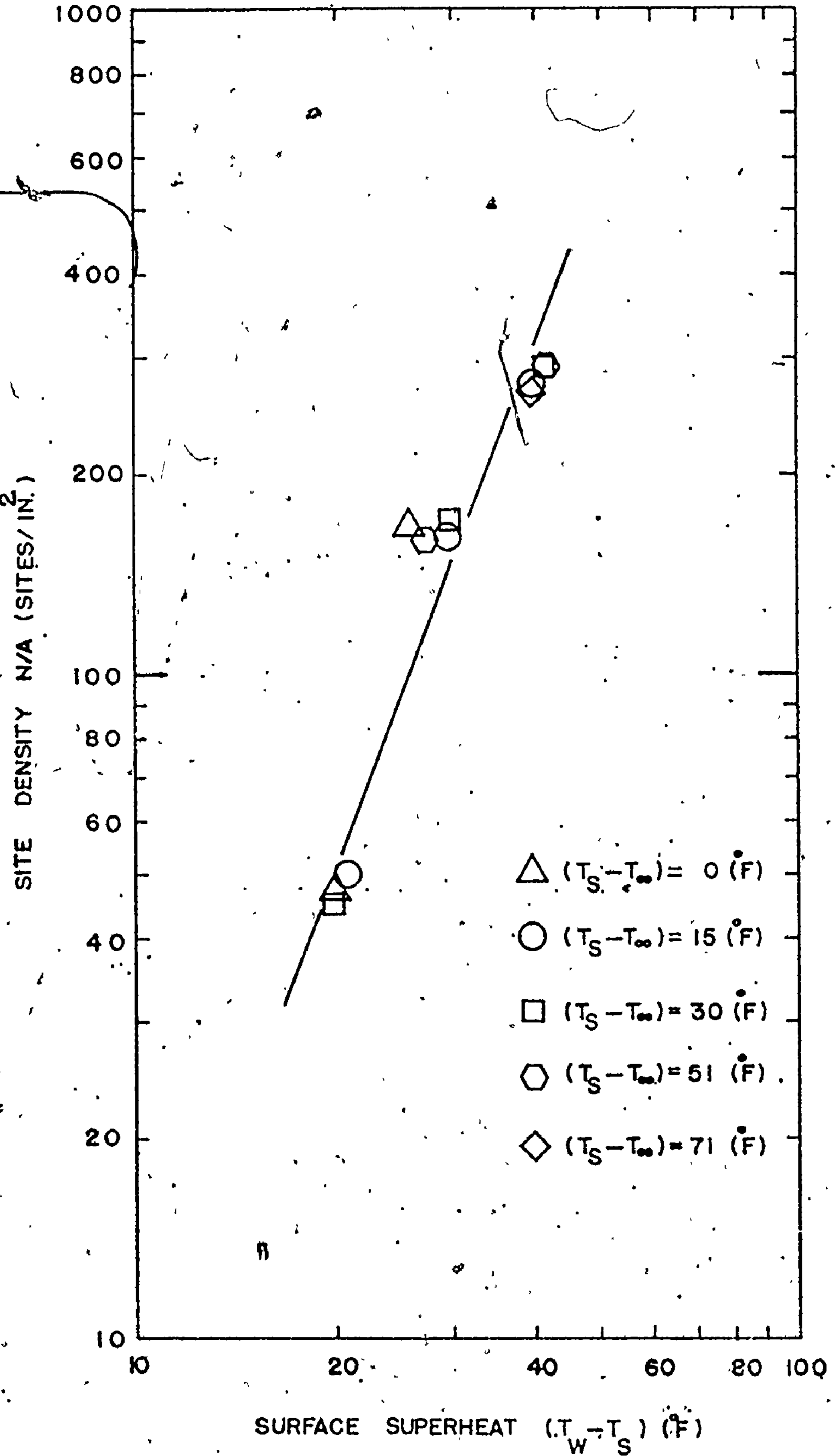

Figure (35) Active Site Density Versus Surface Superheat increases with the increase of heat flux and surface superheat.

Figure (36) shows the effect of subcooling on the active site density for three different levels of heat flux. The results indicate a slight effect of subcooling on the active site density.

Figure (37) and Figure (38) present the effect of the heat flux Q/A and superheat $(T_s - T_\infty)$ on the average nearest-neighbor distance $\overline{S}$. The average nearest-neighbor distance decreases with increasing heat flux and superheat at first, after which it decreases much less rapidly.

Figure (39) shows the effect of subcooling on the average nearest-neighbor distance for the three different levels of heat flux. The results indicate a slight effect of subcooling on the average nearest-neighbor distance.

Figure (40) shows the effect of subcooling on the average frequency of vapour bubble emission for three different levels of heat flux. The results indicate that the average frequency increases with the increase of subcooling and then decreases again with further increase of subcooling.

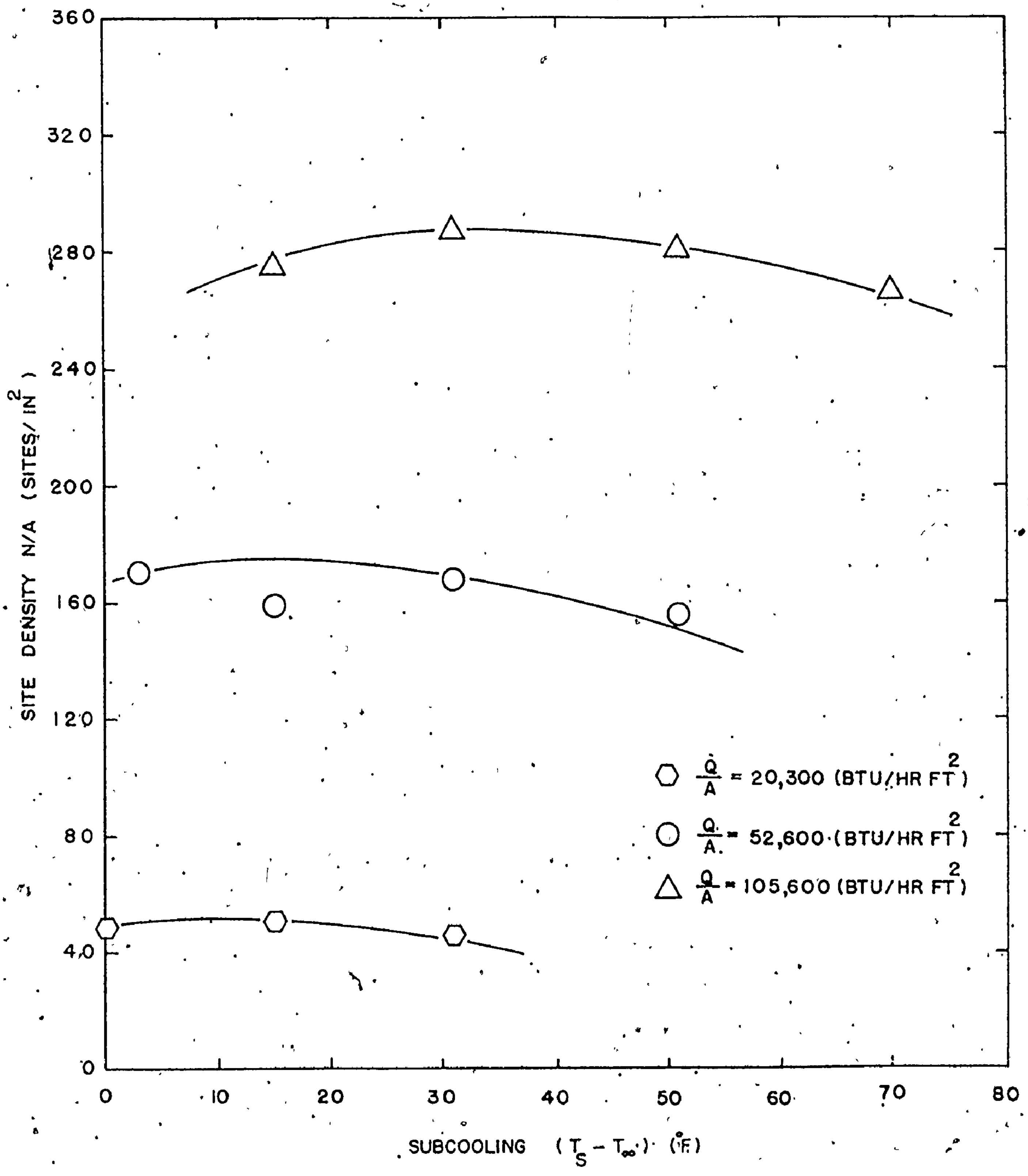

Figure (36) Variation of Active Site Density With Bulk Subcooling

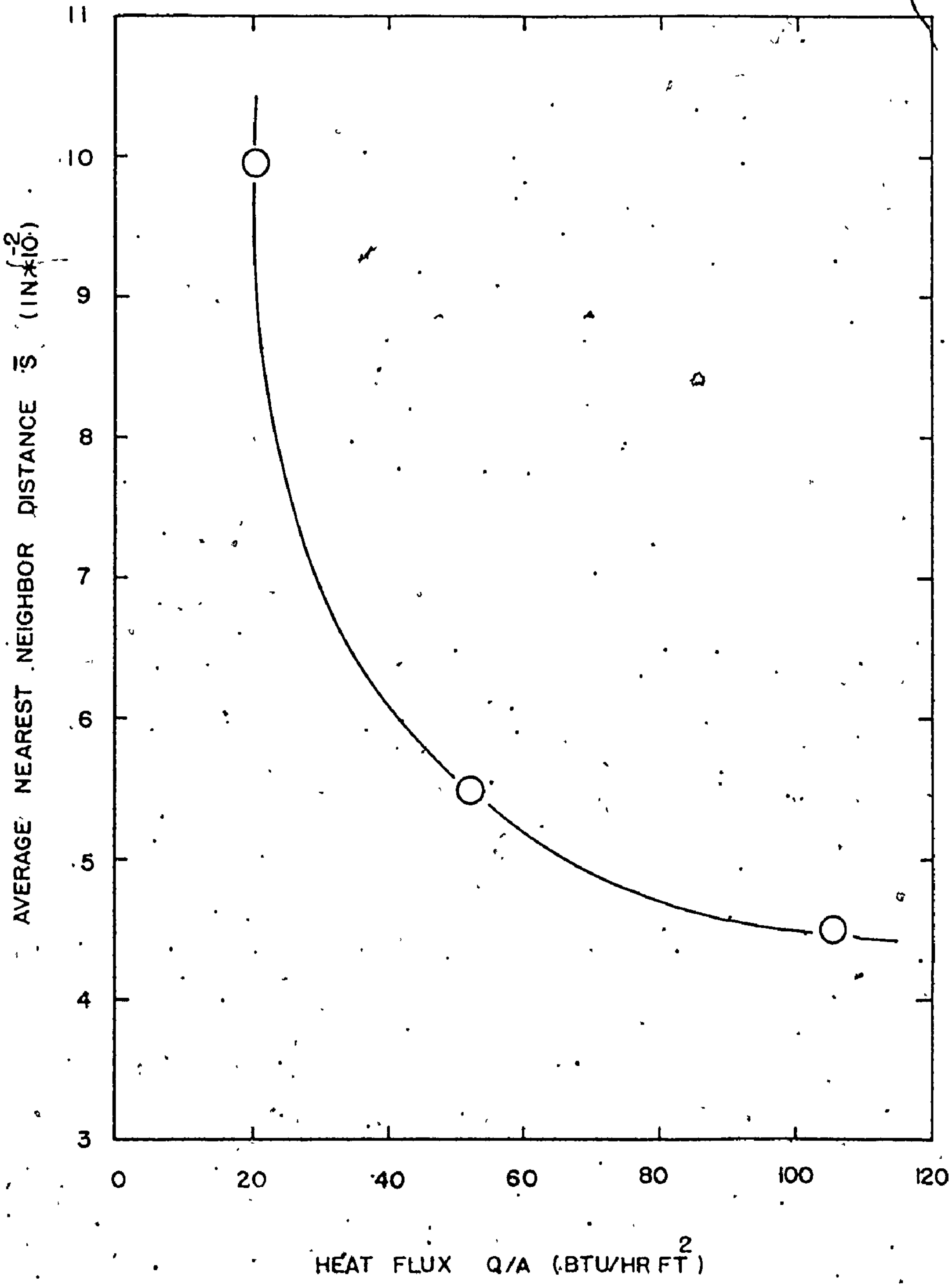

Figure (37) Average Nearest-Neighbor Distance

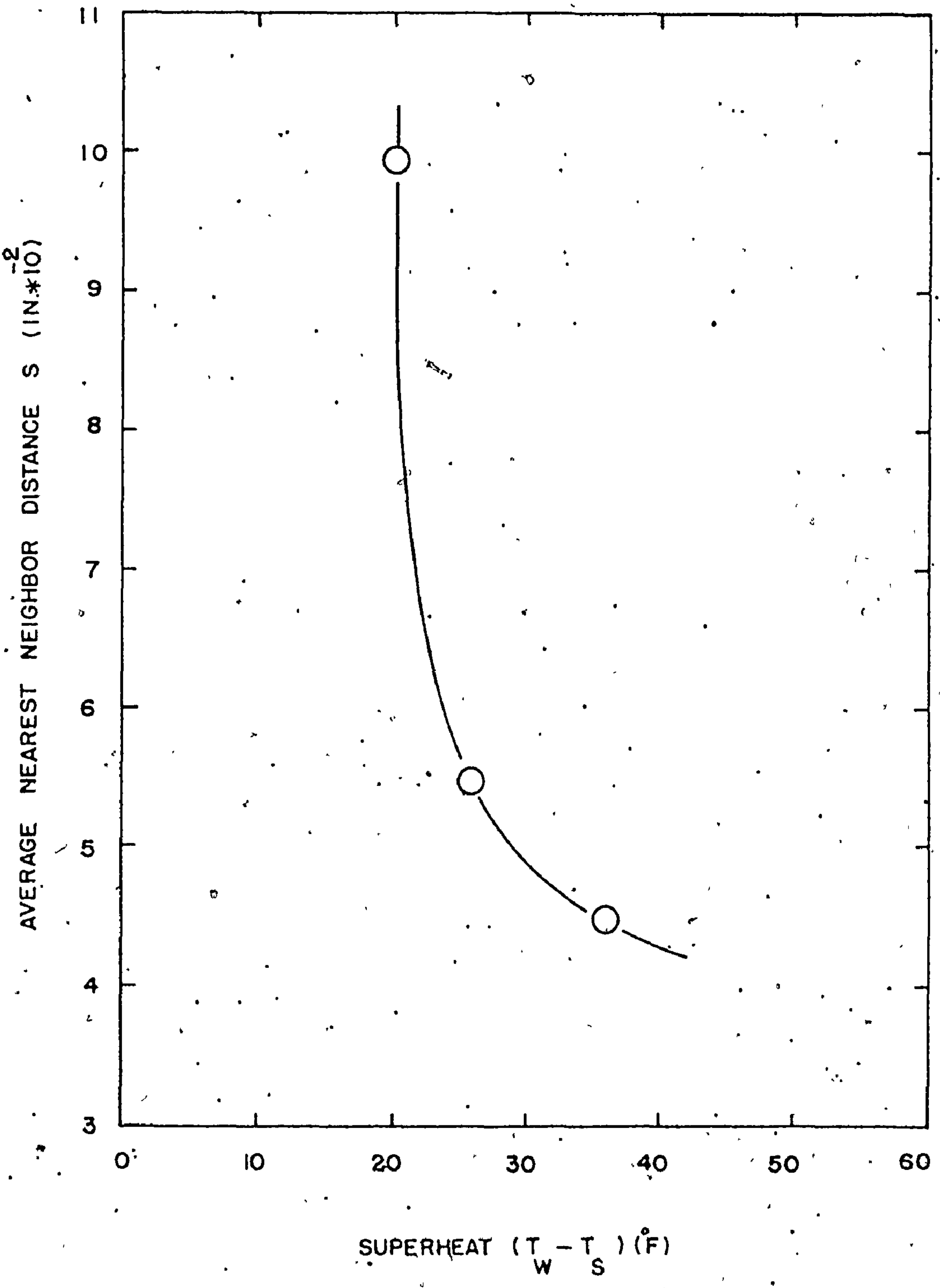

Figure (38) Variation of Average Nearest-Neighbor Distance With Surface Superheat

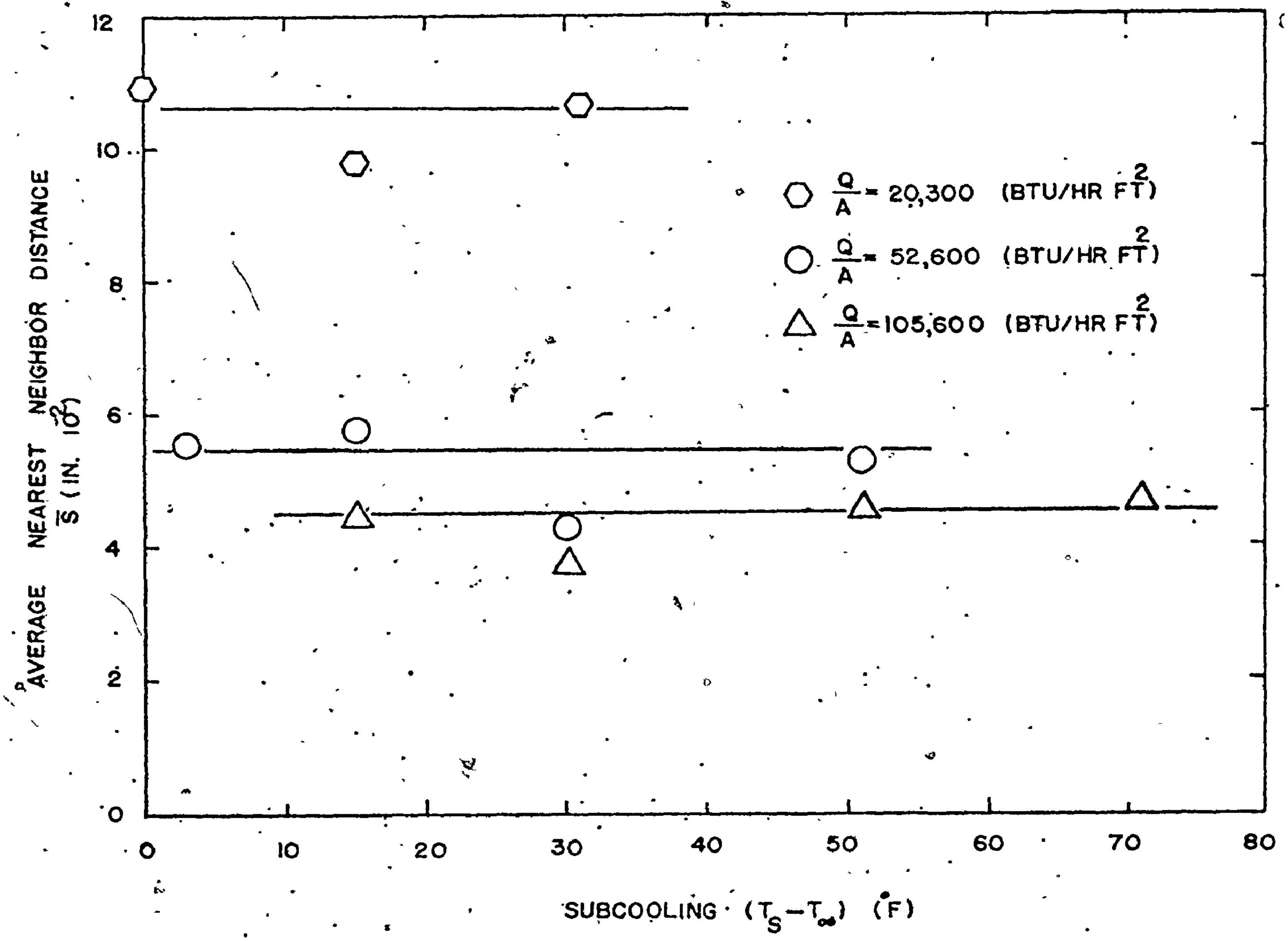

Figure (39) Variation of Average Nearest-Neighbor Distance With Bulk Subcooling

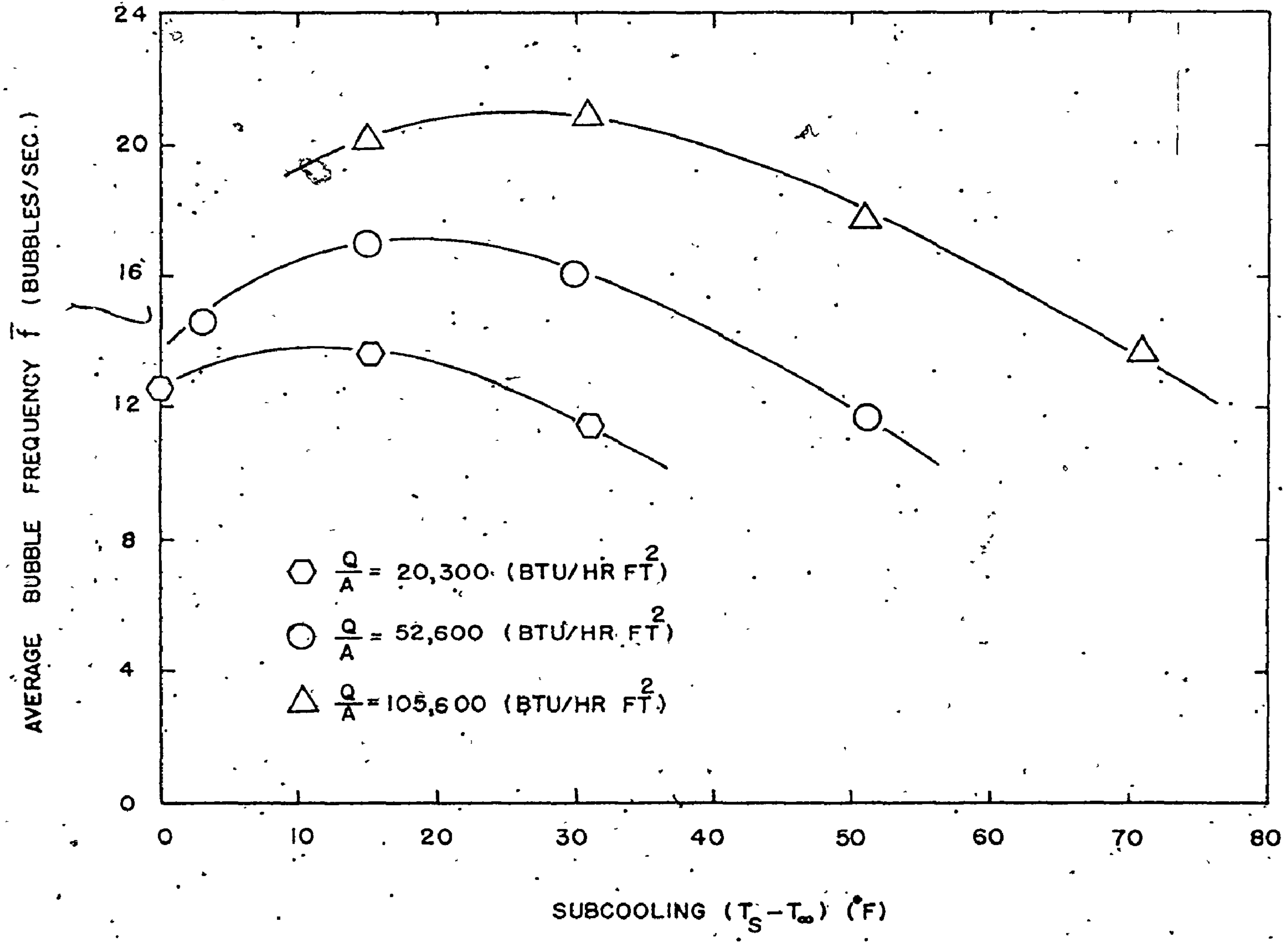

Figure (40) Variation of Average Bubble Frequency With Bulk Subcooling

CHAPTER 8

ANALYSIS AND DISCUSSION

The characteristic boiling curve represents the relationship between the wall superheat (T_W - T_S) and the heat flux Q/A. Previous investigations of the effect of surface condition on the surface superheat indicated clearly that rough surfaces produce smaller values of superheat for the same rate of heat flux that smooth ones. Not only the position of the boiling curve was changed with the change of surface condition but also the slope of the boiling curve was changed. Figure (30) shows the characteristic boiling curve for the present study. In comparison, the experimental data obtained by Wiebe [25] and Gaertner [28] were plotted on the same graph and establish some confidence in the present work.

Subcooling has a slight effect upon the superheat at constant heat flux as illustrated in Figure (31). Increasing subcooling first causes the superheat to increase slightly and then causes the superheat to decrease. The value of subcooling corresponding to the maximum value of superheat increases with increasing heat flux. This type of behaviour is in qualitative agreement with the observations of Judd [22] and Wiebe [25].

The active site density observed in the present investigation for the three different levels of heat flux were plotted on the same graph with the data which had been observed by Gaertner [28] as shown in Figure (41) for the sake of comparison. The present results indicate that the active site density observed increases with the increase of heat flux in the same manner as that observed by Gaertner. The present results, which indicate a greater value of active site density than the Gaertner results for the three different levels of heat flux may be due to a difference in the heating surface microroughness.

As far as the surface roughness is concerned, the number of potentially active sites per unit area increases as the microroughness is increased. The results of numerous investigators have indicated that increasing heat flux can be seen to cause additional nucleation sites to be activated to facilitate the transfer of the additional heat and Figure (41) shows this sort of variation. According to the relationship $Q/A \propto (N/A)^m$, the present value of m was 0.77. In comparison with other investigators, Shoukri and Judd [7] obtained a value of 0.5 for boiling water on copper surface at atmospheric pressure, Westwater and Kirby [29] obtained a value of 0.73 for boiling carbon tetrachloride and methanol on a ground glass surface, Gaertner and Westwater [14] obtained a value of 0.49 for boiling a solution of nickel salts containing 20% solids on copper surface at atmospheric pressure and Kurihara and Myers [4] obtained a value of 0.55 and showed that the exponent m appears to be smaller for rough surfaces than for smooth surfaces. The exponent m takes different values ranging from 0.5 to 1. Presumably this range of exponents is the result of minor variations in surface finish.

The results of the present investigation in Figure (36)

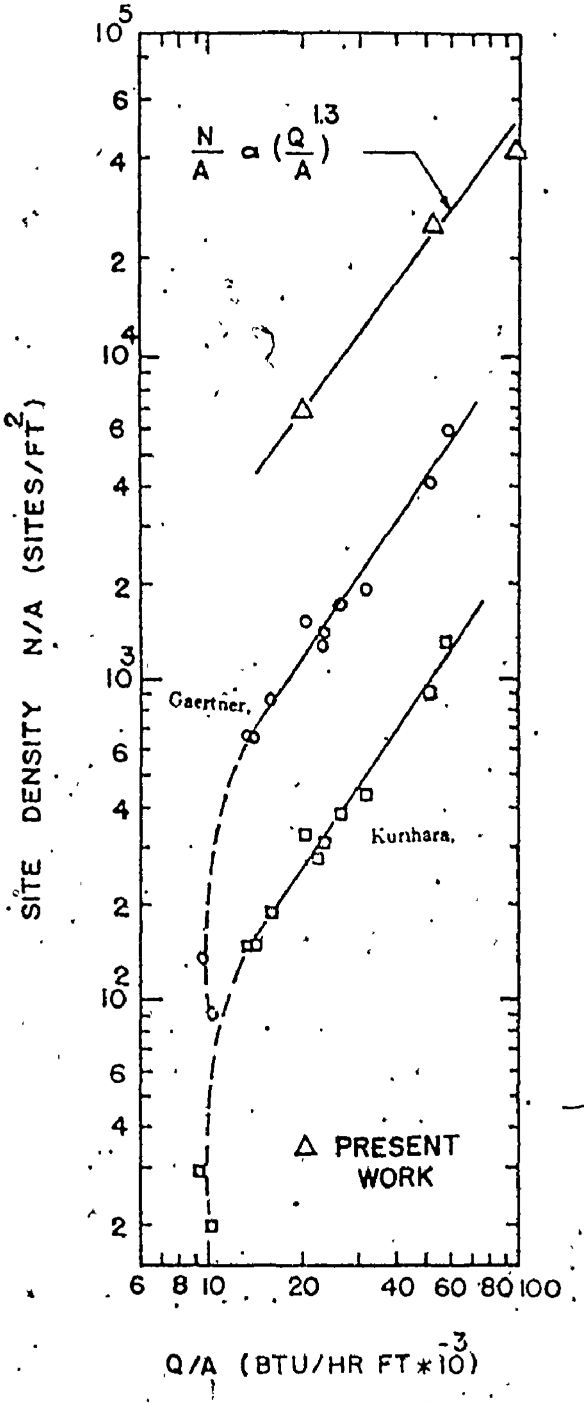

Figure (41) Relationship Between Active Site Population and Heat Flux for Water indicate that subcooling has much less influence on active site density than heat flux. There are no comparable results known for the water-copper combination which would enable the observed variation in the active site density to be corroborated. Some similar work has been done by Judd [22] with the Freon 113 - glass surface combination as shown in Figure (42) which has the same trend as the present investigation.

Any analysis of the boiling heat transfer process occuring on the heating surface should involve the spatial distribution of the local active site population in order to understand the mechanisms of boiling heat transfer. Many natural processes involving spatial distributions are described by the Poisson equation

$$P(X) = \frac{e^{-U}(U)^{X}}{X!} \qquad \text{----20}$$

where

$P(X)$ = Probability of event X occuring

U = Expected value of event X

Few studies exist which treat the distribution of active sites on the heating surface. Gaertner [19] determined that for three different levels of heat flux, the spatial distribution of the local active site population followed the Poisson distribution as shown in Figure (43). The implication of the agreement between the data and the Poisson distribution is that the active sites were distributed randomly on the heating surface. It can be seen from Figure (44), obtained by plotting Gaertner's experimental data on Poisson probability paper, that good agreement with the Poisson distribution exists

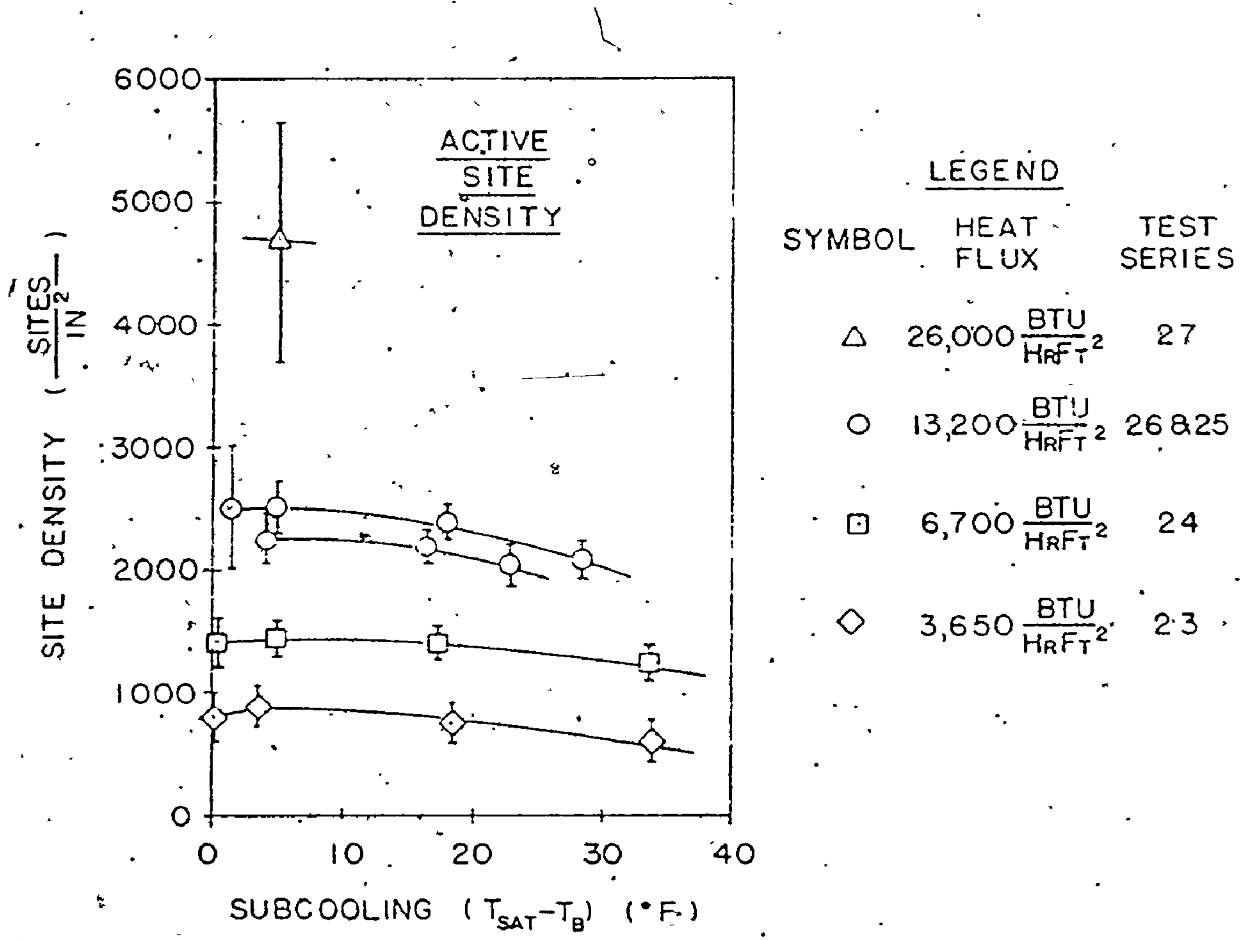

Figure (42) Active Site Density Versus Subcooling According to Judd

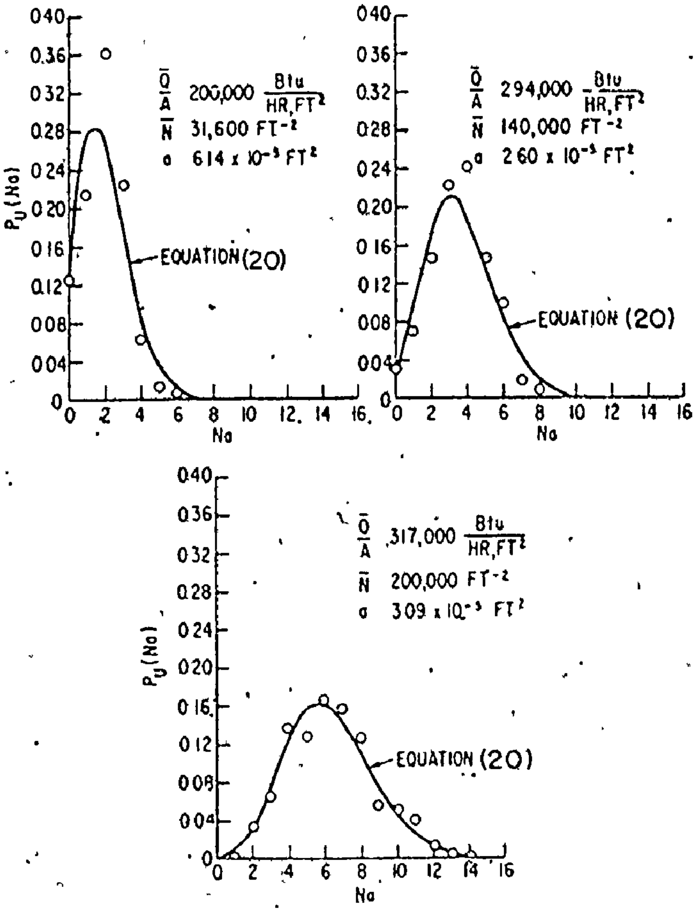

Figure (43) Local Active Site Distribution According to Gaertner 19

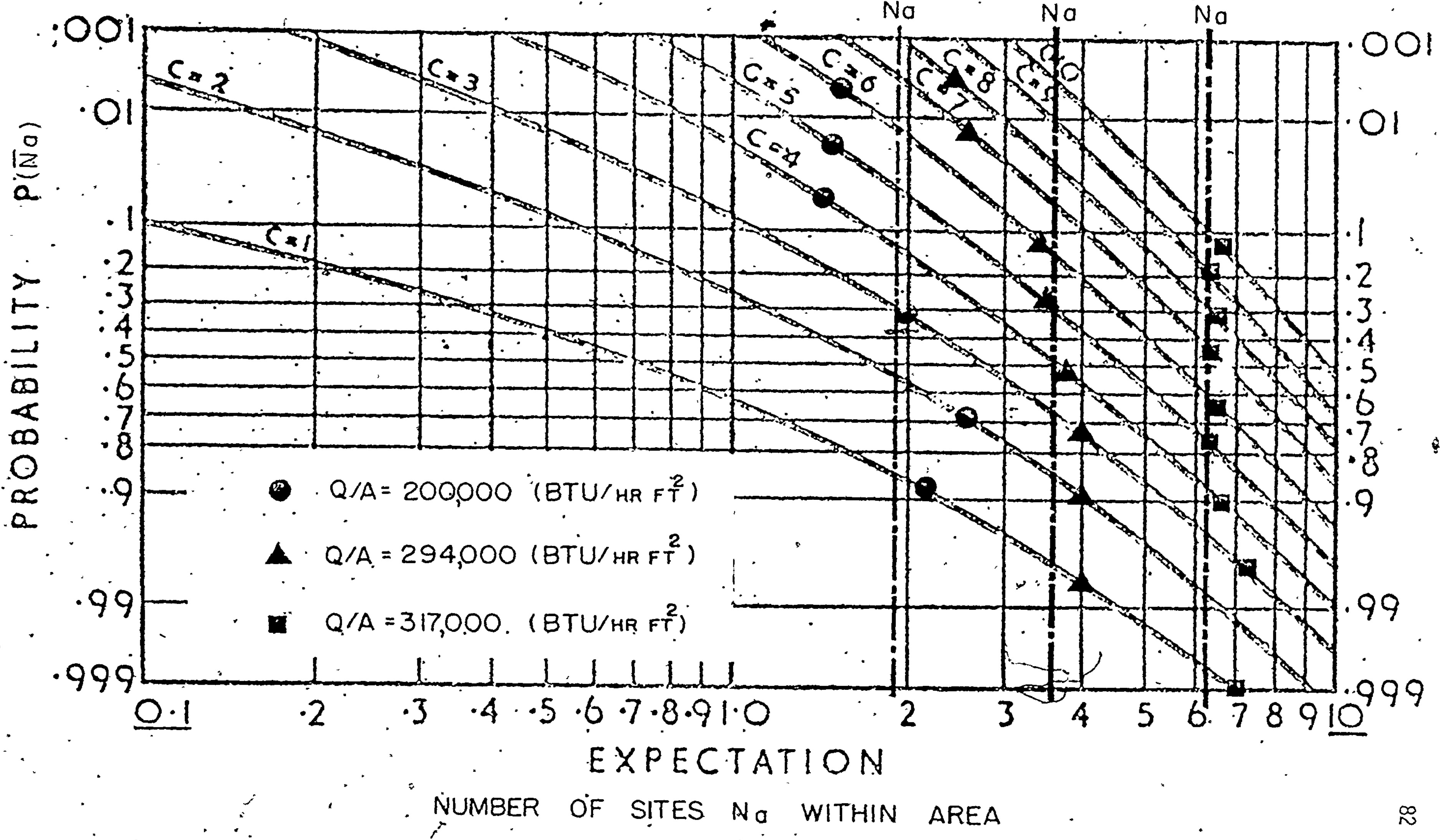

Figure (44) Poisson Plot for Gaertner Results 19 only for the results obtained at $Q/A = 317,000$ BTU/hr. ft.^{2}, since the data lies almost on a vertical line representing $\overline{Na}$, the expected value of the active sites within a local area a. In the case of Q/A equal to 200,000 BTU/hr. ft.^{2} and 294,000 BTU/hr. ft.^{2}, the data shows some scattering about the expected value of $\overline{Na}$. This scattering may be due to the size of the local area selected with respect to the number of active sites found within the area. The fact that this effect disappeared at the highest heat flux level is most likely due to the increase in the number of active sites.

The spatial distribution of the active sites on the heating surface has been studied in the present investigation at three different heat flux levels and various levels of subcooling. The heating surface was divided into a number of small squares and the probability of finding the local population Na was calculated according to

$$P(Na) = \frac{a}{A} Z_{Na} \qquad \text{----21}$$

where

A = Heating surface area (1 x 1) inch square

a = Local surface area

Z_{Na} = Number of small areas having a local population Na.

The probability distributions obtained, showed that agreement with the Poisson distribution was better when the heating surface was divided into twenty-five small areas than when it was divided into one-hundred small areas. The probability of finding the local population Na was calculated from equation (21) considering $a/A = 1/25$.

The probability distributions in Figures (45), (46), and (47) presented a good fit with the Poisson distribution; this conclusion is confirmed by the results of a χ^2 test which is described in Appendix E. The finding of the present investigation are consistent with those of Gaertner's investigation as far as the randomness of the active nucleation site distributions is concerned.

The nearest-neighbor distance between the active sites represents a significant parameter for representing the characteristics of nucleate boiling. At low heat flux the number of the active sites is quite small, and accordingly there is a wide range of nearest-neighbor distances. In the case of high heat flux, the number of the active sites is large and consequently, the range of nearest-neighbor distances becomes quite small. Up to the present time, little experimental data have been available describing the two dimensional spacing of active sites.

Gaertner [19] followed the idea of Clark and Evans in computing the most probable, mean and root mean square nearest-neighbor distance according to the following:

$$S_{mp} = \frac{1}{\sqrt{2\pi}} \left(\frac{N}{A}\right)^{-\frac{1}{2}} \qquad \text{----21}$$

$$\overline{S} = \frac{1}{2} \left(\frac{N}{A}\right)^{-\frac{1}{2}} \qquad \text{----22}$$

$$\sqrt{\overline{S^2}} = \frac{1}{\sqrt{\pi}} \left(\frac{N}{A}\right)^{-\frac{1}{2}} \qquad \text{----23}$$

Figure (48) shows the relationship between the average active

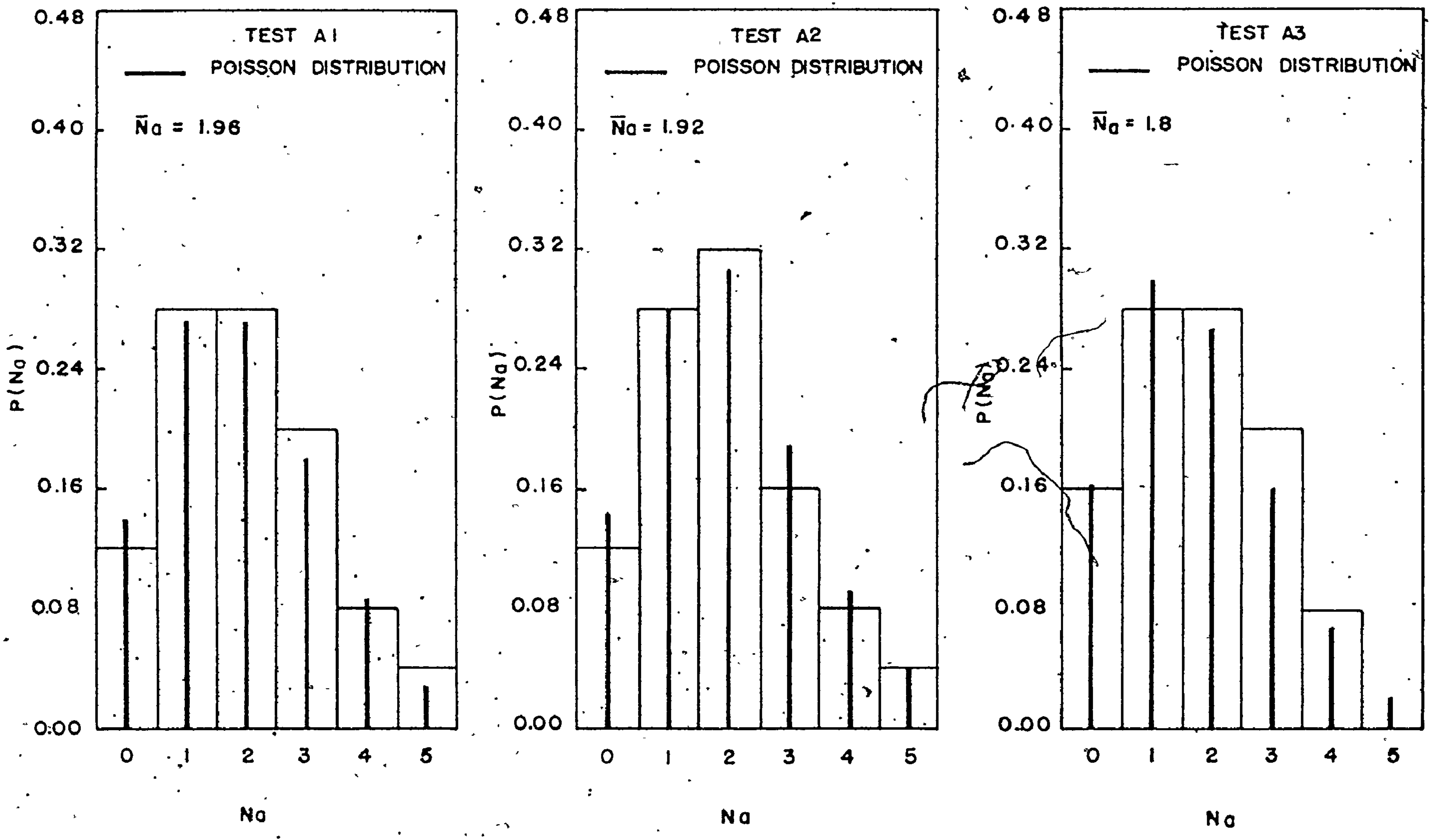

Figure (45) Local Active Site Distribution (Q/A = 20,300 BTU/hr. ft.^{2})

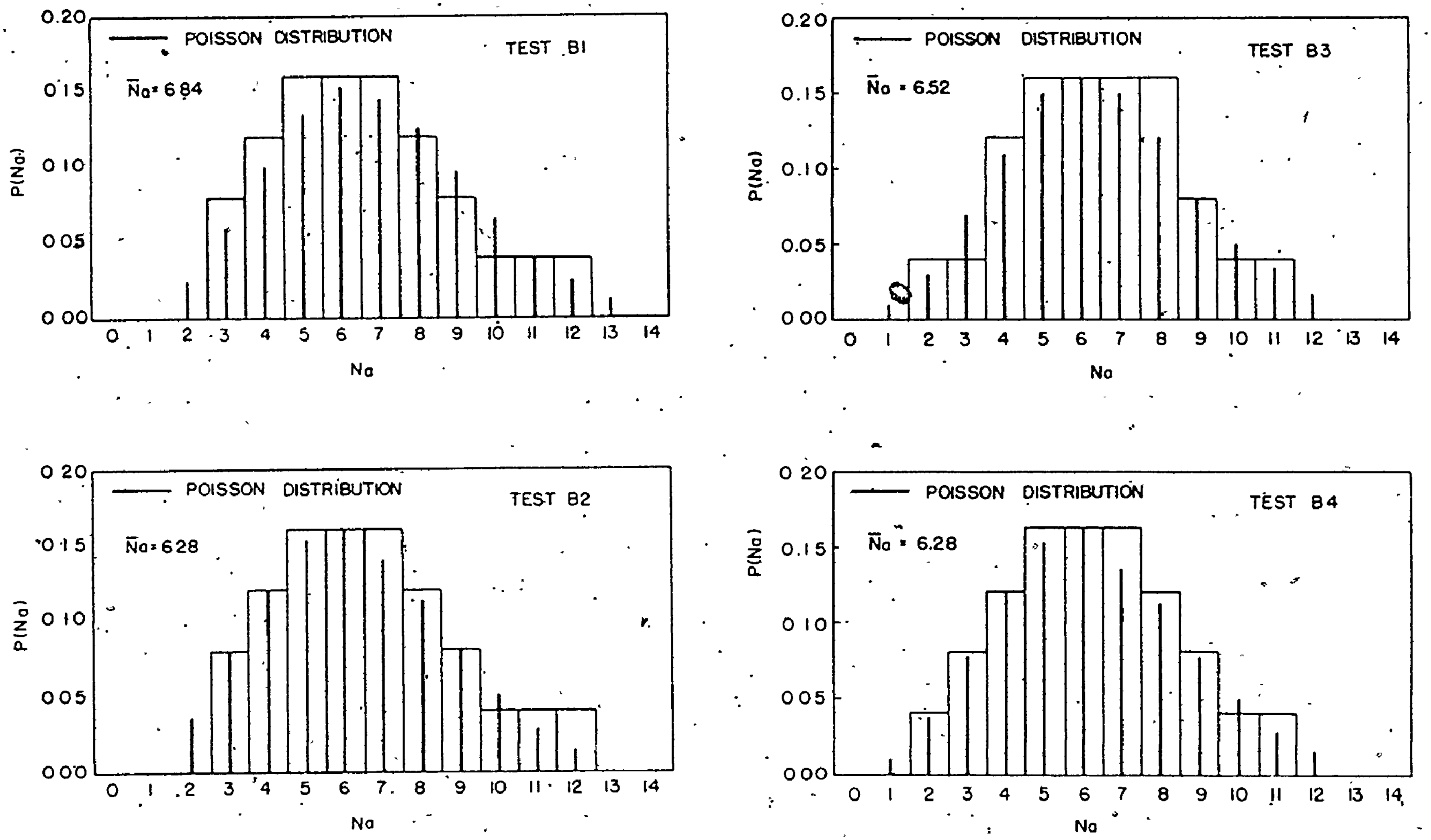

Figure (46) Local Active Site Distribution (Q/A = 52,600 BTU/hr/ft.^{2})

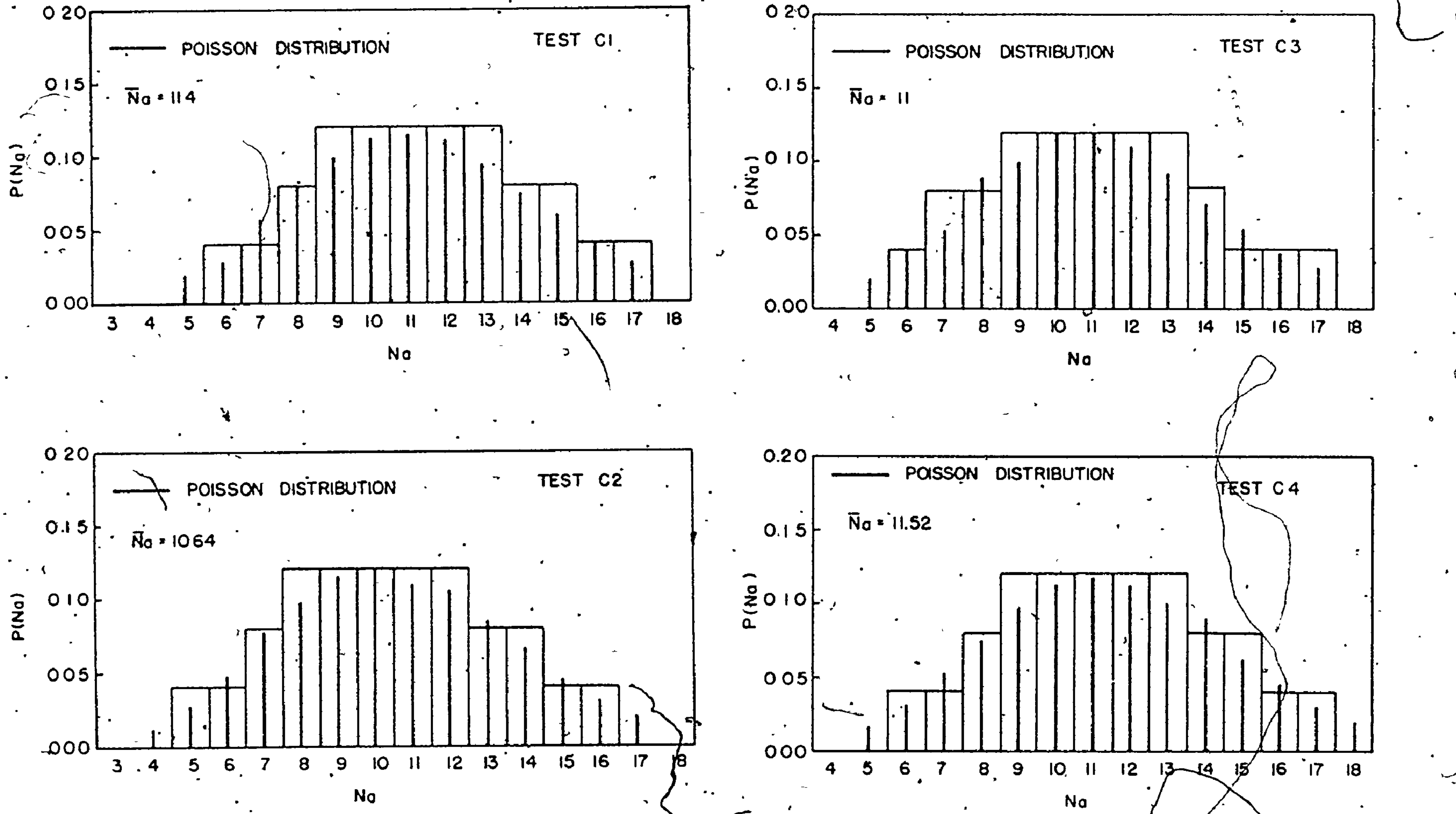

Figure (47) Local Active Site Distribution (Q/A = 105,600 BTU/hr. ft.^{2})

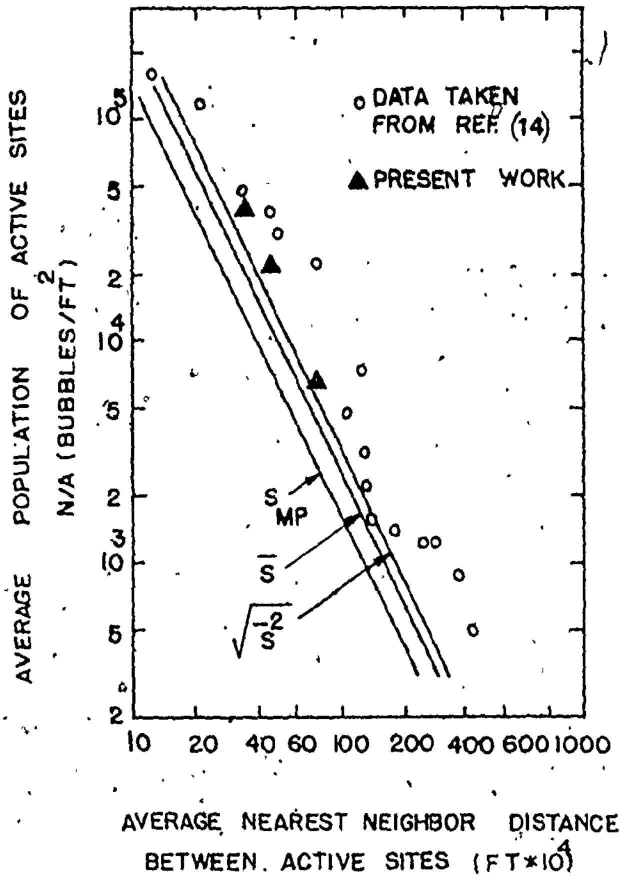

Figure (48) Average Population of Active Sites Versus Average Nearest-Neighbor Distance site density and the average nearest-neighbor distance between active sites. Gaertner [19] presented in the figure three solid lines representing the three equations above for the nearest-neighbor distance. Gaertner indicated that none of these equations was in agreement with the data taken from Gaertner and Westwater [14]. These authors obtained their average nearest-neighbor distance by taking the average of the shortest distances between each active site and each of the surrounding nearest sites, summed up these averages for all of the active sites and divided by the number of active sites as represented in Figure (49). The lack of agreement most likely stems from the fact that the average distance computed by Gaertner and Westwater is not really the average nearest-neighbor distance. The average nearest neighbor distance in the present investigation was calculated on the computer by examining the distances between each active site and all the active sites on the heating surface as represented in Figure (50). The nearest-neighbor distance was selected for each active site. If for example, active site C was examined and active site D were the nearest to C where the distance S between C and D were greater than either co-ordinate X or Y for active site C, active site C was disregarded since it is possible that another site outside of the (1 X 1) inch square might be more closely related. The average nearest-neighbor distance was obtained by summing the nearest-neighbor distances for the active sites considered and then dividing by the number of active sites. Figure (48) shows better agreement between the results of the present investigation and Gaertner [19] predictions for the average

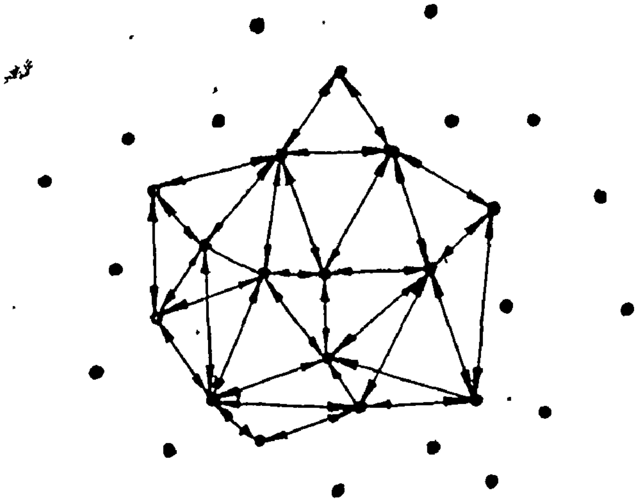

Figure (49) Illustration of Technique Used to Obtain Average Distance by Gaertner and Westwater

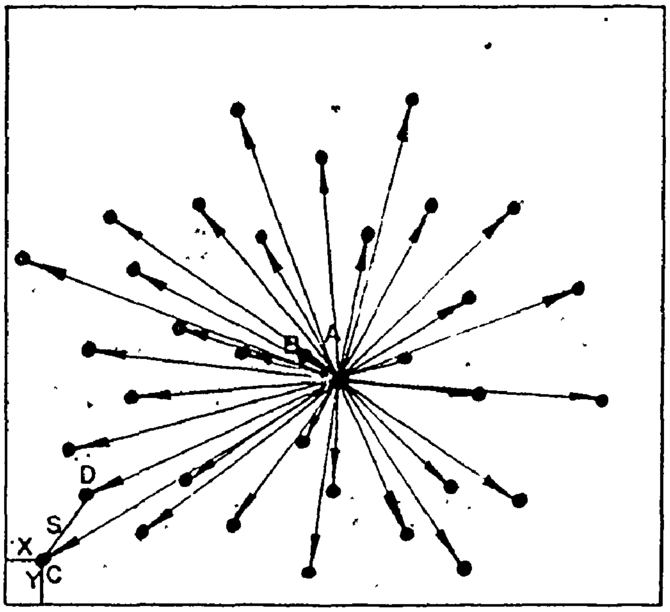

Figure (50) Illustration of Technique Used to Obtain Average Distance in the Present Investigation nearest-neighbor distance.

Figure (51) shows the statistical representation of the distribution of bubble flux density over the heating surface based upon the results presented in Figure (33). As an example of the use of this figure, it can be seen that nineteen small squares contribute a bubble flux density in the range of 0 to 10 bubbles/sec. in.^{2} Figure (52) shows the cumulative distribution of bubble flux density. As an example of the use of this figure, it can be seen that a total of seventy-four small squares contribute a bubble flux density less than 30 bubbles/sec. in.^{2} Figure (53) shows the cumulative bubble flux density versus the cumulative area. In this case, 61 squares contribute a total of 823 bubbles/sec. in.^{2}. Figure (54) shows the percentage cumulative bubble flux density versus the percentage cumulative area.

The bubble flux density distribution on the heating surface has a significant effect on the boiling heat transfer process. The present investigation concerns the distribution of the bubble flux density over one hundred small squares which represent the whole heating area. Figure (55) shows the percentage cumulative bubble flux density versus the percentage cumulative area for the heating surface. It is seen that the effect of subcooling is quite small but the effect of heat flux is significant. As the heat flux is increased, the number of active sites increases and the bubble frequency increases also. Consequently, there is a tendency for the bubble flux density distribution to become uniform at high heat flux, in which case 10

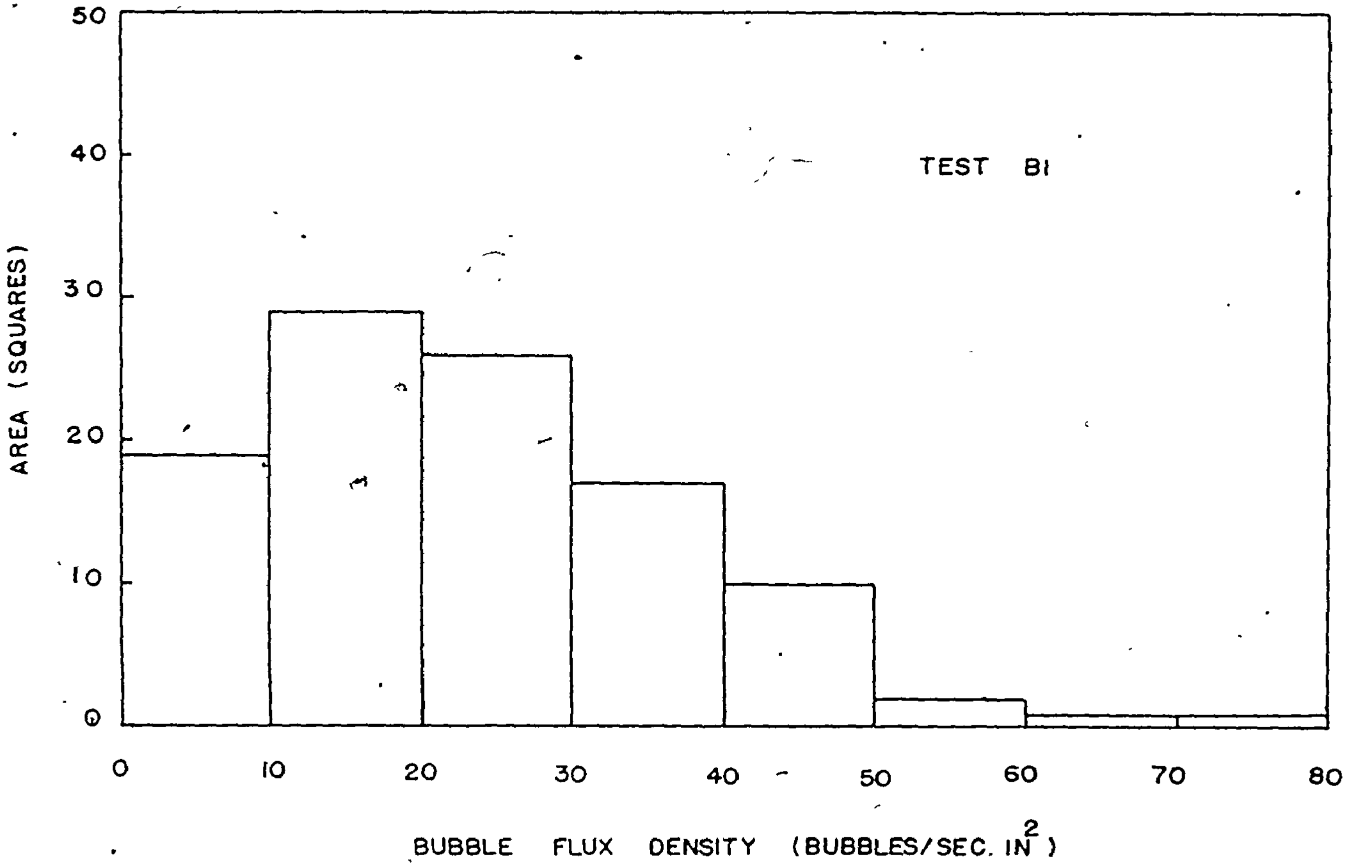

Figure (51) Distribution of Bubble Flux Density

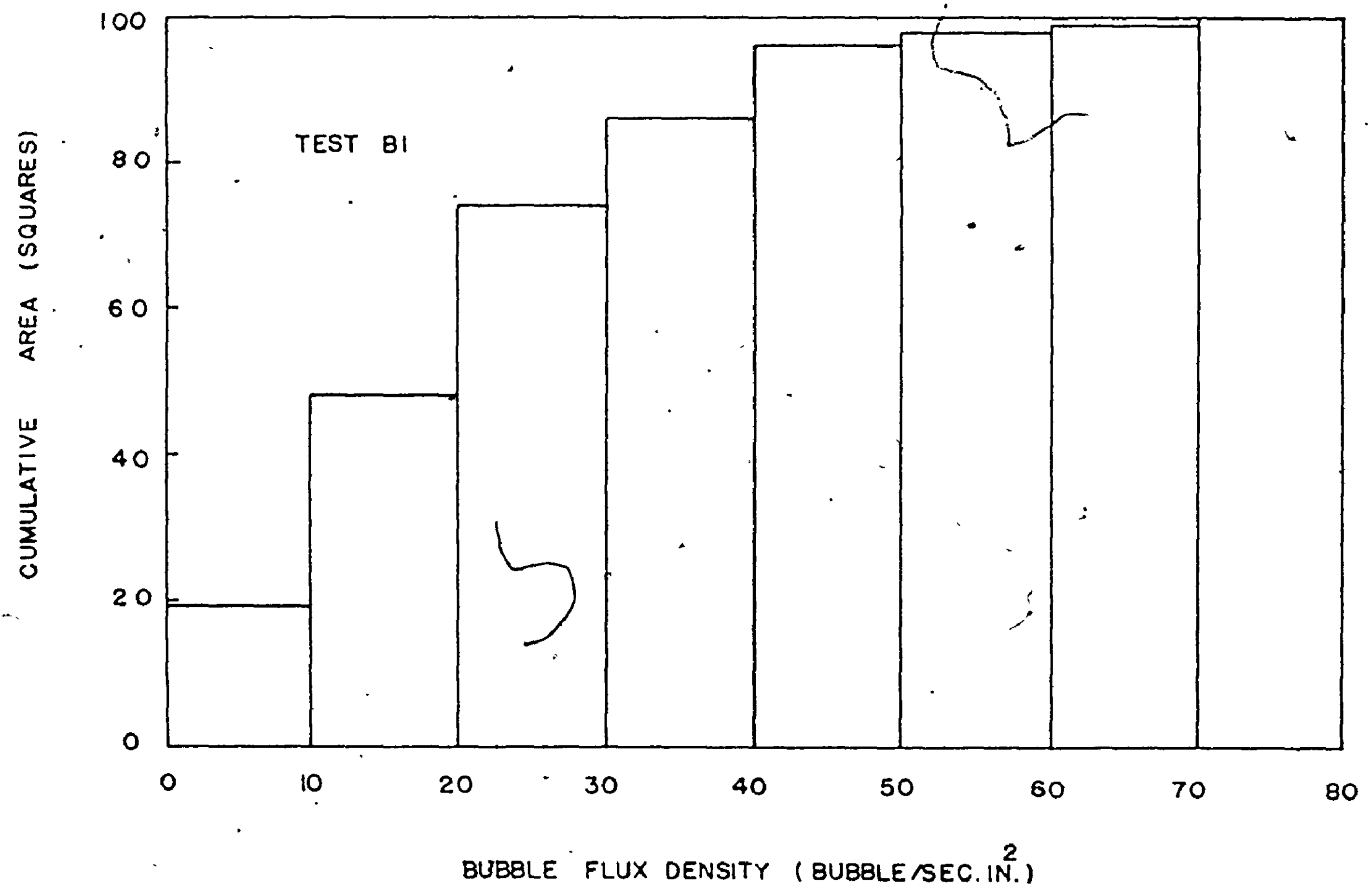

Figure (52) Cumulative Distribution of Bubble Flux Density

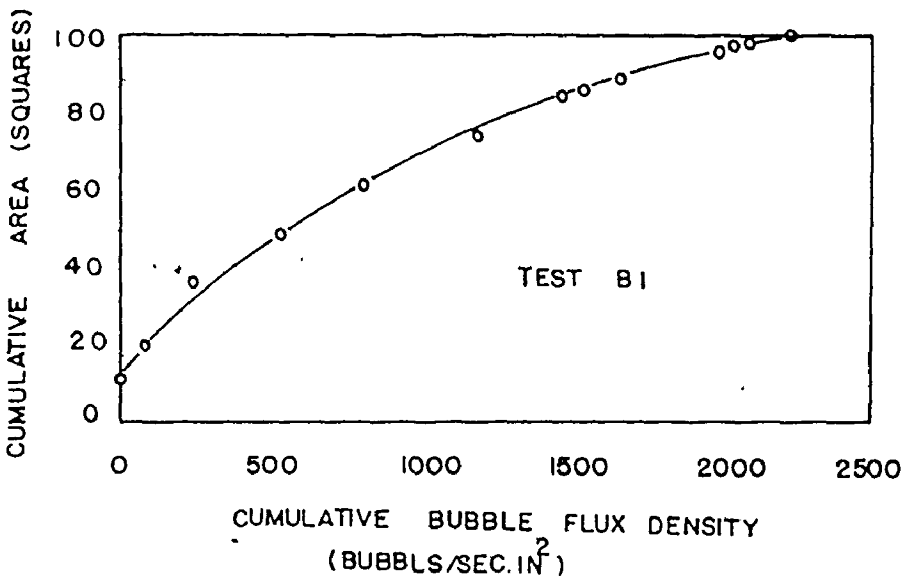

Figure (53) Cumulative Bubble Flux Density Versus Cumulative Area

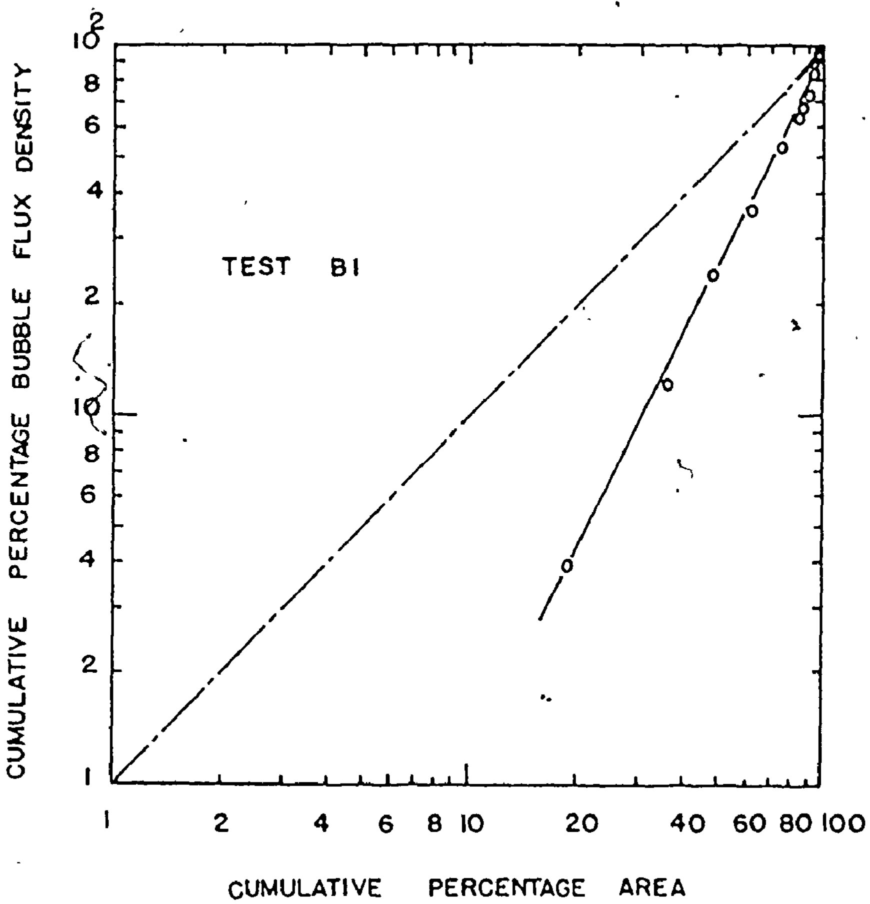

Figure (54) Cumulative Percentage Bubble Flux Density Versus Cumulative Percentage Area

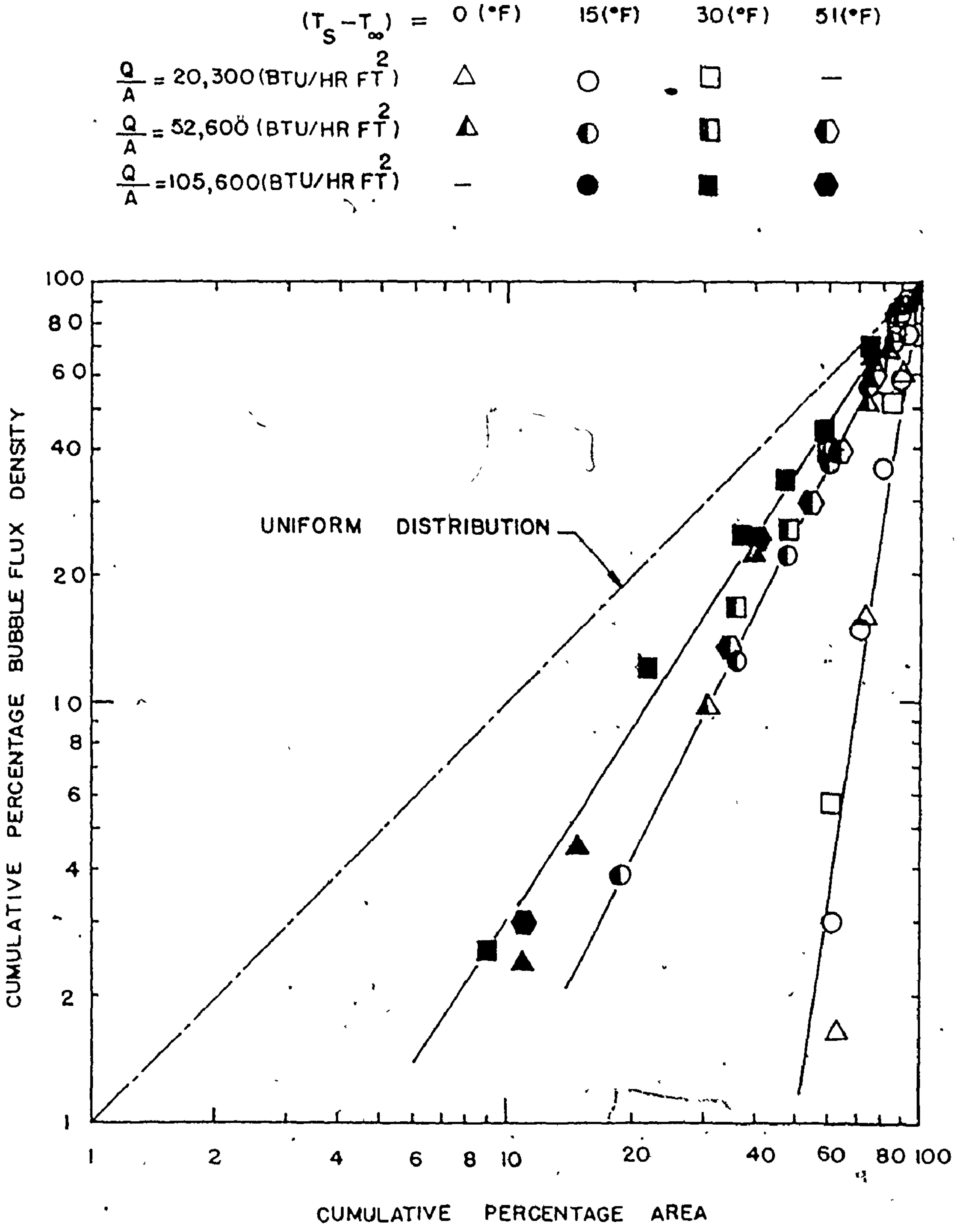

Figure (55) Cumulative Percentage Bubble Flux Density Versus Cumulative Percentage Area of the area would contribute 10% of the bubble flux density, for instance.

The influence of heat flux and subcooling on the pattern of the active nucleation sites was studied in the present investigation. An area of (0.2 X 0.2) inch square was selected from the area tested to examine the change in pattern of the active nucleation sites with changing heat flux and subcooling during a single experimental run. Figure (56) shows the influence of three different levels of heat flux on the active nucleation site pattern at constant subcooling. As heat flux increased, bubbles continued to originate from the nucleation sites already activated and some more nucleation sites appeared due to the increase of heat flux. Figure (57) shows the influence of three different levels of subcooling on the active nucleation site pattern at constant heat flux. As the subcooling increased, the active nucleation site pattern did not change, except for one active nucleation site which appeared, perhaps as the result of the slight increase of superheat with the increase of subcooling.

These results show that bubbles originate from specific locations on the heating surface such as a cavity or scratch and present a good agreement with Corty and Foust [2] and others who advanced the postulate the bubbles originate on a heating surface from nucleation sites in which a gas or vapour phase prexists.

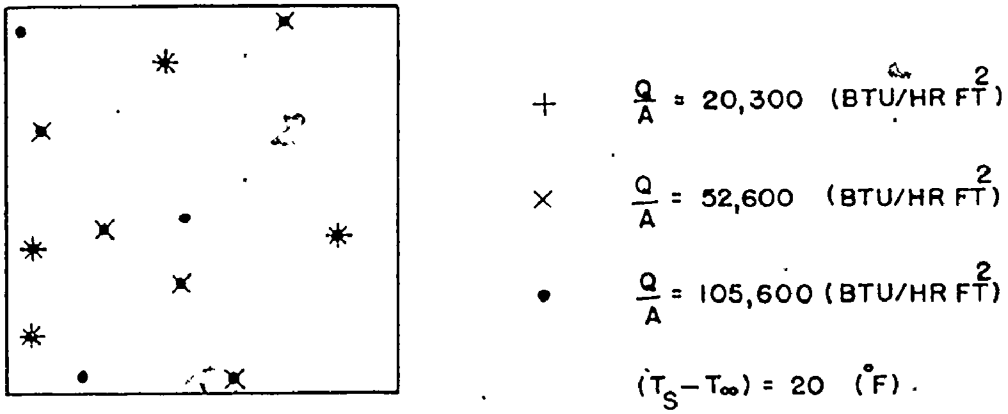

Figure (56) Influence of Heat Flux on the Active Site Pattern

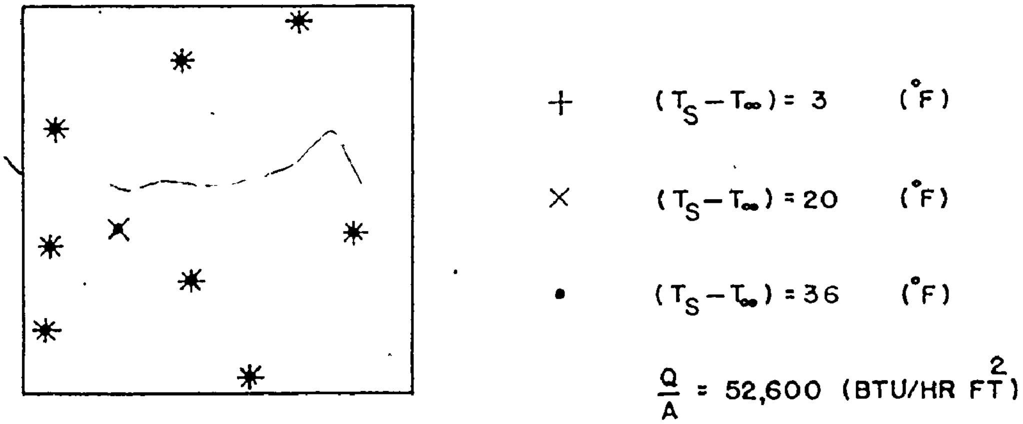

Figure (57) Influence of Subcooling on the Active Site Pattern

CHAPTER 9

CONCLUSIONS

1. Inagreement with Gaertner's findings, active sites are randomly located and their spatial distribution follows the Poisson distribution.

2. Bubble flux density is observed to be non-uniformly distributed even though it is thought that the heat flux is uniform over the heating surface and one might expect the bubble flux to be uniformly distributed.

3. Changes in heat flux and subcooling do not affect the distribution of active sites. Although increasing heat flux causes more active sites to be activated, the additional active sites form among the sites which have been already activated. Subcooling appears to have no effect at all.

APPENDIX A

ESTIMATE OF HEAT TRANSFER RATE

In the present investigation, two methods were used to calculate the rate of heat transfer through the boiling surface. The first method considered the rate of heat transfer in the neck of the heater block to be determined by one-dimensional heat conductions using the Fourier one-dimensional heat conduction equation. The heat transfer in the redial direction was minimized by using vermiculate as an insulation material, so that it was reasonable to assume

$$\frac{Q}{A} = -k\,\frac{dT}{dx} \qquad \text{----(A.1)}$$

where $k = 145$ BTU/hr. ft. ^{o}F according to Wiebe [25] and $\frac{dT}{dx}$ is the axial temperature gradient measured in the neck of the heater block.

The second method considered the actual rate of heat transfer as the total rate of heat generation less the rate of heat loss, using the same procedure as Wiebe [25] to calculate the rate of heat loss from the system.

A.1 Skirt Heat Loss

$$Q_{Fin} = n_f\,\bar{h}_c\,A_{Fin}\,(T_{Fin\ Base} - T_\infty) \qquad \text{----(A.2)}$$

where

$$n_f = f(2\bar{h}_c L/kt) = f(mL) \qquad \text{----(A.3)}$$

The functional relationship between n_f and mL is given in Schenck [30]

$k = 9.2$ BTU/hr. ft. ^oF

$\bar{h}_c = 130$ BTU/hr. ft.^{2} ^oF

$t = 0.5$ inch

$d_o = 7.75$ inch

$d_i = 2$ inch

$L = 2.88$ inch

$mL = 6.25$ (calculated)

Then $n_f = 0.085$, so that

$$Q_{Fin} = 3.36\ (T_{Fin\ Base} - T_\infty) \qquad \text{----(A.4)}$$

A.2 Radial Heat Loss Through Vermiculite

The volume occupied by the vermiculite can be considered to be comprised of two hollow cylinders for the analysis of heat transfer in the radial direction. Figure (58) shows the locations of the thermocouples used in this analysis.

A.2.1 Around the Neck of the Heater Block

$$Q_{v_1} = \frac{2\pi\ k\ L}{\ln(\frac{r_2}{r_1})} (T_F - T_K) \qquad \text{----(A.5)}$$

$k = 0.48$ BTU/hr. ft.^oF

$L = 1$ inch

$r_1 = 1$ inch

$r_2 = 4$ inch

Therefore

$$Q_{v_1} = 0.18\ (T_F - T_K) \qquad \text{----(A.6)}$$

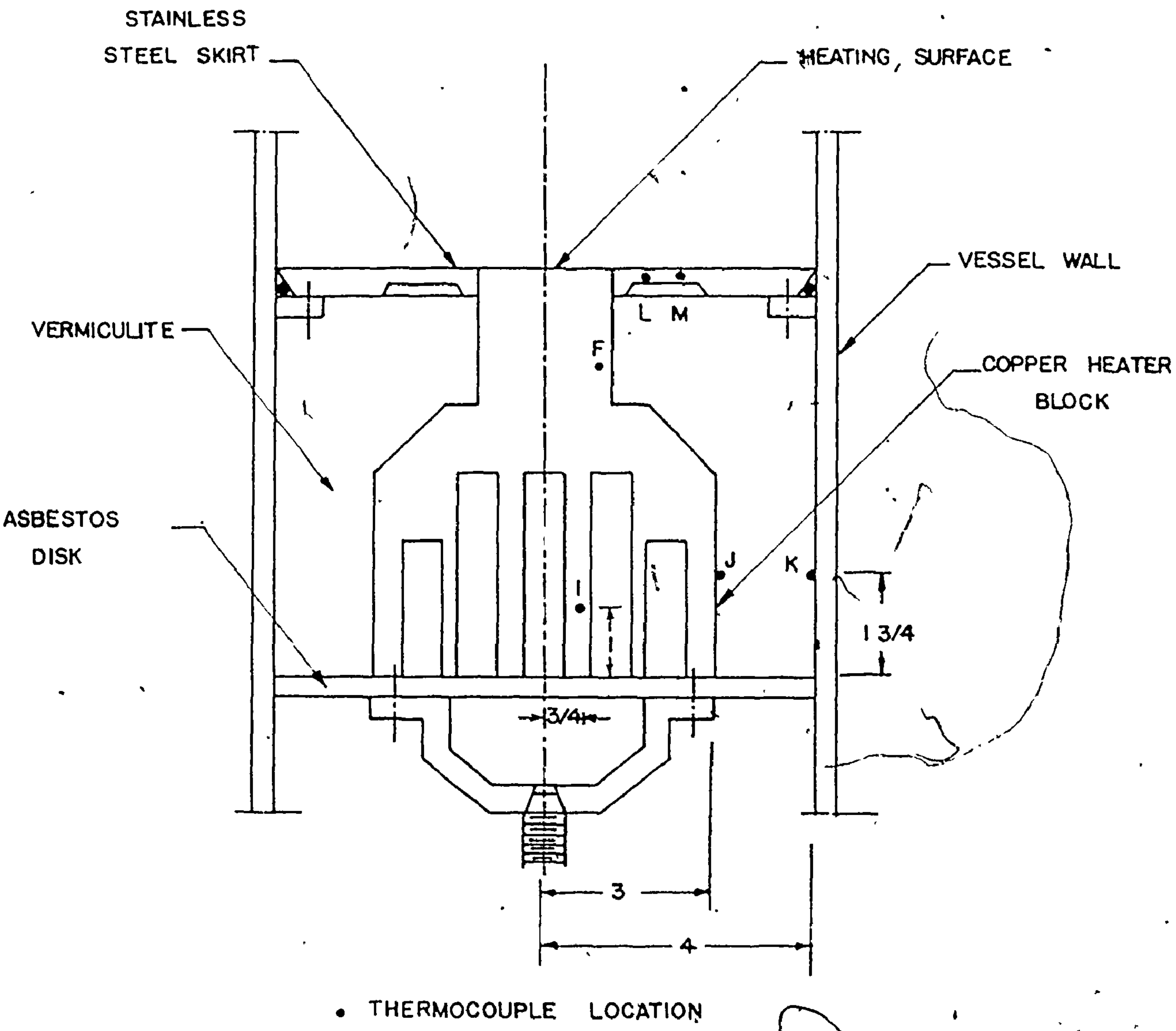

Figure (58) Location of Thermocouples Used in Determining Heat Loss

A.2.2 Around the Base of the Heater Block

$$Q_{v_2} = \frac{2\pi\ k\ L}{\ell n(\frac{r_2}{r_1})}\ (T_J - T_K) \qquad \text{----(A.7)}$$

$r_1 = 3$ inch

$r_2 = 4$ inch

$L = 3$ inch

Therefore

$$Q_{v_2} = 2.62\ (T_J - T_K) \qquad \text{----(A.8)}$$

A.3 Heat Loss From the Bottom Face of the Heater Block

The heat loss from the bottom face was reduced by using an asbestos disk of 1/4 inch thickness so that the heat loss becomes

$$Q_b = \frac{(T_I - T_a)}{\frac{L}{kA_b} + \frac{1}{\bar{h}_c A_b}} \qquad \text{----(A.9)}$$

where T_a is the surrounding air temperature

$L = 0.25$ inch

$A_b = 0.34$ ft.^{2}

$k = 0.09$ BTU/hr. ft.^{0}F

$$\bar{h}_c = 0.12\left(\frac{T_{I'} - T_a}{d}\right)^{1/4} \qquad \text{Schenck [30]} \qquad \text{----(A.10)}$$

where $T_{I'}$ is the temperature of the surface of the asbestos disk

$d = 0.66$ ft.

and therefore

$$Q_b = \frac{(T_I - T_a)}{0.6 + \frac{22}{(T_{I'} - T_a)^{1/4}}} \qquad \text{----(A.11)}$$

$T_{I'}$ is obtained by trial and error estimate as the heat transfer by conduction through the asbestos disk must equal to the heat transfer by convection from the bottom face of the asbestos disk.

A.4 Numerical Calculation

$$Q_{Total} = 1434 \text{ BTU/hr.}$$

TABLE 3 SET OF TEMPERATURE READING

THERMOCOUPLE	TEMPERATURE °F
A	258.0
B	271.1
C	282.2
D	270.4
E	270.3
F	270.2
G	209.4
H	209.8
I	313.0
J	240.9
K	191.5
L	214.1
M	213.1

A.4.1 The First Method:

Equation (A.1) gives

$$Q/A = -145 \times (-31) \times 12$$

$$= 53{,}940 \quad \text{BTU/hr. ft.}^2$$

A.4.2 The Second Method:

$$T_{Fin\ Base} = 240.7^0F$$

Equation (A.4) gives

$$Q_{Fin\ Base} = 3.36\,(240.7 - 209.4)$$

$$Q_{Fin\ Base} = 105.2 \quad \text{BTU/hr.}$$

Equation (A.6) gives

$$Q_{v_1} = 0.18\ (270.2 - 191.5)$$

$$Q_{v_1} = 14.2 \text{ BTU/hr.}$$

Equation (A.7) gives

$$Q_{v_2} = 2.62\ (240.9 - 191.5)$$

$$= 129.4 \text{ BTU/hr.}$$

Equation (A.10) gives

$$Q_b = \frac{(313 - 81)}{0.6 + \frac{22}{(288.3 - 81)^{1/4}}}$$

$$Q_b = 36.3 \text{ BTU/hr.}$$

$$Q_{Loss} = Q_{Fin} + Q_{v_1} + Q_{v_2} + Q_b$$

$$Q_{Loss} = 105.2 + 14.2 + 129.4 + 36.3$$

$$Q_{Loss} = 285.1 \text{ BTU/hr.}$$

$$Q_{Actual} = 1434 - 285.1 = 1148.9 \text{ BTU/hr.}$$

$$\left(\frac{Q}{A}\right)_{Actual} = 52{,}660 \text{ BTU/hr. ft.}^2$$

In comparison

$$\left(\frac{Q}{A}\right) = 53{,}940 \text{ BTU/hr. ft.}^2$$

and % difference = 2.37%

The difference in the rates of heat transfer between the two methods may be due to the assumption of one dimensional flow in the first method. The second method values were used to represent the value of the rate of heat transfer in the present investigation.

Figure (59) shows the relationship between the actual heat flux calculated and the axial temperature gradient in the neck of the heater block. The relationship for the straight line through the data gives k = 139 BTU/hr. ft. °F which is in excellent agreement with the value suggested by Wiebe.

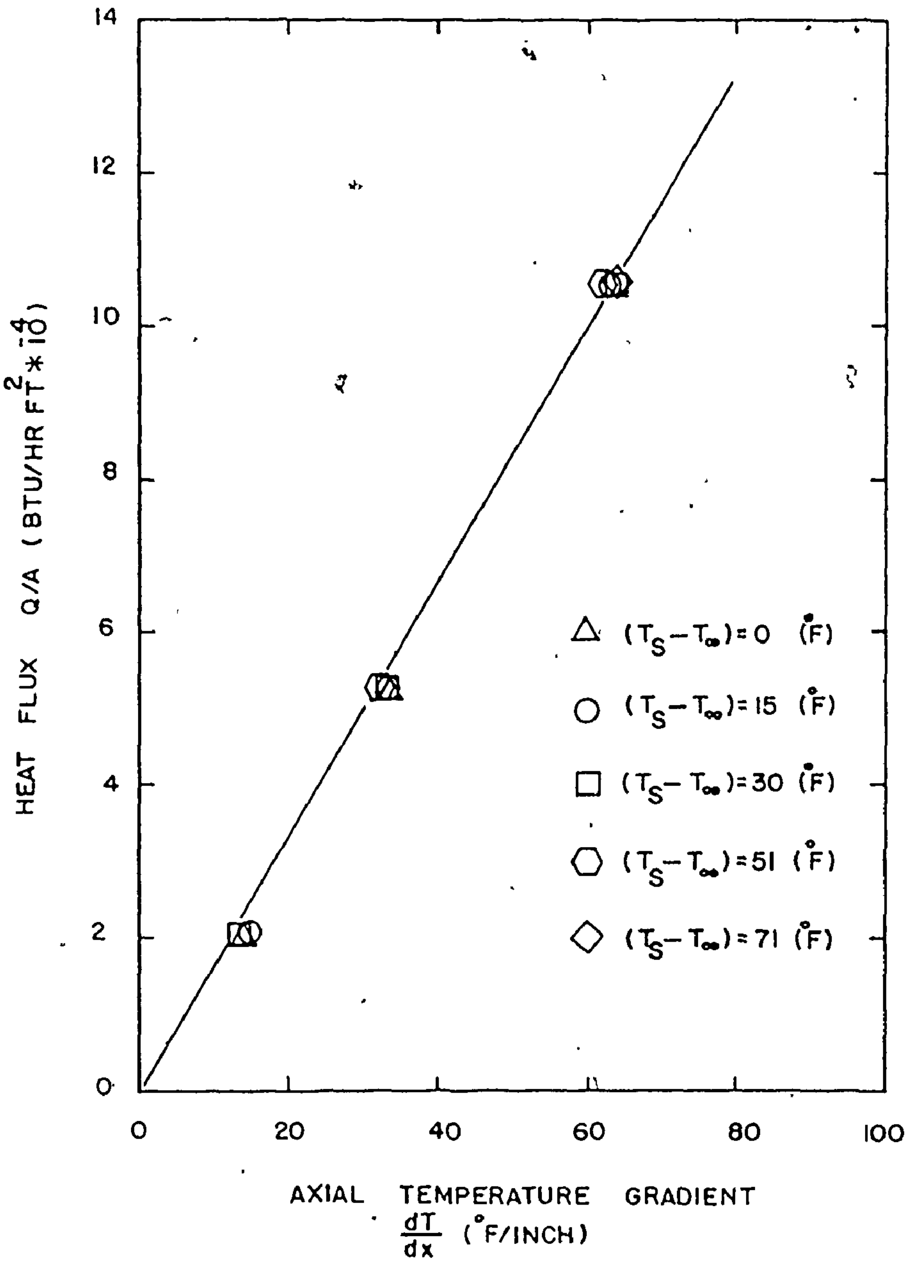

Figure (59) Heat Flux Versus Axial Temperature Gradient

APPENDIX B

BULK LIQUID TEMPERATURE

In the present investigation it was essential to obtain the value of the bulk liquid temperature in both saturated and subcooled conditions. This value was required for obtaining the subcooling level in each test. The bulk liquid temperature could be determined by considering the temperature variation over the heating surface at different levels. After a certain distance from the surface, the liquid temperature remain constant in both of the saturated and subcooled conditions. A preliminary experimental study had been conducted to obtain the liquid temperature distribution above the heating surface using the thermocouple probe shown in Figure (60) positioned in the water at different levels.

Figure (61) shows three temperature profiles for the saturated condition obtained at three different radii. Additionally, Figure (62) shows three temperature profiles obtained under conditions of high heat flux level and highly subcooled boiling liquid. At a displacement of approximately 2 inches from the heating surface, the three temperature profiles approach a common value 212°F for the saturated conditions, whereas for the subcooled conditions, the three curves approach a common value of 115°F. Consequently, it was felt that the temperature measured at a displacement of 2 inches from the surface would adequately characterize the bulk temperature. During

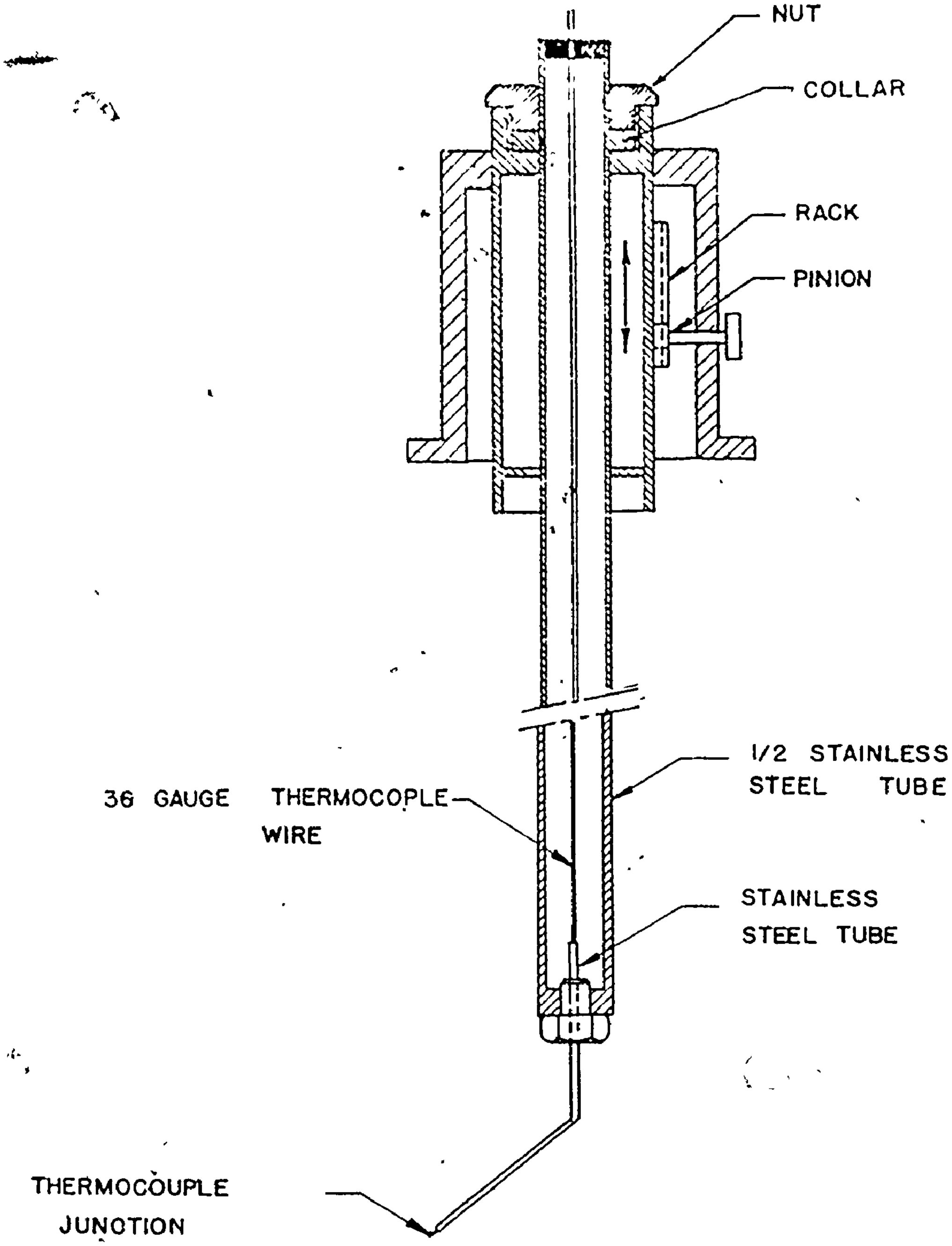

Figure (60) Thermocouple Probe

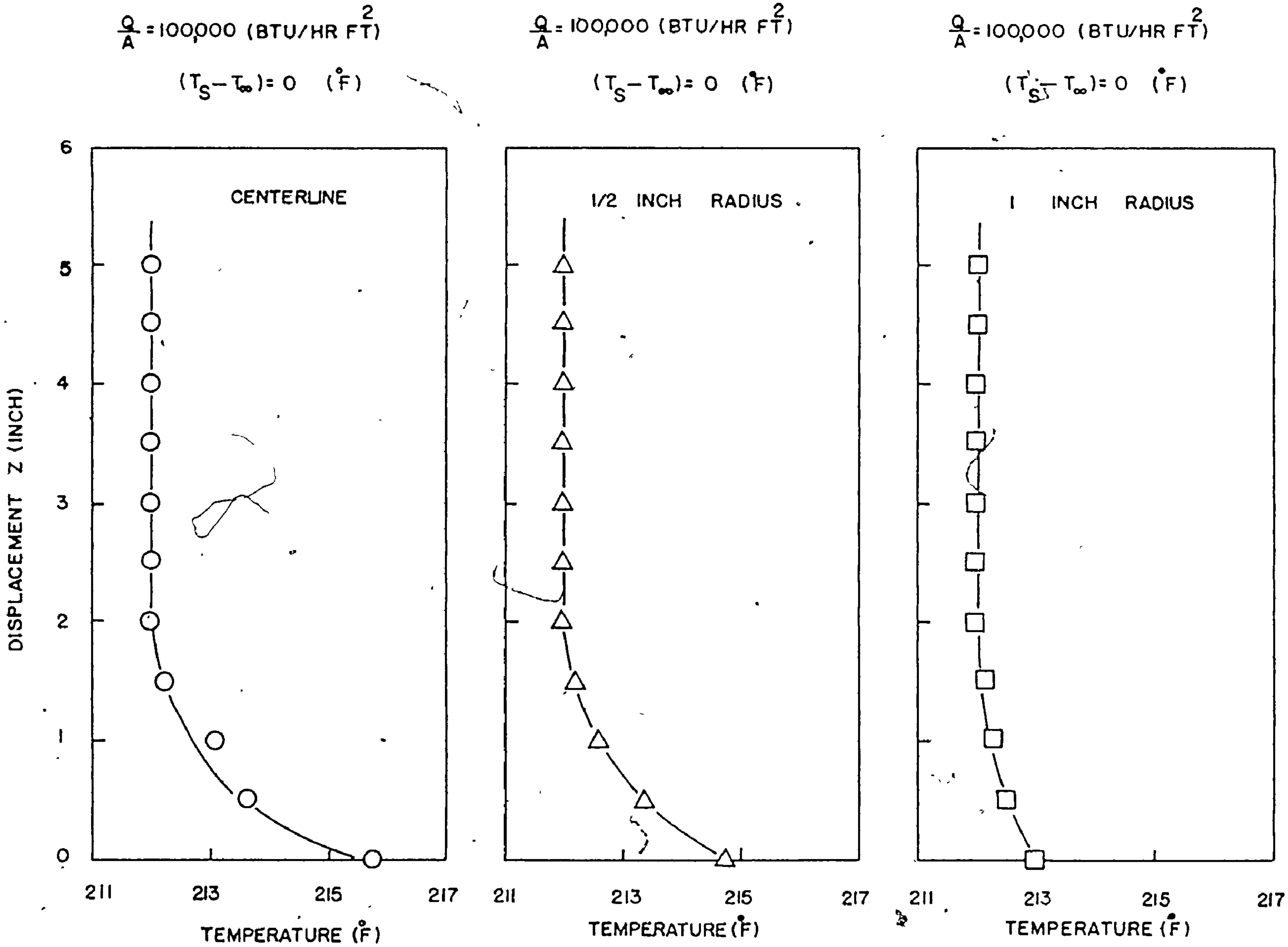

Figure (61) Bulk Liquid Temperature Profiles for Saturated Conditions

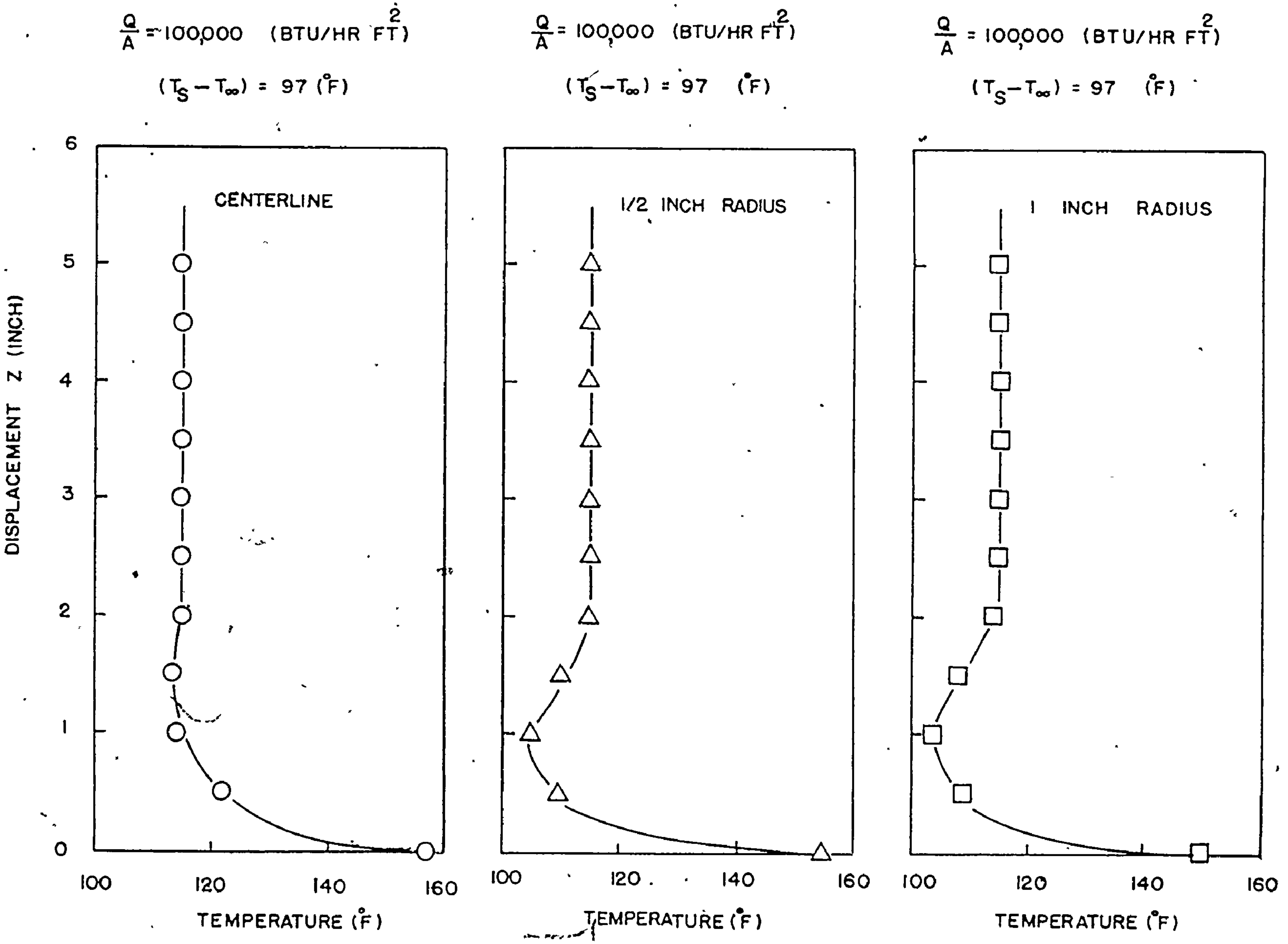

Figure (62) Bulk Liquid Temperature Profiles for Subcooled Conditions the actual test, thermocouples were located at 2 inches and 4 inches from the surface at 1 inch radial displacement. The two measurements taken were averaged so that the error resulting from using one thermocouple might be reduced.

APPENDIX C

BUBBLE DETECTION PROBE

The single most important component of the apparatus was the bubble detection probe. Alternating current with a frequency of 11,000 Hz at 10 volts passed through the varnished copper wire of the probe which was bared at the tip to the water or vapour in the gap between the heating surface and the bubble detection probe. It was important to use a very small diameter varnished copper wire and to place the wire tip as near as possible to the heating surface in order to obtain the distribution of the active sites on the heating surface.

Figure (63) shows the details of the bubble detection probe. It consisted of a probe tip made from copper with a conical shape having a drilled hole with a diameter of 0.032 inches. A stainless steel tube closely matching the hole diameter was soldered at the tip of the copper cone in order to support the varnished copper wire in such a way as to disturb the flow pattern of the bubbles emitted as little as possible. A varnished copper wire having a diameter of 0.007 inches was used at high heat flux and 0.010 inches was used at low and intermediate heat flux. A plastic screw was used to fix the copper wire in the probe tip. The traversing mechanism which was used for controlling the vertical distance between the copper wire tip and the heating surface is depicted in the sketch.

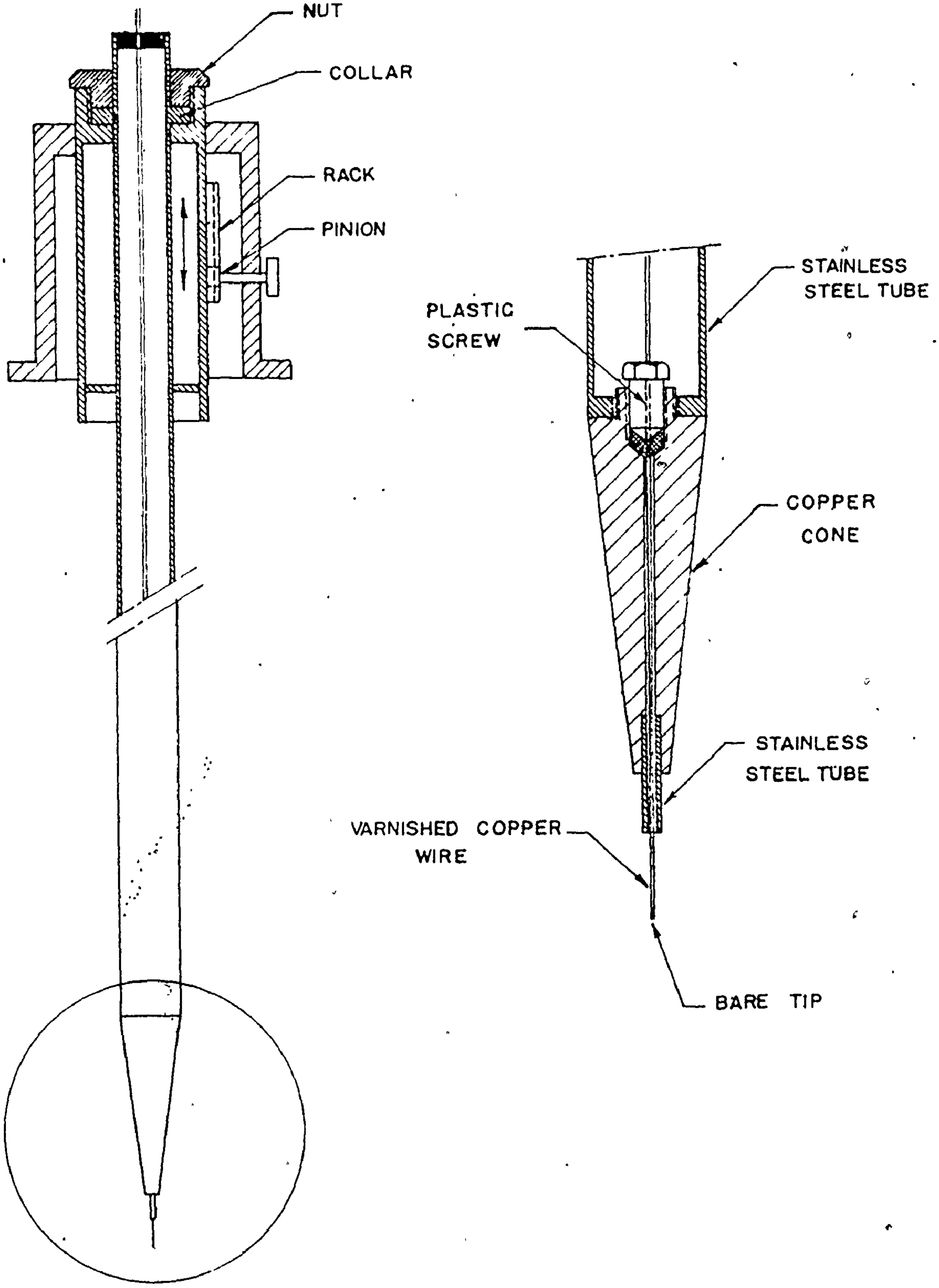

Figure (63) Bubble Detection Probe

APPENDIX D

TABLE (4) TABULATION OF COMPUTED RESULTS

Test No.	$(O/A)_{Actual}$ $(BTU/hr\ ft^2)$	(T_w-T_s) (^oF)	(T_s-T_∞) (^oF)	S_{min} $(inches*10^2)$	$\overline{S}$ $(inches*10^2)$	N/A Bubble/in^2	$\overline{f}$ Bubble/sec	$(\overline{f}\ \frac{N}{A})$ Bubble/sec ft^2
A 1	20,300	20	0	5.94	9.94	49	12.6	612.5
2	20,300	21	15	4.1	9.92	48	13.7	657.6
3	20,300	19	31	6.35	10.61	45	11.5	517.5
B 1	52,600	28	3	2.4	5.54	171	14.6	249.6
2	52,600	30	15	3.6	5.62	157	18.2	285.7
3	52,600	31	30	2.5	4.25	163	16.1	262.4
4	52,600	27.5	51	2.8	5.23	157	13.7	215.1
C 1	105,600	40	15	2.2	4.50	275	20.11	5530.3
2	105,600	42	31	2.5	3.67	288	21.2	6105.6
3	105,600	42	51	2.5	4.52	285	17.7	504.5
4	105,600	40.5	71	2.5	4.71	266	15.1	4016.6

TABLE (5)

REPRESENTATIVE ACTIVE SITE LOCATION AND EMISSION FREQUENCY DATA

TEST A1

X (Inches)	Y (Inches)	f (Bubbles/Sec.)	X (Inches)	Y (Inches)	f (Bubbles/Sec.)
0.011	0.255	4.7	0.380	0.389	15.7
0.038	0.440	8.0	0.384	0.741	12.3
0.092	0.775	22.1	0.464	0.893	10.9
0.013	0.917	6.5	0.498	0.280	5.9
0.124	0.572	11.6	0.56	0.912	6.6
0.068	0.123	4.4	0.654	0.703	9.9
0.074	0.604	10.0	0.520	0.572	13.4
0.122	0.215	5.0	0.568	0.374	9.4
0.150	0.660	21.2	0.600	0.285	20.3
0.100	0.965	17.3	0.628	0.809	18.8
0.125	0.856	28.8	0.640	0.926	18.0
0.150	0.335	8.2	0.645	0.556	18.7
0.172	0.114	3.7	0.685	0.186	8.0
0.113	0.000	24.6	0.750	0.97	13.8
0.200	0.264	5.5	0.756	0.646	6.9
0.209	0.476	22.4	0.744	0.444	10.9
0.250	0.775	5.7	0.812	0.042	4.8
0.262	0.58	19.7	0.875	0.493	17.6
0.256	0.068	6.2	0.850	0.345	16.0
0.362	0.205	10.9	0.900	0.900	13.4
0.375	0.515	20.9	0.920	0.623	7.2
0.377	0.890	18.1	0.910	0.268	5.8
0.390	0.995	21.1	0.985	0.206	8.5
0.345	0.295	13.4			

TABLE (6)

ACTIVE SITE DISTRIBUTIONS

Test No.	Na	P(EXP.)	P(Poisson)
A1	0	0.12	0.14
	1	0.28	0.27
	2	0.28	0.27
	3	0.24	0.18
	4	0.08	0.09
	5	0.00	0.03
A2	0	0.12	0.13
	1	0.28	0.27
	2	0.32	0.30
	3	0.16	0.18
	4	0.08	0.09
	5	0.04	0.04
	6	0.00	0.01
A3	0	0.16	0.16
	1	0.28	0.30
	2	0.28	0.27
	3	0.20	0.16
	4	0.08	0.07
	5	0.00	0.03
B1	0	0.00	0.001
	1	0.00	0.007
	2	0.00	0.025
	3	0.08	0.057
	4	0.12	0.100
	5	0.16	0.135
	6	0.16	0.152
	7	0.16	0.147
	8	0.12	0.127

Test No.	Na	P(EXP.)	P(Poisson)
B1	9	0.08	0.097
	10	0.04	0.066
	11	0.04	0.041
	12	0.04	0.024
	13	0.00	0.012
B2	0	0.00	0.001
	1	0.00	0.010
	2	0.04	0.037
	3	0.04	0.077
	4	0.12	0.121
	5	0.16	0.152
	6	0.16	0.160
	7	0.16	0.143
	8	0.12	0.112
	9	0.08	0.078
	10	0.04	0.050
	11	0.04	0.028
	12	0.04	0.011
	13	0.00	0.002
B3	0	0.00	0.001
	1	0.00	0.009
	2	0.04	0.031
	3	0.04	0.068
	4	0.12	0.111
	5	0.16	0.150
	6	0.16	0.160
	7	0.16	0.150
	8	0.16	0.120
	9	0.08	0.080
	10	0.04	0.050
	11	0.04	0.033

Test No.	Na	P(EXP.)	P(Poisson)
B3	12	0.00	0.018
B4	0	0.00	0.010
	1	0.00	0.010
	2	0.04	0.037
	3	0.08	0.077
	4	0.12	0.121
	5	0.16	0.152
	6	0.16	0.160
	7	0.16	0.143
	8	0.12	0.112
	9	0.08	0.078
	10	0.04	0.050
	11	0.00	0.028
C1	0	0.00	0.000
	1	0.00	0.000
	2	0.00	0.001
	3	0.00	0.004
	4	0.00	0.010
	5	0.00	0.022
	6	0.04	0.041
	7	0.08	0.065
	8	0.08	0.090
	9	0.12	0.108
	10	0.12	0.120
	11	0.12	0.120
	12	0.12	0.110
	13	0.12	0.093
	14	0.08	0.073
	15	0.04	0.053
	16	0.04	0.037
	17	0.04	0.024

Test No.	Na	P(EXP.)	P(Poisson)
C1	18	0.00	0.010
C2	0	0.00	0.000
	1	0.00	0.000
	2	0.00	0.000
	3	0.00	0.003
	4	0.00	0.007
	5	0.00	0.017
	6	0.04	0.032
	7	0.08	0.053
	8	0.08	0.077
	9	0.12	0.098
	10	0.12	0.113
	11	0.12	0.118
	12	0.12	0.113
	13	0.12	0.100
	14	0.08	0.091
	15	0.08	0.063
	16	0.04	0.046
	17	0.04	0.031
	18	0.00	0.010
C3	0	0.00	0.000
	1	0.00	0.000
	2	0.00	0.001
	3	0.00	0.003
	4	0.00	0.010
	5	0.00	0.019
	6	0.04	0.036
	7	0.04	0.057
	8	0.08	0.080
	9	0.12	0.100
	10	0.12	0.113

Test No.	Na	P(EXP.)	P(Poisson)
C3	11	0.12	0.115
	12	0.12	0.112
	13	0.12	0.094
	14	0.08	0.075
	15	0.08	0.059
	16	0.04	0.040
	17	0.04	0.028
	18	0.00	0.012
C4	0	0.00	0.000
	1	0.00	0.000
	2	0.00	0.001
	3	0.00	0.005
	4	0.00	0.013
	5	0.04	0.027
	6	0.04	0.048
	7	0.08	0.073
	8	0.12	0.098
	9	0.12	0.115
	10	0.12	0.123
	11	0.12	0.119
	12	0.12	0.105
	13	0.08	0.086
	14	0.08	0.065
	15	0.04	0.046
	16	0.04	0.031
	17	0.00	0.019

APPENDIX E

CHI-SQUARED GOODNESS-OF-FIT TEST

The most commonly used, and perhaps most versatile procedure for evaluating distributional assumptions is the chi-squared goodness-of-fit test. It is used to compare the experimental number of observations with the expected number of observations based on the proposed distribution. From this comparison a test statistic that approximately follows a chi-square distribution only if the assumed model is correct, is calculated. The test statistic will tend to exceed a chi-square value if the assumed model is not correct. This test can be carried out by computing the value of χ^2 and the degrees of freedom

$$\chi^2 = \sum_{i=1}^{k} \frac{(M_i - E_i)^2}{E_i}$$

where

M_i = Actual number of observations

E_i = Expected number of observations

k = Number of classes

Degrees of freedom = $k - r - 1$

where

k = Number of classes

r = Number of parameters in the proposed distribution (1 in Poisson distribution)

TABLE (7)
χ^2 Test

Test No.	Degrees of Freedoms	χ^2
A1	4	1.501
2	5	0.404
3	4	0.949
B1	12	2.210
2	11	1.489
3	11	1.520
4	10	1.100
C1	16	1.576
2	16	1.605
3	16	1.593
4	16	1.527

Figure (64) shows that all the χ^2 values lie in the good-fit region for the proposed Poisson distribution.

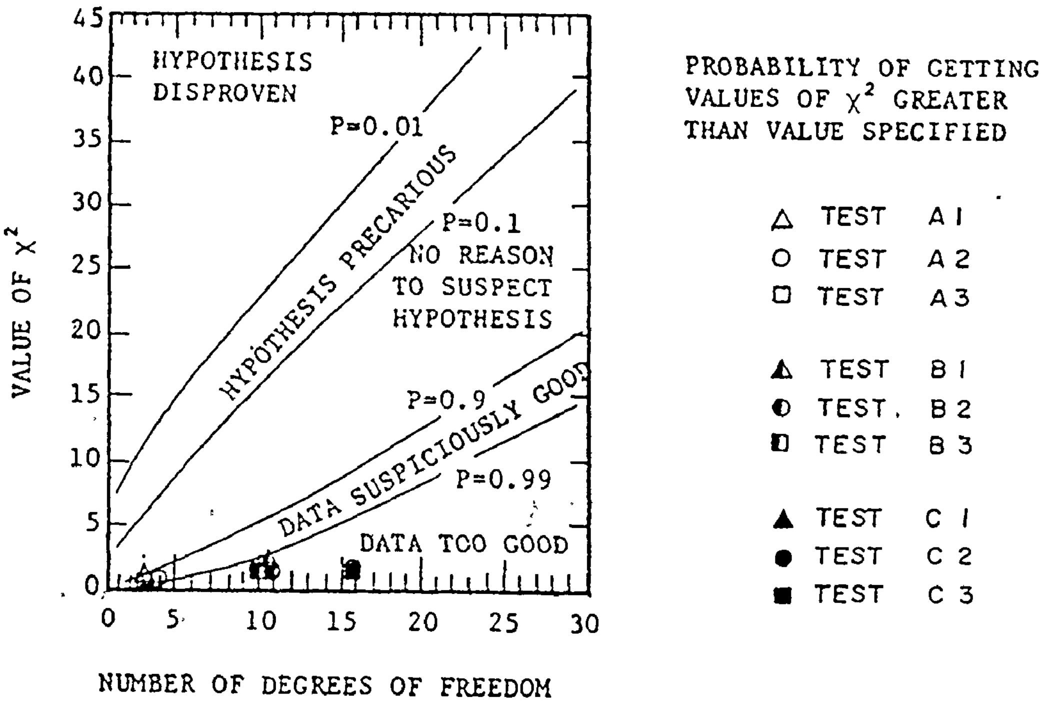

Figure (64) Graphical Comparison of χ^2 Data

APPENDIX F

UNCERTAINTY ANALYSIS

The uncertainty of each computed result was calculated using the following equation:

$$\frac{W_R}{R} = \left[\left(\frac{\partial R}{\partial v_1}\frac{W_1}{R}\right)^2 + \left(\frac{\partial R}{\partial v_2}\frac{W_2}{R}\right)^2 + \cdots + \left(\frac{\partial R}{\partial v_n}\frac{W_n}{R}\right)^2 \right]^{\frac{1}{2}} \quad \text{----(F.1)}$$

where

R = result computed

W_R = uncertainty in the result R

v_n = n^{th} variable

W_n = uncertainty in the n^{th} variable

Heat Flux

1. HEAT INPUT $(Q/A)_{Input}$ (65,730 BTU/hr. ft.^{2})

The uncertainty of the heat input to the system is due to the uncertainty of the wattmeter reading, which is about 10 watts. Using equation (F.1)

$$W_{(Q/A)_{Input}} / (Q/A)_{Input} = 2.38\%$$

2. HEAT LOSS $(Q/A)_{Loss}$ (13,010 BTU/hr. ft.^{2})

The uncertainty of the heat loss is mainly due to the uncertainty in the thermocouple potentiometer reading. Using equation (F.1)

$$W_{(Q/A)_{Loss}} / (Q/A)_{Loss} = 9.7\%$$

Therefore

$$W_{(Q/A)_{Actual}}/(Q/A)_{Actual} = 3.81\%$$

Superheat

The uncertainty of the surface superheat was due to the uncertainty of the thermocouple potentiometer reading. Using equation (F.1) at $T_w - T_s = 32^{o}F$

$$W_{(T_w - T_s)}/(T_w - T_s) = 2.2\%$$

Subcooling

The uncertainty of the subcooling was due to the uncertainty of the thermocouple potentiometer reading. Using equation (F.1) at $T_s - T_\infty = 51^{o}F$

$$W_{(T_s - T_\infty)}/(T_s - T_\infty) = 1.41\%$$

Site Location

The uncertainty of the site location was due to the uncertainty of X - Y stage reading which was indicated ±0.0001 inches.

The Probable Error in the Average Bubble Frequency

$$f = 12.57 \text{ (Bubbles/Sec.)}$$

$$PE_{\bar{f}} = 0.38 \text{ (Bubbles/Sec.)}$$

Therefore

$$\bar{f} = 12.57 \pm 0.38 \text{ (Bubbles/Sec.)}$$

NOMENCLATURE

SYMBOL	DESCRIPTION	UNITS
A	Total area of heat transfer surface	ft.^{2}
a	Local area of heat transfer	ft.^{2}
$\bar{D}$	Average diameter of bubbles at departure	ft
r	Nucleus radius	ft
R	Cavity radius	ft
t	Thickness	ft
S	Nearest-neighbor distance between active sites	ft
$\bar{S}$	Average nearest-neighbor distance between active sites	ft
$\bar{h}_c$	Average heat transfer coefficient	BTU/hr ft^2 hr
$\sqrt{\bar{S}^2}$	Root-mean-square nearest-neighbor distance between active sites	ft
S_{mp}	Most probable nearest-neighbor distance between active sites	ft
S_{min}	Minimum nearest-neighbor distance between active sites	ft
Q	Rate of heat transfer	BTU/hr.
T	Temperature	^oR
ΔT_{sup}	Temperature difference $(T_w - T_s)$	^oF
ΔT_{sub}	Temperature difference $(T_s - T_\infty)$	^oF
P	Pressure	lb_f/ft^2
k	Thermal conductivity	BTU/hr. ft.^{o}F
$\bar{h}_c$	Heat transfer coefficient	BTU/hr. ft.^{2} ^{o}F

h_{fg}	Latent heat of vaporization	BTU/lb_m
$\overline{R}$	Gas constant	$BTU/lb_m{}^oR$
N^*	Avogadro's number	
M	Molecular weight of fluid	
g	Acceleration due to gravity	ft/hr^2
g_c	Conversion factor	$lb_m\ ft/lb_f\ hr^2$
$\overline{f}$	Average vapour bubble frequency	sec^{-1}
N	Total population of active site on area A	
$\overline{N}$	Average population of active site on area A	
N/A	Active site density	
Na	Population of active sites on local area a	
$\overline{Na}$	Average population of active sites on local area a	
P(Na)	Probability that a random local area a has a population Na	
P($\overline{Na}$)	Probability that a random local area a has a population $\overline{Na}$	
P(0)	Probability that a random local area a has no active sites	
Z_{Na}	Number of local micro-areas having a local population Na	
C, m, N_0, ϕ	Constants	

SUBSCRIPTS

ℓ	Liquid
v	Vapour

w	Surface	
s	Saturation	
∞	Bulk	
i	Inside	
o	Outside	

GREEK LETTERS

ρ	Density	lb_m/ft^3
δ	Surface tension	lb_f/ft
θ	Contact angle	
ϕ	Cone angle	

REFERENCES

1. Jakob, M., "Heat Transfer", Vol. 1, Wiley, New York, (1949).

2. Corty, C. and Foust, A. S., "Surface Variables in Nucleate Boiling", Chem. Eng. Prog. Symp. Series, V. 51, No. 17, (1955).

3. Hsu, S. T., Schmidt, F. W., "Measured Variations in Local Surface Temperatures in Pool Boiling of Water", Trans. ASME, Journal of Heat Transfer, (1961).

4. Kurihara, H. M., Myers, J. E., "The Effects of Superheat and Surface Roughness on Boiling Coeffiecients", AIChE J., V. 6, No. 1, (1960).

5. Berenson, P. J., "Experiments on Pool Boiling Heat Transfer", Int. J. Of Heat and Mass Transfer, V. 5, (1962).

6. Vachon, R. I, Tanger, Davis and Nix, "Pool Boiling on Polished and Chemically Etched Stainless-Steel Surface", J. Heat Transfer, Trans. ASME, Series C, V. 90, No. 2, (1968).

7. Shoukri, M., Judd, R. L., "Nucleation Site Activation in Saturated Boiling", J. Heat Transfer, Trans. ASME, Series C, V. 97, N. 1, (1975).

8. Nishikawa, K, Trans. Soc. Mechanical Engineers, Japan, 20, (1954).

9. Marto, P. J., Moulson, J. A., Maynard, M. O., "Nucleate Pool Boiling of Nitrogen with Different Surface Conditions", J. Heat Transfer, ASME, Series C, 90, (1969).

10. Bankoff, S. G., AIChE J., V.4, P. 24, (1958).

11. Lorenz, Mikic, Rohsenow, "Fifth International Heat Transfer Conference" Sep. (1974).

12. Singh, Mikic and Rohsenow, "Active Sites in Boiling", ASME, 11, (1975).

13. Rohsenow, W. M., "Developments in Heat Transfer", M. I. T. Press (1964).

14. Westwater and Gaertner, "Population of Active Sites in Nucleate Boiling Heat Transfer", Chem, Eng. Prog. Symp., Series 30, 56, (1960).

15. Heled, Y. and Orell, A. "Characteristic of Active Nucleation Sites in Pool Boiling", J. Heat and Mass Transfer, V. 10, P. 553-554, (1967).

16. Nail, J. P., Vachon, R. I. and Morehouse, "An SEM Study of Nucleate Sites in Pool Boiling From 304 Stainless-Steel", ASME, May, (1974).

17. Jakob and Fritz, Forsch. Geo. Ingr. 2, (1931).

18. Zuber, N., Trans. J. Heat Transfer, ASME 80, (1958).

19. Gaertner, R. F., "Distribution of Active Sites in Nucleate Boiling of Liquids", Ch. Eng. Prog. Sym. Ser., Vol. 59, N. 41, (1963).

20. Staniszewski, B. E., "Nucleate Boiling Bubble Growth and Departure", Tech. Rept. H.T., MIT, (1959).

21. Brown, W. T., "Study of Flow Surface Boiling", Ph.D. Thesis, Mech. Eng. Dept., M.I.T., (1967).

22. Judd, R. L., "Influence of Acceleration on Subcooled Nucleate Boiling", Ph.D. Thesis, Univ. of Michigan, U.S.A., 1968.

23. Voutsinos, C. M., "Laser Interferometric Investigation of Microlayer Evaporation Various Levels of Subcooling and Heat Flux", M. Eng., Mech. Eng. Dept., McMaster Univ. Canada, (1976).

24. Judd, R. L. and Hwang, K. S., "A Comprehensive Model for Nucleate Pool Boiling Heat Transfer"

25. Wiebe, J. R., "Temperature Profiles in Subcooled Nucleate Boiling", M.Eng., Mech. Eng. Dept., McMaster Univ., Canada, (1970).

26. ASME Heat Transfer Division, "Two Phase Flow Instrumentation", Aug. (1969).

27. Shoukri, M., Private Communication.

28. Gaertner, R. F., "Photographic Study of Nucleate Pool Boiling on a Horizontal Surface", Trans. ASME, Series C, V. 87, (1965).

29. Westwater, J. W. and Kirby, D. B., "Bubble and Vapour Behaviour on a Heated Horizontal Plate During Pool Boiling Near Burnout", Chem. Eng. Prog. Symp. Series, V. 61, N. 57, (1965).

30. Schenck, H., Heat Transfer Engineering Prentice-Hall Inc., (1959).

31. Rohsenow, W. M., "Nucleation with Boiling Heat Transfer", ASME, (1970).

32. Kendall, M. G. and Stuart, A., "The Advanced Theory of Statistics,

V. 1, 3rd Edn., (1969).

33. Duncan, A. J., "Quality Control and Industrial Statistics", (1952).